The University of Nottingham
UNITED KINGDOM · CHINA · MALAYSIA

Cheng, Zhixing (2021) Controllable synthesis of transition metal nitride materials and performance tuning in photocatalysis and piezoelectric catalysis. PhD thesis, University of Nottingham.

Access from the University of Nottingham repository:
http://eprints.nottingham.ac.uk/65532/1/Zhixing%20Cheng%20-%2020127465%20-%20Thesis.pdf

Copyright and reuse:

The Nottingham ePrints service makes this work by researchers of the University of Nottingham available open access under the following conditions.

This article is made available under the University of Nottingham End User licence and may be reused according to the conditions of the licence. For more details see: http://eprints.nottingham.ac.uk/end_user_agreement.pdf

For more information, please contact eprints@nottingham.ac.uk

Controllable Synthesis of Transition Metal Nitride Materials and Performance Tuning in Photocatalysis and Piezoelectric Catalysis

Thesis submitted to be University of Nottingham for the degree of

Doctor of Philosophy, July 2021.

Zhixing Cheng

20127465

Supervised by

Tao Wu

Minghui Yang

Mike George

Signature _____

Date _____

Abstract

Energy crisis has become imminent owing to the increasing energy demand in recent years. Renewable and sustainable alternative energy resources, such as hydrogen have attracted significant attentions. In order to produce hydrogen energy efficiently, artificial photocatalysis is an attractive way forward. Use of piezoelectric materials for solar energy conversion is being researched in this context. However, such materials that are semiconductor-based are not practically viable applications. Simultaneously, as a kind of most efficient catalyst, the noble metal is difficult to apply in large-scale. Transition metal nitrides (TMNs) have become a family of alternatives of noble metal catalysts due to their unique properties. However, the present synthesis methodologies of TMNs are complex with severe conditions. Maintenance of morphology of TMNs also remains a challenge, since morphological changes do influence their activity. This thesis has provided a new strategy for production of TMNs with stable nano-morphology. These have been used for photocatalytic and piezoelectric H_2 evolution, while discussing the structure-activity relationship. The details are listed below:

(1) A novel hard template/rapid-nitridation synthesis of ordered mesoporous metal nitrides is reported, which is based on a nanocasting-thermal nitridation process. This method uses 2D ordered hexagonal mesoporous SBA-15 as the hard template. A series of TMNs with ordered and regular mesoporous structures have been successfully synthesized from the corresponding mesoporous oxides. A comparative experiment shows that when a long-time heating process is employed, the ordered mesopores are hard to maintain anymore due to the collapse and coalescence of the porous structure. This proves the necessity of rapid-nitridation for keeping nanostructures of materials.

(2) Prussian blue (PB) precursors are first oxidized and then subjected to rapid-nitridation to obtain pure porous Fe_2N nanocubes while maintaining the pattern and structure of the parent MOF precursor. The samples are sensitized using Eosin-Y (EY)

in photocatalytic HER. The performance of cube-like Fe_2N is duly rationalized using DFT-based calculations and its metallic nature is also duly elaborated. The optimal Fe_2N/EY system exhibits excellent photocatalytic hydrogen evolution performance.

(3) MOF-derived Fe_2N with different types of doped elements (Co, Cr, W and V) are successfully synthesized. Rapid-nitridation has been applied as a synthesized method, which is efficient for retaining the morphology of catalyst. The regular nanocubic pattern of samples has been maintained. The doped Fe_2N have been utilized for piezoelectric catalytic H_2 evolution and the Co-doped Fe_2N has achieved the highest activity (122.8 μmol $g^{-1}h^{-1}$). After tuning the doping ratio, the Co and V doped Fe_2N have greatly improved their H_2 evolution performance. Compared with the control experiments, the sample with nanocubic morphology has a higher H_2 evolution rate than that of the nanoparticle sample. These doped Fe_2N catalysts also have the ability to degrade different types of dye, while improving their H_2 production efficiency. Besides, the DFT calculation has elucidated the activity improvement of doped nitrides.

In summary, this thesis has introduced a method for synthesizing several types of ordered porous TMN materials. They have exhibited considerable activity and properties in the application of H_2 evolution by photocatalysis and piezoelectric catalysis. The relationship between the performance and the morphology as well as nanostructure has been demonstrated.

Keywords: Transition Metal Nitride, Rapid-Nitridation, Hydrogen Evolution, Photocatalysis, Piezoelectric Catalysis.

Acknowledgements

After three years of learning and research for a PhD degree, I have grown a lot and attained significant experience of lifelong value. At this juncture, I would like to take this opportunity to thank a number of people who have offered invaluable assistance in the preparation of this thesis.

My deepest gratitude goes first and foremost to Professor Wu Tao, my first supervisor, who provided the opportunity for me to work as a PhD student at University of Nottingham. He has also given me lots of help during the annual report and viva processes. Then, I would like to thank Professor Minghui Yang, my second supervisor, who played a critical role in my progress during my PhD period. He has walked me through all the stages of research at Ningbo Institute of Materials Technology & Engineering. Besides, he also offered valuable suggestions for the writing of this thesis. His critical comments, constant encouragement and guidance have greatly enlightened me not only on the academic pursuit but also on the morals of good living. Without his consistent and illuminating instruction, I would not have the achievements I report in this thesis. Finally, I also would like to thank my third supervisor Mike George.

Secondly, I would like to express my heartfelt thanks to senior Siqi Liu, whose detailed guidance has well prepared me for the completion of the thesis, daily research and experiments during my whole PhD period.

I also greatly appreciate the assistance offered by the research mates and scholars mentioned in the bibliography, especially Weiliang Qi, Jiuyang Yu, Ali Saad and Tiju Thomas, without whose works, the literature review of my thesis would not have been possible. They also gave me warmth, guidance and companionship.

Last, I am deeply indebted to my beloved parents, friends, and my girlfriend Shan Li, who always supported me, willingly discussed with me, and offered valuable insights. Their help and support have helped me through the difficult course of the thesis and given me valuable moments in my life.

Contents

List of Tables

List of Figures

Abbreviations

1D	One Dimension
2D	Two Dimension
3D	Three Dimension
AC	Alternating Current
BET	Brunauer-Emmett-Teller
CB	Conduction Band
CV	Cyclic Voltammetry, Cyclic Voltammogram
DFT	Density Functional Theory
DOS	Density of States
EIS	Electrochemical Impedance Spectroscopy
EY	Eosin-Y
FT-IR	Fourier Transform-Infrared
GCE	Glassy Carbon Electrode
HER	Hydrogen Evolution Reaction
HOMO	Highest Occupied Molecular Orbital
HRTEM	High-Resolution Transmission Electron Microscopy
LUMO	Lowest Unoccupied Molecular Orbital
LSPR	localized Surface Plasmon Resonance
LSV	Linear Sweep Voltammetry
MO	Methyl Orange

MOF	Metal-Organic Framework
OER	Oxygen Evolution Reaction
PB	Prussian Blue
PDOS	Partial Density of States
PVP	Polyvinyl Pyrrolidone
RhB	Rhodamine B
RHE	Reversible Hydrogen Electrode
SAED	Selected Area Electron Diffraction
SEM	Scanning Electron Microscopy
TEM	Transmission Electron Microscopy
TEOA	Triethanolamine
TMN	Transition Metal Nitride
TMO	Transition Metal Oxide
TOF	Turnover Frequency
TON	Turnover Number
UV-Vis	Ultraviolet-Visible
VB	Valence Band
XPS	X-ray Photoelectron Spectroscopy
XRD	X-ray Diffraction
ZIF	Zeolitic Imidazolate Framework

Dissemination Section

The main parts of this thesis are based on the author's formal publications. The contents of **chapter 1** mainly come from **Publication 1**. The experiment sections of **chapter 2** mainly come from the experiment sections of **Publication 1, 2, 3**. The contents of **chapter 3** mainly come from **Publication 2**. The contents of **chapter 4** mainly come from **Publication 3**. The contents of **chapter 6** are mainly rewritten based on **Publication 2,3**.

1. Z. Cheng, W. Qi, C. H. Pang, T. Thomas, T. Wu, S. Liu*, M. Yang*, Recent advances in transition metal nitride-based materials for photocatalytic applications. *Advanced Functional Materials*, **2021**, 2100553.

2. Z. Cheng, A. Saad, H. Guo, C. Wang, S. Liu, T. Thomas, M. Yang. Ordered mesoporous transition metal nitrides prepared through hard template nanocasting and rapid nitridation process. *Journal of Alloys and Compounds* **2020**, 838, 155375.

3. Z. Cheng, A. Saad, S. Adimi, H. Guo, S. Liu, T. Thomas, M. Yang. Metal organic framework-derived porous Fe_2N nanocubes by rapid-nitridation for efficient photocatalytic hydrogen evolution. *Materials Advances* **2020**, 1, 1161–1167.

Chapter 1

Introduction

1.1 Research background

The global energy demand has been increasing continuously in recent years because of the increase in population and industrialization. This has led to progressively higher use of traditional fossil fuels, which causes environmental problems such as water, air pollution and the greenhouse effect.[1,2] Thus, pursuing renewable and sustainable alternative energy resources has become an urgent requirement. This direction has hence attracted the significant attention of researchers.[3,4] Hydrogen energy is an abundant and clean energy resource, which can be an ideal choice to meet future demand.[1,5] It is highly desirable to achieve a high rate of energy harvesting and conversion from solar energy.[6–8] The cost-effective hydrogen production technology plays an important role in the realization of hydrogen energy schemes.[9] Compared to the electro-dissociation of water, photo-chemical dissociation of water by solar energy is a more promising strategy to produce hydrogen. In addition, as another new efficient technology for promoting the energy conversion reaction, piezoelectric effect has also been recently researched.[10] For the smoothly proceeding of the reaction, efficient photo- and piezoelectric catalysts are required.

Since the pioneering work of photochemical hydrogen generation was reported, a variety of semiconductor-based materials have been developed, which are able to absorb visible light for utilizing solar energy. Generally, these photocatalysts mainly include metal oxides, sulfides, (oxy)nitrides and metal-free compounds.[11–14] However, they still have disadvantages such as large band gap, the tendency of recombination of

electron-hole pairs and insufficient energy efficiency.[15] Noble metal-based materials including Ir, Ru and Pt are still the best catalysts for HER and OER.[9] However, due to their high price and low reserves, these precious metals are hindered to be utilized in large-scale applications. Thus, the development of efficient and low-cost photocatalysts is important. For piezoelectric catalysts, most of the applied materials have disadvantages such as large size, small specific surface area and fewer active sites.[16] Therefore, it is desirable to explore a type of new piezoelectric catalyst with a suitable energy band structure, considerable material properties and the tunable porous morphology of nanostructure.

Among the non-noble catalysts, transition metal nitrides (TMNs) have emerged as a kind of new family of alternatives of photocatalytic noble metal catalysts and new efficient piezoelectric catalysts due to their unique physical, chemical and electronic properties.[9,17,18] However, the synthesis methodologies of TMN are generally complex with severe conditions. TMN produced using common methods tend to form agglomerations, which seriously influence their photocatalytic performance and reduces the active sites for piezoelectricity.[19] Thus, exploration of a new strategy of TMN synthesis while maintaining the porous structure, and applications of such functional nanostructure TMNs in photocatalytic and piezoelectric hydrogen production are significantly desirable.

1.2 Photocatalysis and piezoelectric catalysis

1.2.1 Background of photocatalysis

Photocatalysis is a convenient and environment-friendly means to convert solar energy into chemical energy.[15] Specially, photocatalytic water splitting is regarded as artificial photosynthesis (**Figure 1.1**).[20] Fujishima and Honda pioneering work of solar energy conversion using TiO_2 photocatalysts was reported in 1972.[21] Thereafter, researchers have been continuously exploring new materials as photocatalysts.[1,2,5,15,20,22] The earliest reports are mainly based on TiO_2-based semiconductor photocatalysts.[23–26] However, in recent years, semiconductor materials such as g-C_3N_4, CdS, Ag_3PO_4 and related composites have also attracted interest.[27–35] Photocatalysis plays an increasingly significant role in fields such as energy regeneration including H_2 production from splitting water and CO_2 reduction to fuels.[20,36–38] Likewise photocatalysis has also been used for clean chemical synthesis and environmental protection, including the degradation of organic dyes and inhibition of air and water pollution.[27,39–42] However, in most semiconductors, a combination of the large band gap and the tendency of recombination of electron-hole pairs limit the efficiency and practical utility.[15]

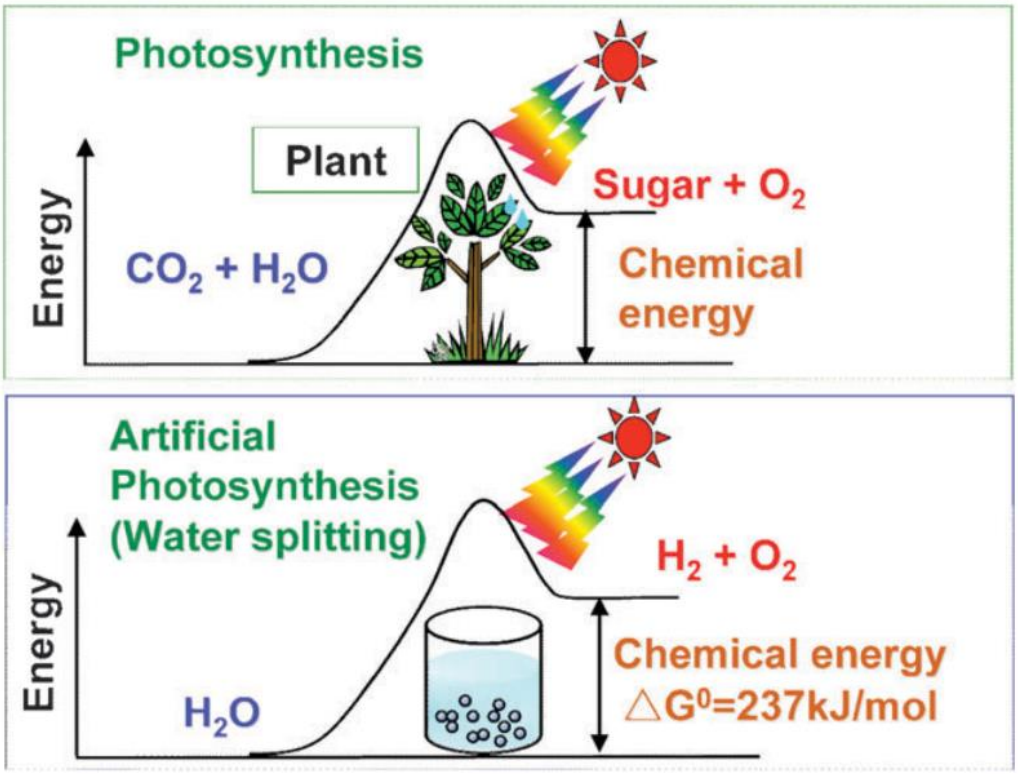

Figure 1.1 Photosynthesis by green plants and photocatalytic water splitting as artificial photosynthesis.[20]

In order to enhance the catalytic potential of semiconductor photocatalysts, adjustment of composition and application of cocatalysts have become two primary approaches. For example, ion doping and element substitution (such as nitrogen for oxygen) can enhance the photocatalytic activity of semiconductors by improving their conductivity, narrowing their band gaps and making them more active under visible light.[4,42–44] Ion doping can create point defects, generally including vacancy, interstitial particle and foreign particle. **Figure 1.2** has shown two cases that TiO_2 doped by C and S elements, which form intra-band-gap states close to VB and CB for inducing visible light absorption.[42] The new energy state (C 2p) is introduced by the substitution of the C atom in the n-type TiO_2 matrix, which leads to the shift of the VB edge to higher energy.

The energy state near the CB edge is created due to the substitution of Ti^{4+} by S^{6+}, which makes the band gap narrower.[42] In most cases, suitable dopants can enhance the visible light absorption and separation efficiency of photoexcited electron-hole pairs.[45] The low dopant content of metal ions can introduce localized electronic states, such as a donor level above the VB or an acceptor level below the CB in the forbidden band of wide band gap photocatalysts.[46] A sufficiently high dopant content can help in achieving multiphoton excitation of a wide band gap semiconductor by forming a delocalized state band in the intermediate region.[47,48] On the other hand, the element substitution is usually an important strategy to tune the basic properties of photocatalysts, such as band gap narrowing, adjustment of electronic structures and improvement of conductivity.[49] Through these processes, the light-harvesting, charge transfer reactions and surface reactions are promoted using different elements.[50] For example, nitrogen is used to replace oxygen in oxide semiconductors to form nitride semiconductors because of similar electronic, chemical and structural features of both nitrogen and oxygen. The N 2p atomic orbitals with higher potential energy than O 2p atomic orbitals are introduced. This leads to the formation of new VBs instead of O 2p atomic orbitals, thereby reducing the band gap energy without affecting the CB level. Therefore, a visible-light-driven photocatalyst with band edge potentials suitable for various photocatalytic reactions is produced.[13]

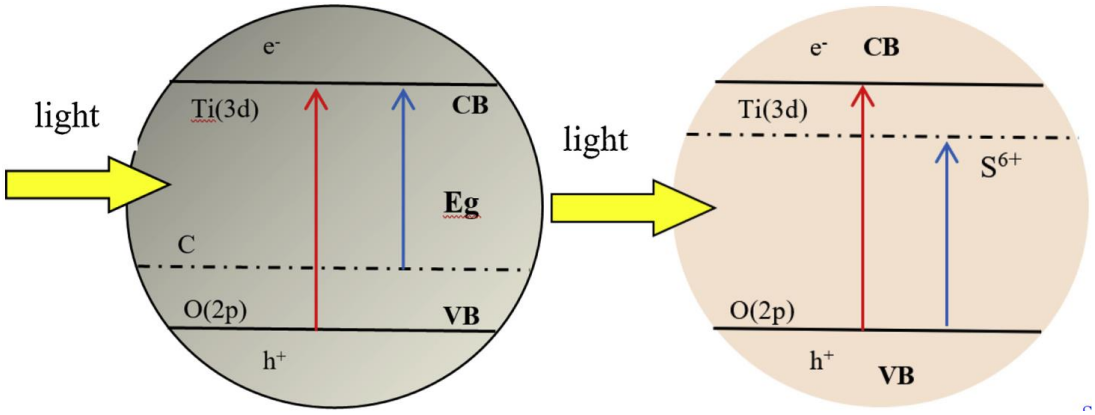

Figure 1.2 The change in the energy band gap diagram of n-type TiO_2 when doping C and S. The blue line is the energy band gap of C- and S-doping TiO_2 and the red line is the energy band gap of TiO_2.[42]

Also, co-catalysts have advantages such as decreasing the overpotential of photocatalytic reaction, extracting photogenerated charge carriers and host active sites, as well as improving the stability of photocatalysts through inhibiting photo-corrosion.[1,4] Thus, cocatalysts are widely utilized in photocatalytic systems to improve their efficiency considerably. In recent years, most conventional photocatalysts rely on noble-metal-based cocatalysts to realize high photocatalytic activity.[51–55] For instance, Pt is one of the most efficient cocatalysts for the H_2 evolution reaction because of its lowest overpotential and largest work function.[56,57] Meanwhile, RuO_2[58,59] and IrO_2[60,61] of noble metal oxides are well-known as outstanding cocatalysts for enhancing the photocatalytic O_2 evolution reaction. $Rh_{2-y}Cr_yO_3$ and core-shell-structured Rh-Cr_2O_3 are two of the most active cocatalysts in H_2 production by overall water splitting.[62–64] However, noble metals suffer from high cost and low abundance, which render them non-viable for widespread use in industrial production. Thus, the

development of noble-metal-free cocatalyst materials is very important for alternatives with superior activity and robust stability.[65–71]

1.2.2 Principles of photocatalysis

In general, the processes of photocatalytic reaction involve three main steps: (i) the adsorption of the photons by semiconductor to generate electron-hole pairs and the excited charge separation, (ii) transportation of electrons and holes to the semiconductor surface, and (iii) the utilization of charge for surface redox reactions (**Figure 1.3**).[1,5,72] The total efficiency of the photocatalytic reaction process depends on the thermodynamics and kinetics associated with these steps.[1]. **Figure 1.4** shows some of the Gibbs free energy changes of a few representative chemical reactions, including arguably the most promising reaction in the renewable energy sector: water splitting yielding hydrogen, as well as the CO_2 reduction and organic synthesis of fuels.[5,73–76]

In the first step of the reaction process, the efficiency of electron and hole separation is largely determined by chemical compositions, crystalline phases and junctions, nanostructure such as the width of the band gap, and material morphology.[72] During the second step of the process, a significant fraction of electron-hole pairs recombine due to surface sites.[50,77,78], which leads to energy loss in the form of heat or light emission.[79] This problem is one of the main troubles that need to be solved to make photocatalysis viable.[5,79] Thirdly photocatalysis needs a large number of active sites

for providing suitable environments for electron separation or adsorption from reagents, thus accelerating photocatalytic oxidation or reduction reactions on the surface of photocatalysts with extreme efficiency.[20] This process is promoted by the presence of cocatalyst, which acts as host active sites and extracts photogenerated charge carriers for photocatalytic oxidized and reduced production.[20] Therefore, cocatalysts play an important role in improving both the activity and stability of semiconductor photocatalysts.[80,81]

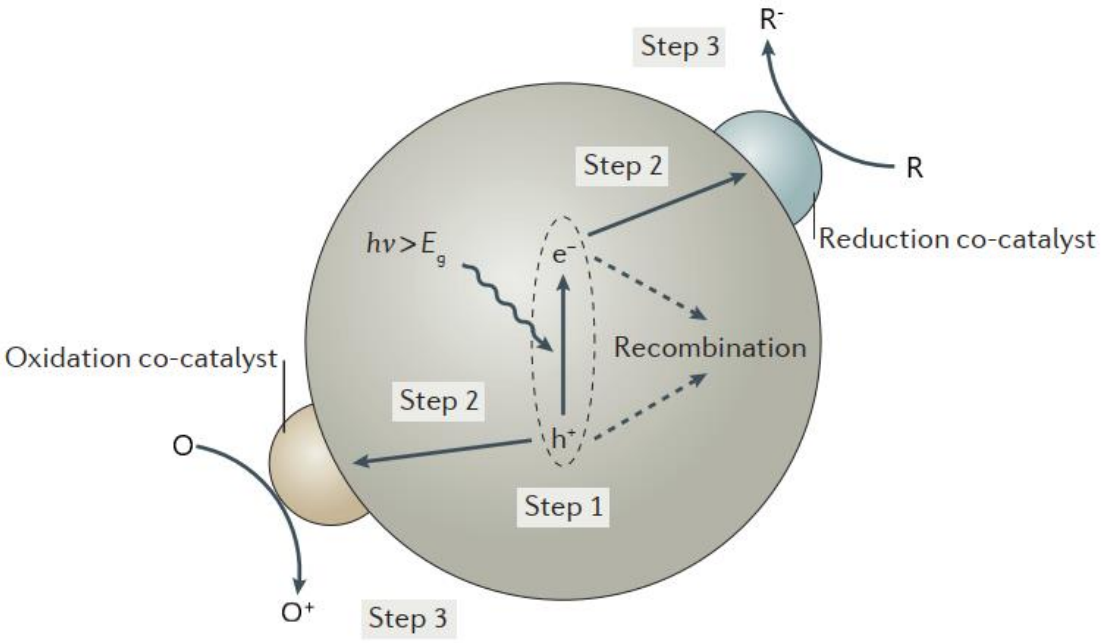

Figure 1.3 Schematic illustration of the main processes within the photocatalytic overall water-splitting reaction. E_g: semiconductor band gap. R: chemicals in reductive reactions, O: chemicals in oxidative reactions.[72]

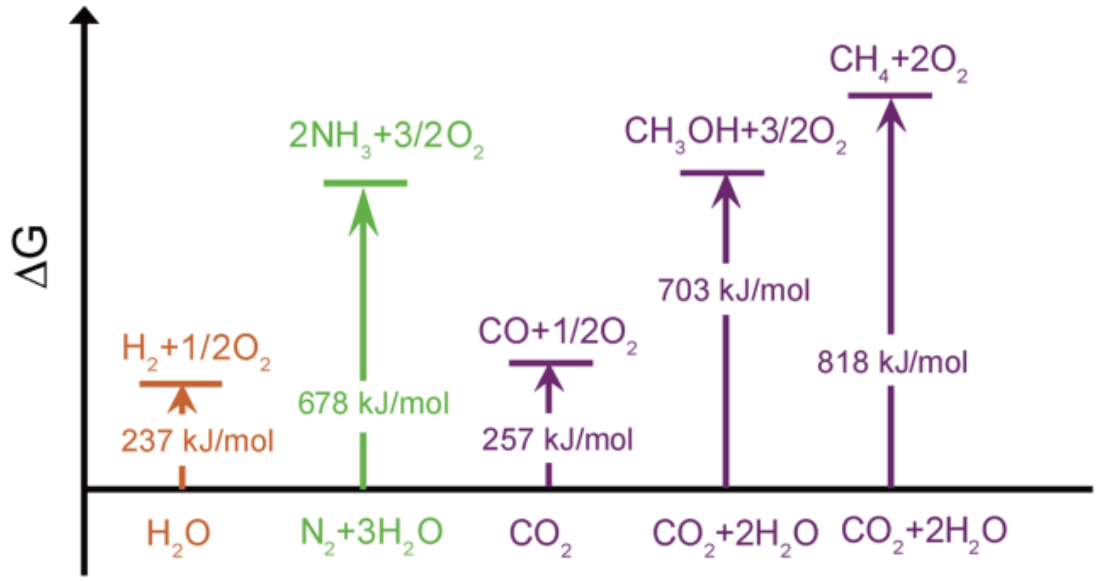

Figure 1.4 Energy diagrams of representative thermodynamically uphill reactions. Reproduced with permission.[5]

1.2.3 Background of piezoelectric catalysis

The materials that can collect mechanical energy have attracted significant attention in recent years. The concept of piezoelectric nanogenerator was first reported by Wang et al. in 2006 for achieving conversion of different types of mechanical energy.[82] They used the ZnO nanowires to transform mechanical energy into electricity successfully. The producing piezoelectric potential has shifted the energetics, which enables the electrons to transfer across the interface between piezoelectric and solution. Based on this research, the piezoelectric materials start to be utilized in piezoelectric catalysis. So far, piezoelectric catalysis has been researched and investigated for more than a decade. It plays an important role in fields such as water splitting, organic pollutants degradation and sterilization. An increasing number of piezocatalysts have been reported, including ZnO, $BiTiO_3$, $BiFeO_3$, $BiWO_6$, MoS_2, $MoSe_2$, $ZnSnO_3$, $KNbO_3$ and

so on.[83–90] Different kinds of nanostructural piezoelectric materials such as 1D wurtzite ZnO and $BaTiO_3$, 2D morphology or 3D hierarchitectures have also been investigated.[16]

The recent development of piezoelectric catalysis indicates that compared to the previous strategies of improving charge carrier separation in photocatalysis, the piezoelectric potential seems more efficient owing to long-range ordered electric field throughout the materials.[16] In addition, piezoelectric can utilize mechanical energy sources such as vibration, noise and fluid flow, which can be harvested from the surrounding environment.[18] Typical piezocatalysts including ZnO, perovskites and bismuth-based piezoelectrics are usually used in practical reactions.[16] However, most of these materials have drawbacks such as large size, small specific surface area and fewer active sites, which lead to limited piezoelectric activity.[86,91] In general, an ideal piezoelectric material is required to have great flexibility, a high piezo-electric coefficient, a large specific surface area for harvesting the mechanical energy and rich catalytic active sites.[19,91,92] Besides, the morphology of nanomaterials also act as an important role in the performance of piezoelectric catalysis. For instance, previous research has found that the ZnO nanorods and $BaTiO_3$ nanowires have much better piezoelectric performance compare to their corresponding nanoparticles.[84,93] In addition, it has been reported that the inversion symmetry of piezoelectric material would limit the induction of their piezoelectricity.[19,94] Thus, it is reasonable to explore piezoelectric catalysts with non-centrosymmetric crystal structure which is also

nanostructured, along with appropriate energy band structure.

At present, research on piezoelectric catalysis mainly focuses on the effect of polarization within materials and on the surface, different types of contacting modes of components, and band bending, as well as the mechanisms involved.[10,16,95–97] Thus, as a promising mechanical-energy-triggered catalysis strategy, piezoelectric catalysis has exhibited a significant potential in various practical application fields.

1.2.4 Principles of piezoelectric catalysis

The piezoelectricity origins from the non-centrosymmetric property, which results in the electric dipoles within the material. However, the piezoelectric crystals are still electrically neutral because of the canceling out of a positive and an adjacent negative charge.[10] Thus, if the crystals are stressed by squeezing or stretching, the movement of atoms from their original positions would change the state of electric neutrality. Then the unit cell gains the dipole moment, and the piezoelectric potential is produced because of the collective induced polarization of charges in the whole unit cell (**Figure 1.5a** and **b**).[16,82] For the piezoelectrics that are insulators with wide band gaps, free charge carriers are not available aplenty at the thermal equilibrium state. The two ends of piezoelectrics with sufficient thickness are separated and have independent fields. The piezoelectric potential will shift the electronic energy levels of occupied or unoccupied states. It will lower the CB until it goes marginally below the HOMO of the solution. Thereby the electron will transfer from HOMO to the CB and from VB to

LUMO (**Figure 1.5c** and **d**). Thus, the internal piezoelectric potential is able to alter the surficial charge energy of materials.[16,98] Finally, various redox reactions are triggered on the surface.

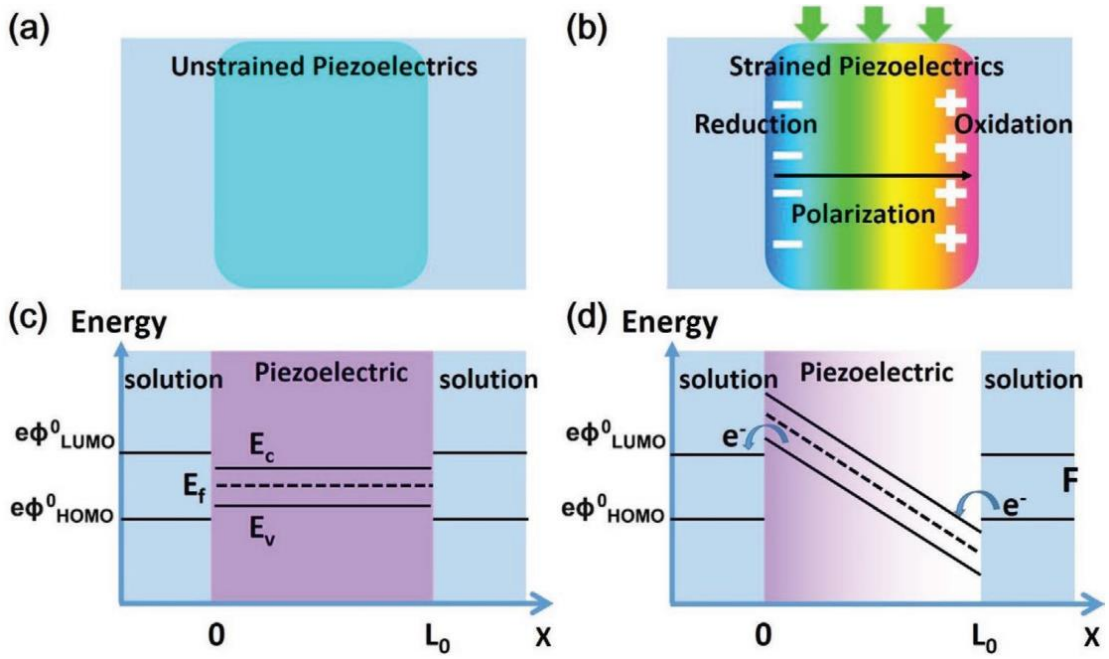

Figure 1.5 (a,b) Schematic diagrams depicting the potential distribution on piezoelectrics through bending. (c) Band diagram of unstrained and (d) strained insulating piezoelectric. The piezo-potential has changed the energy state across the material, allowing electron transfer between piezoelectric/solution interface.[98]

1.2.5 Assessments of photocatalysis and piezoelectric catalysis

Photocatalytic hydrogen production is induced by solar light, so it provides a valuable method to utilize solar energy, which is similar to the natural process of photosynthesis. As a convenient and environmental-friendly methodology, it has been researched for several decades since 1972 and has attained considerable progress in various fields.

However, two critical problems of photocatalysis that inhibit its developments are yet to be solved. One of the problems is the dependence on the light source, which is limited by the natural conditions. Another difficulty is the low utilization efficiency of solar energy in artificial photosynthesis (1-3%).[20] These two obstacles are derived from the nature of photocatalysis, thus further development remains a serious challenge.

In this case, piezoelectric catalysis has become a new strategy that has attracted considerable attention for producing hydrogen energy. This is because it can utilize weak mechanical energy sources from the surrounding environment, including various kinds of vibration and noise. This characteristic can avoid the dependence on the light source and natural conditions. Moreover, the mechanical-electric energy conversion efficiency has been reported as 78%, which is much higher than the light-electric conversion rate.[86] Thus, it is desirable to explore and develop the field of piezoelectric catalysis. However, most of the used materials in piezoelectric catalysis still have disadvantages such as small specific surface area and fewer active sites.[19,91,92] In addition, the morphology and the inversion symmetry of materials also influence the piezoelectric performance to a great extent.[19,84,93,94] Therefore, a type of new piezoelectric catalyst with considerable morphology, nanostructure and appropriate energy band structure is required to be discovered and explored.

1.3 Classification, advantages and applications of TMNs

1.3.1 Classification of TMNs

TMNs are classified based on their properties. Generally, they are classified into two types - semiconductors and non-semiconductors - for photocatalytic applications. The main distinction lies in determining whether or not a given compound has an obvious band edge associated with VB and CB. This would directly influence their reaction mechanisms and performance enhancement methods for practical applications. The following section provides a brief introduction to both these two types.

At present, the research on TMN semiconductor photocatalysts focuses mainly on Ta_3N_5, Cu_3N, AgN_3, Zr_3N_4 and Zn_3N_2. Their VB and CB positions are displayed in **Figure 1.6**.[99–106] The band gap energies of these semiconductors are mainly between 1.0 and 3.0 eV. As illustrated, most of the semiconductor TMNs straddle the redox potential of water; the relatively narrow band gap also aids in this. Benefitting from the suitable band edge position, Ta_3N_5 has sufficient overpotentials for photocatalytic applications.[101] Cu_3N is a type of defect tolerant semiconductor with a narrow band gap of 1.4 eV.[103] Cu_3N with antibonding VB maximum possesses shallow intrinsic defects and no surface states. This makes it easier to avoid charge carrier recombination centers of defects during photocatalytic processes.[103] AgN_3 and Zr_3N_4 are also among reported nitrides with band gaps of 2.7 and 2.6 eV.[104] Finally, Zn_3N_2 has a cubic structure with a lattice constant of 0.978 nm and a dark blue color.[107] There is variation in the reported band gap for this material, which depends among other things on the deposition methods or film composition chosen. Thus, the band gap energy ranging from 1.0 to 3.2 eV has been reported. This is marked as a dotted vertical line in **Figure**

1.6.[106]

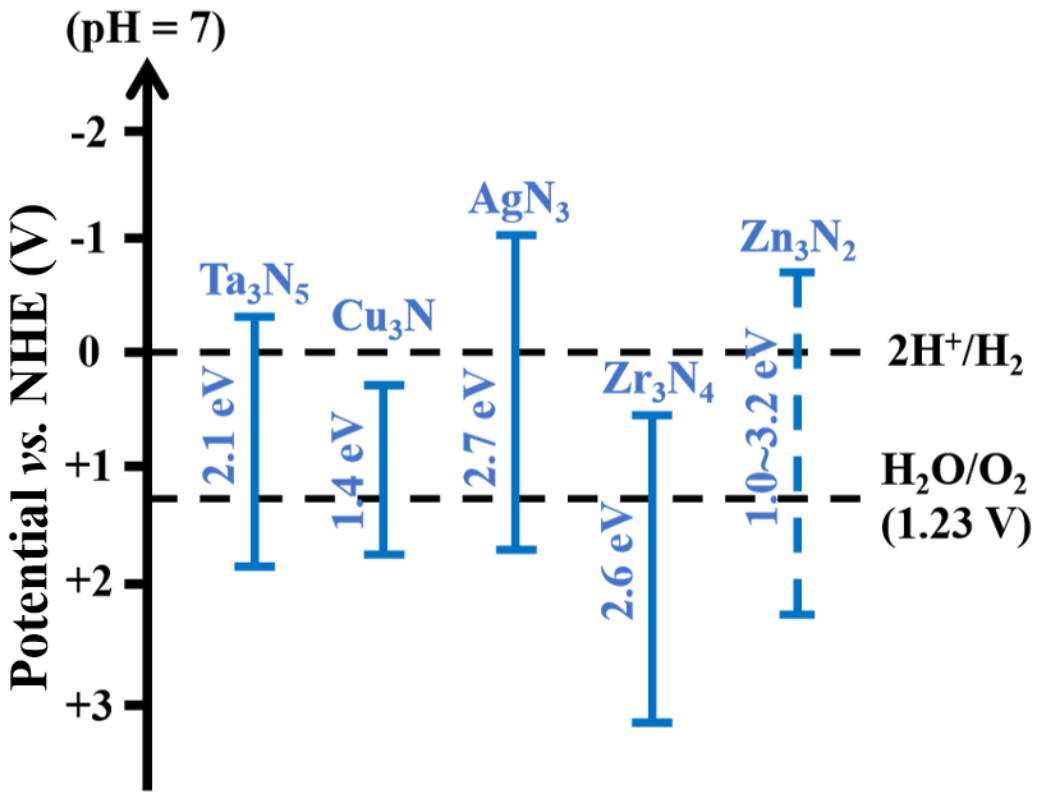

Figure 1.6 Band edge positions of reported semiconductor nitrides. The reduction and oxidation potentials of water are shown by black dotted lines. The band gap of Zn_3N_2 is shown by dotted lines since there is variance in reports.[99–106]

Actually, most of the TMNs used in photocatalysis are not semiconductors. They show metal-like properties without clearly separate VB and CB bands. Notably, some of TMNs have the ability to be excited by near-infrared light. For instance, WN and CoN have been reported and used as photocatalysts by promoting the inter-band excitation effect.[108,109] In addition, TMNs have the noble-metal-like collective localized surface plasmon resonance (LSPR) effect.[110,111] At present, TiN and WN have also been

applied in photocatalytic applications through the LSPR effect. This is proved by the theoretical calculations and experiment results.[110,112]

Besides, other TMNs including those comprising of Ti, Co, Ni, Fe, Mo, V and Nb are generally utilized as cocatalysts. They have optimal metal-like properties, even better than noble metals according to density functional theory (DFT) calculation and experimental results.[81] Thus, they can play an ideal role in the photocatalytic process to transfer electrons from the surface of photocatalysts. This successfully promotes the separation of electron-hole charge pairs and prevents recombination. As a result, these TMNs can efficiently improve the performance of pure photocatalysts. Their advantages and applications are demonstrated in the following sections.

1.3.2 Unique advantages of TMNs

TMNs have recently emerged as a class of metallic interstitial compounds and have attracted significant attention for photocatalysis applications due to their distinctive physical, electronic properties and noble-metal-like properties.[9,17] The intercalation of nitrogen atoms modifies the parent metal structure and leads to lattice expansion. This also resulted in an increase in the distance between metal atoms, and a concomitant reduction in inter-atomic interactions.[113] The contraction of the metal d-band would cause an increased DOS near the Fermi level compared to that of the parent metal, which can be observed from the DOS image. This led to an increased number of valence electrons (even better than noble metals in the VIII group) and a change of structure.[114]

Due to their rather unique chemistry, TMNs have properties that come about due to the mixed nature of bonding (covalent: a strong interaction between several neighboring atoms by sharing electrons; ionic: chemical bonds formed by electrostatic interaction between anions or cations), and the electronic configuration of transition metals. Thus, TMNs have better characteristics than their parent metals and compounds.[113] TMNs have metal-like properties such as considerable conductivity and narrowing of band gap which are beneficial for highly efficient delivery and separation of photo-generated carriers. It is also suitable as a semiconductor in photocatalysis.[49] TMNs can reduce the overpotential or activation energy for photocatalytic reactions on the surface of semiconductors by providing extra active sites, and promote the electron-hole separation at the interface between cocatalyst and semiconductor.[49] Besides, TMNs have low cost, ideal thermal stability and good tolerance against acids and bases. These properties also ensure that TMNs generally do not react with the environment or biological substance to produce toxic effects. This means they are environment-friendly. Hence they offer prospects for use as either photocatalysts or cocatalysts in the industrial field.[115,116]

1.3.3 Photocatalytic applications of TMNs

There are some publications of TMNs for utilization in photocatalysis such as water splitting, organic dye degradation and CO_2 reduction (**Figure 1.7**).[9] They are mainly used as active ingredients of semiconductors and cocatalysts due to their considerable

advantages. For example, Ta_3N_5[117,118], InN[119], and InGaN[120] have been used as potential semiconductor photocatalysts for water splitting due to their simple chemical composition, tunable narrow band gap and stability.[49] In addition, some metallic nitrides such as TiN[121], Fe_xN[122], Co_xN[109,123], Ni_3N[124,125], Mo_xN[126,127], VN[128] and some relative ternary compounds are suitable as cocatalysts because they can act as active sites and promote the transportation of photoexcited electrons. Therefore, TMN is a type of material with a significant prospect for extensive applications in photocatalytic systems. Some examples are shown below.

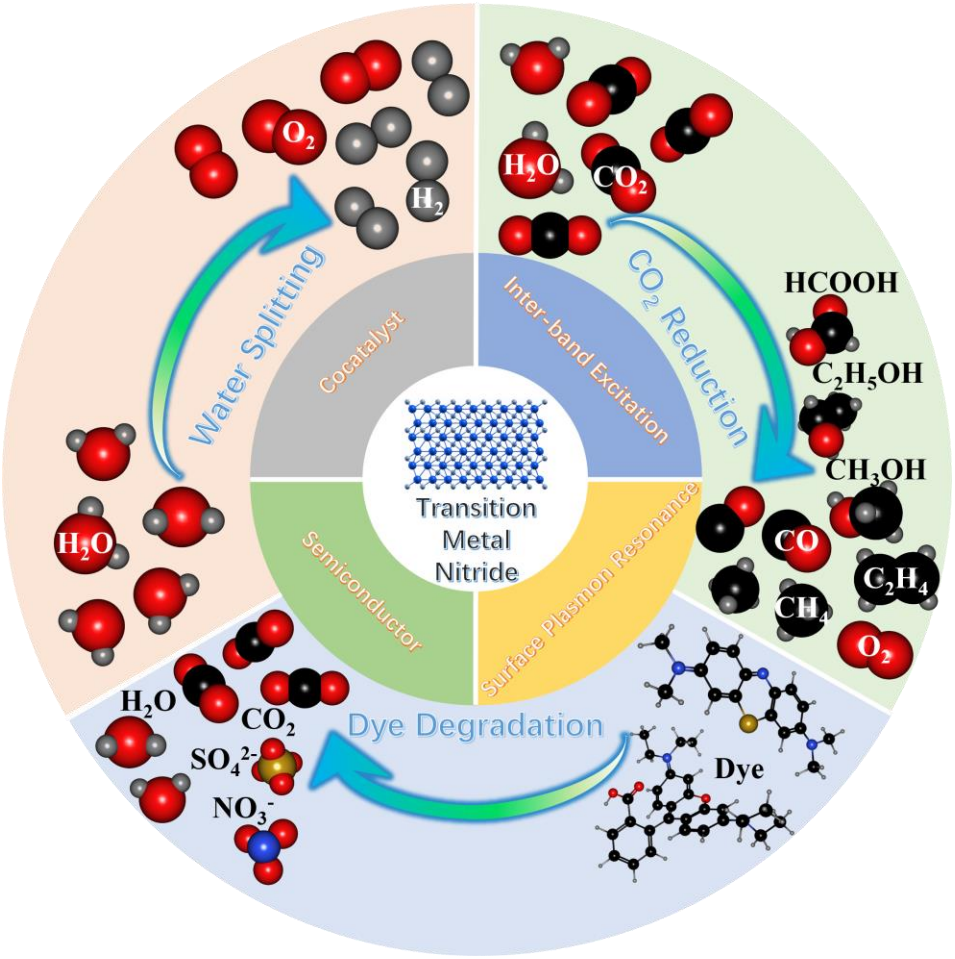

Figure 1.7 The different roles and application fields of TMN materials in photocatalysis.

Semiconductor type Transition metal nitride. Traditional semiconductors (oxide semiconductors) usually exhibit relatively low electronic conductivity and wide band gap, the separation of photoexcited carriers is inefficient and the light harvest is rather inefficient.[39] Therefore, the technological applications of semiconductor-based photocatalysts are always limited.[39] It is important to modify the band structure of semiconductors photocatalysts so that the light absorption would be improved.[129] TMNs with a narrow band gap and great physicochemical properties have become a considerable choice for improving the structures and properties of semiconductor catalysts.

The crystal structural modification has a significant impact on the activity of Ta-based nitrides in photocatalysis. Wang *et al*. have found that the rapid growth of single-crystal Ta_3N_5 nanorods on lattice-matched cubic $KTaO_3$ particles can significantly promote the process of overall splitting water.[117] The growth of nanorods is obviously shown on cubic particles. Each Ta_3N_5 nanorod is a single crystal and the atoms are regularly arranged from the surface to the interior (**Figure 1.8a** and **b**).

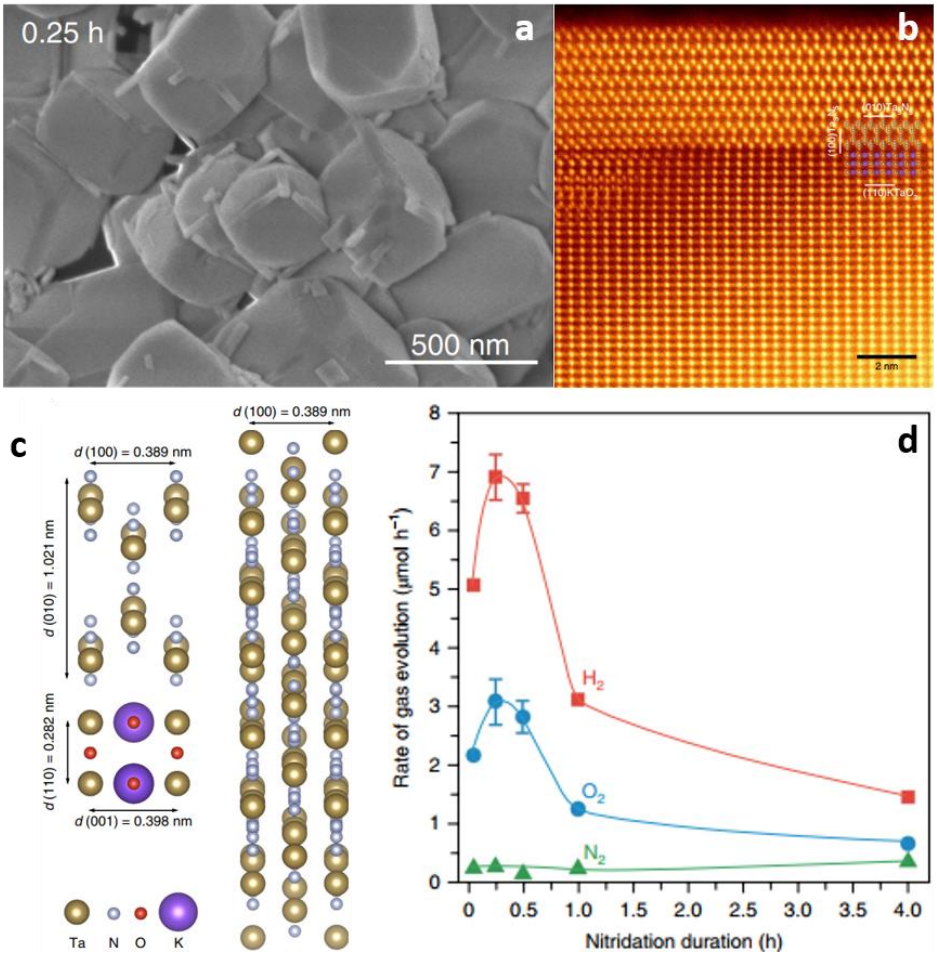

Figure 1.8 (a) SEM image of $Ta_3N_5/KTaO_3$ synthesized with nitridation times of 0.25 h. (b) Colorized and magnified ADF-STEM images of a Ta_3N_5 nanorod in $Ta_3N_5/KTaO_3$ synthesized with a nitridation time of 0.25 h viewed from the [001] direction of the Ta_3N_5. Insets: depicted crystal structures of Ta_3N_5 projected from the [001] direction and $KTaO_3$. (c) Crystal structures of Ta_3N_5 projected from the [001] (top left) and [041] (right) directions, and $KTaO_3$ projected from the [1-10] direction (bottom left), *d* indicates the interplanar distance. (d) Gas evolution rates during overall water splitting as functions of the $Ta_3N_5/KTaO_3$ nitridation time, with 0.05 wt% rhodium loading on $Ta_3N_5/KTaO_3$.[117]

The crystal structural models of Ta_3N_5 and $KTaO_3$ have been presented in **Figure 1.8c**

to indicate their facets. When combined with Rh/Cr_2O_3 cocatalyst, it has considerably high efficiency of the evolution of H_2 and O_2 (~9 μmol h^{-1} of H_2 and ~4 μmol h^{-1} of O_2) (**Figure 1.8d**). The rapid-nitridation process in this case leads to the forming of large size of Ta_3N_5 nanorods and the surface defect states in single-crystal phase. They particularly choose $KTaO_3$ as the nitridated precursor and the base of Ta_3N_5 nanorods growth. This is because these two materials have very similar and matched lattice structures, which contribute to the tight and clear grain boundaries between them.[117] The volatilization of potassium species of the $KTaO_3$ can control the substitution of nitrogen atoms for oxygen atoms and also promote the evolution of discrete Ta_3N_5 nanorods single crystal phase.[117] The small size of Ta_3N_5 crystal and the simple arrangement of atoms make charge transfer faster. The cocatalyst shells make the active sites of photocatalytic reaction nearer to the surface, hence the active site concentration also increases. These results have proven that optimal nanostructure single-crystal photocatalysts can act an important role in overall water splitting.

In addition, different morphological controls also influence the photocatalytic activity of Ta nitride. Xiao *et al*. have synthesized a new type of single-crystal ultrathin (~2 nm) The monoclinic Ta_3N_5 with a nanomesh morphology, which has a high level of crystallinity and a large surface area (284.6 m^2 g^{-1}) (**Figure 1.9a**, **b** and **c**).[130] This kind of material exhibits improved electronic conductivity and prolonged photocatalytic charge carrier lifetime in comparison with pristine Ta_3N_5 material, so it has much better efficiency in the photocatalytic hydrogen evolution process (~11.5 μmol h^{-1} of H_2

evolution amount, which is 10 times higher than that of bulk Ta_3N_5) (**Figure 1.9d**). It is believed that the substantial improvement of photocatalytic performance is attributed to the synergistic effects associated with an increase in the specific surface area and active sites based on the porous mesh structures.

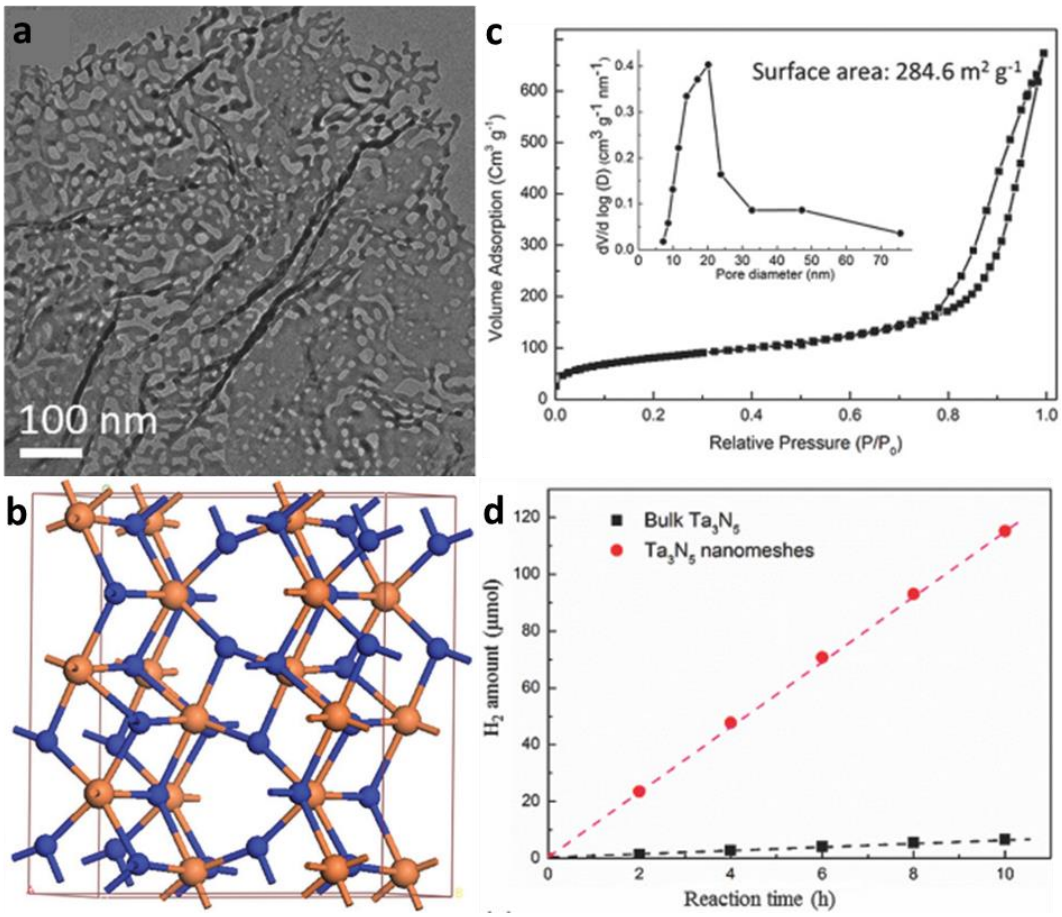

Figure 1.9 (a) TEM image of ultrathin Ta_3N_5 nanomeshes. (b) The simulated crystal structures of monoclinic Ta_3N_5. The grey dots and blue dots stand for Ta atoms and nitrogen atoms, respectively. (c) N_2 adsorption/desorption curve of Ta_3N_5 nanomeshes. (d) Photocatalytic H_2 evolution activity of bulk Ta_3N_5 and Ta_3N_5 nanomeshes under simulated sunlight irradiation (AM 1.5G, 100 mW cm^{-2}), respectively.[130]

Crystallinity is also crucial for performance because it affects photocarrier generation, recombination and migration. Thus, a type of ordered mesoporous Ta_3N_5 with a crystalline thin-wall structure had been synthesized, which achieves a 3 times higher activity (3.4 μmol h^{-1}) than that of bulk Ta_3N_5 under the same condition of loading 3 wt% Pt.[131] The mesoporous Ta_3N_5 material had a small dimension (4 nm pore size and 2 nm wall thickness) and a large specific surface area (100 m^2 g^{-1}). This kind of thin-wall structure promotes charge transfer to active surface sites in photocatalytic applications. These results validate the effectiveness of crystalline mesoporous nitrides. Another strategy of synthesized Ta_3N_5 with high crystallinity is to modify the surface of the precursor Ta_2O_5 with a small amount of alkaline metal such as Na_2CO_3.[132] The Ta_3N_5 which is obtained using nitridation of modified precursor has better crystallinity, smaller sizes and smoother surfaces. This sample of Ta_3N_5 has shown 6 times more O_2 evolution under visible light compared to that of traditional Ta_3N_5.[132]

In addition, general nitridation methods usually produce Ta_3N_5 with the morphology of aggregated bulk materials (size is larger than 100 nm), which limits their photocatalytic activity. Thus, the pattern of the NPs can also be considered as a kind of morphological control to improve the photocatalytic activity of Ta_3N_5. Ta_3N_5 NPs with different sizes (size of 7-24 nm) can be synthesized by using mesoporous C_3N_4 with a controllable pore size as a template.[133] The small particle size associated Ta_3N_5 with concomitant large surface area (61 m^2 g^{-1}) offers a higher activity (27.2 μmol h^{-1}) when compared to bulk Ta_3N_5 (2.9 μmol h^{-1}). In addition to the low particle size and high surface area, the

low density of defect sites would also lead to increased activity, because fewer defect sites would facilitate electron migration from the Ta_3N_5 bulk to the surface and/or electron transfer from the CB of Ta_3N_5 to the loaded cocatalyst.

Table 1.1 The BET surface area, band gap energy, and production rates of Ta_2O_5, Ta_3N_5, 1% V-Ta_3N_5, 2% V-Ta_3N_5, and 3% V-Ta_3N_5 materials.[134]

	Surface area (m^2/g)	**Band gap energy (eV)**	**Production rates (μmol g^{-1} cat h^{-1})**			
			CH_4	CO	O_2	H_2
Ta_2O_5	20.5	3.82	0	0	0	0
Ta_3N_5	21.3	2.09	224	152	508	18
1% V-Ta_3N_5	35.6	1.91	389	176	876	37
2% V-Ta_3N_5	40.7	1.82	425	236	1003	56
3% V-Ta_3N_5	46.8	1.81	403	214	927	43

Doping of other element components can also improve the efficiency of Ta nitride in photocatalytic reactions. For example, Dieu *et al*. have successfully synthesized Ta_3N_5 and V-Ta_3N_5 for CO_2 conversion to produce valuable fuels including CH_4, CO, H_2, and O_2, even under visible light.[134] The V dopants that exist in the Ta_3N_5 lattice reduce the band gap energy, which increases the electron-hole separation efficiency of the V-Ta_3N_5 photocatalysts. Therefore, the photocatalytic activity of the synthesized V-Ta_3N_5 is higher than that of the Ta_3N_5. However, the substantial increase in the V doping ratio results in the formation of VN particles distributed on the Ta_3N_5 surface. This blocks the light and reduces the number of photons reaching the photocatalyst, thus reducing its photocatalytic activity. The optimal V doping ratio in V-Ta_3N_5 is found to be 2 wt%

(**Table 1.1**). The production rates of CH_4, CO, O_2, and H_2 generated from the photocatalytic reduction of CO_2 by 2 wt% V-Ta_3N_5 under visible light are 425, 236, 1003, and 56 μmol g^{-1} h^{-1}, respectively.[134] This result also proves the potential of the Ta nitride application in photocatalysis.

Cu_3N has a special anti-ReO_3 crystal structure containing corner-shared Cu-N octahedra, which are arranged in the cubic lattice.[102] There exists a void in the center of the unit cell of Cu_3N, which can hold other transition metal ions. In addition, the narrow band gap of Cu_3N (1.4 eV) and its high optical absorption coefficient value (~10^5 cm^{-1}) are ideal for solar energy conversion.[135,136] Barman *et al*. have decorated Au NPs on the surface of Cu_3N semiconductor for photocatalytic degradation of organic dyes.[102] The colloidal Cu_3N nanocrystals with decorated surficial Au NPs cause the LSPR effect and the better charge carriers separation property are the two main reasons to promote the photocatalytic degradation processes.[102] The results prove that the coupling between metal and semiconductor in these nanoheterostructures can efficiently improve the activity of photocatalysts.

Besides, there is an abundance of literature on the use of Ga-based nitrides in photocatalysis. GaN is a type of bulk nitride material with d^{10} electronic configuration that is active in overall water splitting, and it has a wide band gap of 3.4 eV.[137] GaN and its related oxynitride are an important family of materials due to the insights they offer between composition, structure and photocatalytic activity.[138] For example,

Domen's group has reported the overall splitting water property of GaN. The groups of Ooi and Mi have introduced Indium (In) to synthesize InGaN and narrow the band gap of GaN, and Li's group has synthesized a (oxy)nitride composite (InN/GaZnON) for photocatalytic water splitting.[119,120,138–142] However, Ga belongs to IIIA group instead of transition metal elements, so it would not be discussed in detail in this thesis.

Transition metal nitrides used as cocatalysts. Recently, a variety of TMNs has been reported as co-catalysts with their considerable activity of different applications. For instants, the nitrides of Ti, Co, Ni, Fe, Mo, V and Nb are used for water splitting, organic degradation and so on with achieving high efficiency. They can provide a large number of active sites and promote the separation of photoexcited electrons and holes.

Zhou *et. al.* have reported a synthesis strategy to produce oxidized TiN NPs, which possesses an active performance and an extended stable period.[121] In comparison to the rutile phase of such a compound, this oxidized TiN photocatalyst is able to provide superior H_2 evolution activity without the use of any noble metal cocatalyst. The sufficient small TiN nanopowders (~20 nm) have been used to produce the thermodynamically stable polymorph anatase phase of a TiO_2:Ti^{3+}:N compound. For pure titanium nitride as the photocatalyst, no H_2 evolution could be detected. The optimal synthesis condition of oxidized TiN is tested as 400 ℃ in 1 h and the H_2 evolution rate achieves ~75 μmol g^{-1} h^{-1} (**Figure 1.10a**). During the oxidization process of TiN, the combination of Ti^{3+}-state and nitrogen is formed. This leads to a remarkably

stable catalytic center for H_2 evolution. The oxidized TiN has maintained its activity for ~4 months while the samples of reduced anatase exhibiting a rapidly decreasing performance (**Figure 1.10b**). The electron paramagnetic resonance spectroscopy has further confirmed the remarkably stable photocatalytic activity observed from these samples for a long period, and further supported the concept of Ti^{3+} related defect structure capable of acting as the cocatalytic center in H_2 production reaction.

Meng *et al*. fabricated the ternary nitride $Cr_{0.5}Ti_{0.5}N$ NPs with CdS semiconductor as the base.[30] They attained the best photocatalytic H_2 production rate of 2.44 mmol g^{-1} h^{-1}, which is ~120 times higher than that of pure CdS sample and even higher than that of Pt-based nanocomposites (2.06 mmol g^{-1} h^{-1}) (**Figure 1.10c**). Thus, it is proved that Cr-Ti ternary nitride has much better photocatalytic efficiency than those of the binary nitride of Cr and Ti. The sample of CrN-CdS has the highest photocurrent densities and the smallest resistance (**Figure 1.10d**). The sample of TiN exhibits the lowest H_2 evolution over-potential and the highest electrochemical double-layer capacitance (**Figure 1.10e**). However, the $Cr_{0.5}Ti_{0.5}N$ exhibits the highest photocatalytic H_2 activity even in different photocatalytic systems (TMN-Eosin Y and TMN-CdS), which is due to the synergistic effect of Cr and Ti atoms in the compound. This has been rationalized using the DOS plots. These plots demonstrate that the d orbitals of the Cr and also Ti near the Fermi level greatly contribute to the total DOS (**Figure 1.10f**). This means the electronic state of the energy region near the Fermi level is mostly dominated by the orbital electrons of two kinds of metal atoms, which indicates metallic bonding. All

these results demonstrate the synergistic effect between Cr and Ti in this ternary nitride, and the experimental results are in accord with the theoretical indication.

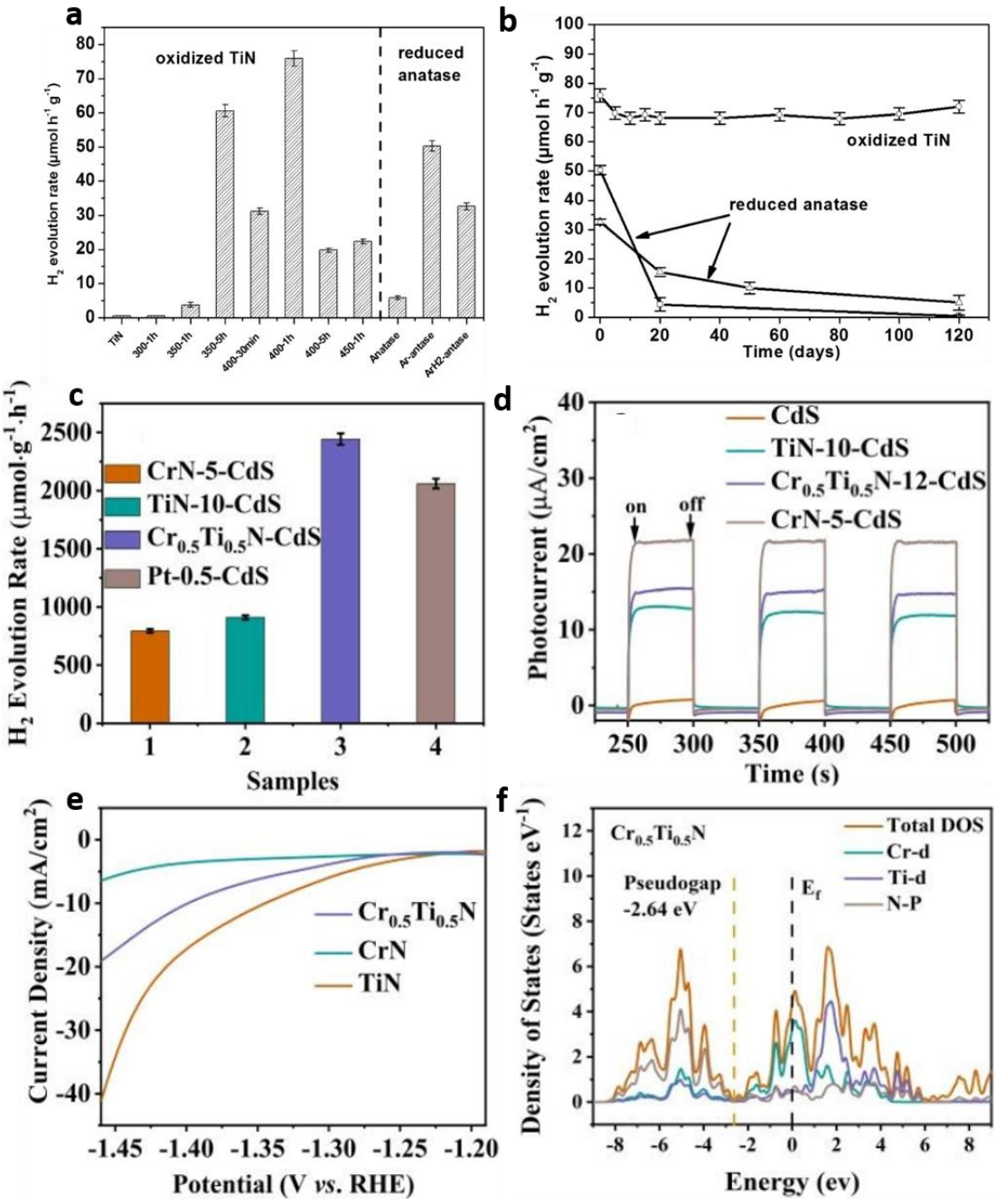

Figure 1.10 (a) Open-circuit hydrogen generation for oxidized TiN nanopowders treated at different temperatures in air and comparison to reduced anatase samples as a reference. (b) Stability of photocatalytic H_2 evolution for oxidized TiN (400 ℃, 1 h)

and reduced anatase (Δ: Ar/H_2 500 ℃, 3 h; □: Ar 500 ℃, 3 h). (c) Photocatalytic H_2 production activity of different samples for 2 h light irradiation. (d) Transient I-t curves without bias potential. (e) Polarization curves for TMNs. (f) Total and partial electronic density of states calculated for $Cr_{0.5}Ti_{0.5}N$.[30,121]

Cobalt-based nitride is also a type of promising co-catalyst which is a noble metal substitute for photocatalytic applications.[143] Chen *et al*. reported that Co_3N can be synthesized and used as a cocatalyst for enhanced photocatalytic H_2 production (~137.33 mmol g^{-1} h^{-1}) and apparent quantum yield (~14.9% at 450 nm) in water based on CdS nanorods.[123] Similarly, Jin *et al*. successfully decorated Co_3N NPs on ternary metal sulfide photocatalyst $Zn_{0.5}Cd_{0.5}S$, which achieved a H_2 production rate of 218.8 mmol g^{-1} h^{-1} under visible light and the apparent quantum yield of 30.2% at 420 nm.[143] This is due to the lower CB (-0.35 eV) of Co_3N and its excellent electron-conductivity, Co_3N NPs exhibit excellent electron capture ability.[143] The photo-generated electrons can be efficiently excited from the CB of the semiconductor to the surface of Co_3N, thereby effectively separating the photoexcited hole pairs (**Figure 1.11a**).[143] In addition, Co_3N and semiconductor photocatalyst have tightly combined to form a tight metal-semiconductor interface, thus also improving the electron transport efficiency. Thus, we can conclude that Co_3N could perform both the collection and transportation of electrons to extend the carrier lifetimes and improve photocatalytic activity.

Another type of Co-based binary nitride (Co_2N) has been applied as a novel cocatalyst

to promote photocatalytic CO_2 reduction by combining with BiOBr ultrathin nanosheets.[144] The authors reported considerable selectivity of CO formation rate of 67.8 μmol g^{-1} h^{-1} in pure water without sacrificial reagent or extra photosensitizer, which is 6 times better than that of pure BiOBr.[144] This is because of the unique surface configuration of Co_2N, which generates a strong electronic interaction with BiOBr, which is able to steer the electron transfer from the semiconductor photocatalyst. Electrons thus can transfer across the interface and arrive at the surface of the cocatalyst. The activation energy barrier can be lowered on the Co_2N surface via stabilize COOH* intermediates, tuning the rate-limiting step from the formation of COOH* on BiOBr to the formation of CO* on Co_2N, jointly optimize the CO_2 photoreduction activity.[144]

Compared to binary Co-based nitride, anti-perovskite phase Co_3ZnN that is formed by zinc atoms replacing the cobalt atoms at the apex of the cubic unit cell has improved electronic properties (**Figure 1.11b**).[145] DFT calculations reveal that the electronic structure of Co_3ZnN can be tuned by introducing zinc atoms (**Figure 1.11c**).[145] It is clear from these plots that the calculated d-band center of Co_4N and Co_3ZnN are -1.78 eV and -1.87 eV relative to the Fermi level, respectively. Therefore, the lower antibonding energy states of Co_3ZnN are lowered further, and the d-band center of Co_3ZnN becomes more negative, thus moving farther away from the Fermi level.[145] These electronic changes might lead to a weakened interaction between the material surface and hydrogen. Meanwhile, this favors the desorption of hydrogen from the catalyst surface, thus benefitting hydrogen desorption.[146] As result, with the support of

carbon black, Co_3ZnN/C achieves the highest H_2 evolution rate of 15.4 mmol g^{-1} h^{-1}, which is over 6 times higher than that of monometallic Co_4N (**Figure 1.11d**).[145] This experimental result gives an ample demonstration of the concurrence with the theoretical calculation and provides a new guideline for optimizing TMN.

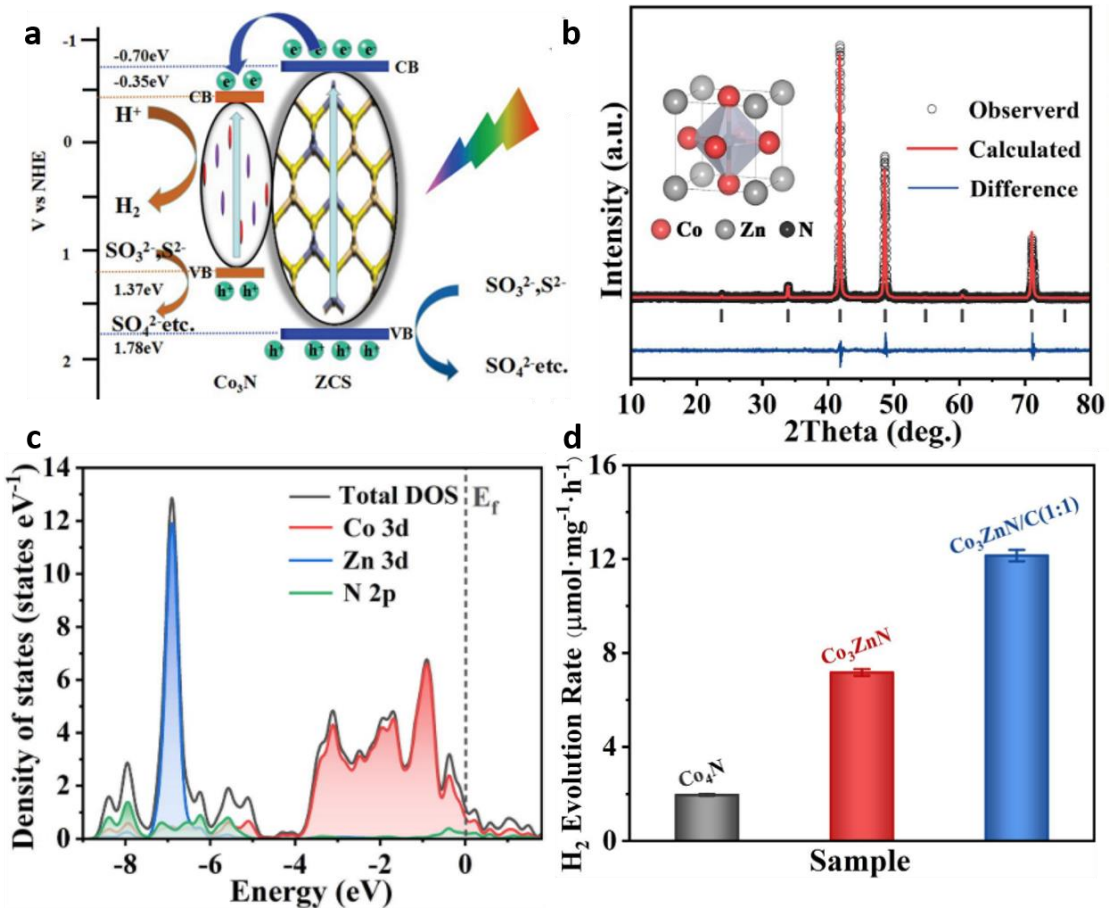

Figure 1.11 (a) Schematic illustration of the charge transfer and separation for the $Co_3N/Zn_{0.5}Cd_{0.5}S$ photocatalyst under visible light irradiation and the proposed mechanism for photocatalytic H_2 production. (b) The Rietveld-fitted X-ray powder diffraction pattern of Co_3ZnN. (c) Calculated electronic densities of states of Co_3ZnN. The Fermi level is set to zero. (d) The average rates of H_2 evolution under visible-light ($\lambda > 400$ nm) over as-prepared Co_4N, Co_3ZnN and Co_3ZnN/C (1:1) samples in Eosin

Y-TEOA system.[143,145]

In present photocatalytic fields, nickel-based nitrides have mainly been reported as cocatalysts for hydrogen production. The small Gibbs free energy ΔGH^* (65 meV) promotes the adsorption of protons on the surface of the Nickel-based nitride and at the same time promotes electron transportation to the adsorbed protons during the hydrogen production process.[124] In addition, Ni-based materials have a much lower price and higher abundance than noble metals. Thus, they are plausible replacements for noble metals in the construction of an artificial photocatalytic H_2 production system.[125]

Because Ni-based nitride is a type of metastable compound, which could be partially decomposed, it was usually binding chemically to stable photocatalysts such as CdS nanorod and g-C_3N_4 for application.[124,125] Sun *et al*. used a facile in situ growth method to grow Ni_3N on the semiconductor of the CdS nanorod.[125] The hydrogen production rate they have achieved (88 mmol g^{-1} h^{-1}) can be improved more than 10 times that of pure CdS nanorod. The result would be attributed to the interfacial charge transfer between semiconductor and Ni nitride cocatalyst.

Chen *et al*. also found that Ni_3N/g-C_3N_4 could achieve an H_2 evolution rate of 169 μmol g^{-1} h^{-1}, which is slightly higher than that of 3 wt% Pt modified g-C_3N_4 (152.0 μmol g^{-1} h^{-1}).[124] This is since Ni_3N NPs anchor on the g-C_3N_4 surface and form heterostructures

to promote the photogenerated electron-hole pair separation. This results in more photocatalytic active sites, thereby increasing the photocatalytic hydrogen evolution rate. Similarly, Qi *et al*. have synthesized a cocatalyst compound of Ni_3N with some oxidation impurities combined with g-C_3N_4 (**Figure 1.12a**), which approached a 54 times higher activity (151.5 μmol g^{-1} h^{-1}) when compared to the pure sample (**Figure 1.12b**).[116] They proved that the internal NiO impurities in Ni_3N can significantly improve the activity of photocatalytic reaction. This is owing to the formation of an all-solid-state Z-scheme photocatalytic system (**Figure 1.12c**). Moreover, they found that ammonia treatment can boost the hydrogen evolution rate due to the formation of reductive defects on the surface.

In addition, Meng *et al*. found that the Ni_3N-Au-TiO_2 sample with ultralow loading of Au clusters exhibits the most photocatalytic hydrogen production rate (87.7 μmol g^{-1} h^{-1}) compared with Ni_3N-TiO_2.[147] The excessive amount of Au clusters becomes charge carriers recombination centers of Ni_3N-Au-TiO_2 samples. It indicates that Ni_3N as support can efficiently decrease the loading amount of noble metal co-catalysts toward photocatalytic hydrogen evolution reaction.[147]

Ternary nitrides of Ni are also increasingly gaining prominence. Recently, Wang *et al*. synthesized a kind of Ni-Mo ternary nitrides based 1D hierarchical structure with In_2S_3 coating (In_2S_3-$Ni_{0.2}Mo_{0.8}N$(Ni) and In_2S_3-$Ni_{0.2}Mo_{0.8}N$) (**Figure 1.12d**).[148] The $Ni_{0.2}Mo_{0.8}N$ with metal Ni acted as an efficient cocatalyst that transfers the electrons

from the In_2S_3 to the interface between them, which promoted the separation of electrons and holes. This compound achieved a H_2 evolution rate of 614.2 μmol g^{-1} h^{-1} with the best ratio of 1 wt% cocatalyst composite. This is ~10 times higher than that of pure In_2S_3 (**Figure 1.12e**). In addition, the results demonstrate that pure $Ni_{0.2}Mo_{0.8}N$ shows higher co-catalytic properties than $Ni_{0.2}Mo_{0.8}N$(Ni), which indicates that the metal Ni impurity in the $Ni_{0.2}Mo_{0.8}N$ lowers the cocatalytic ability of the ternary nitride.

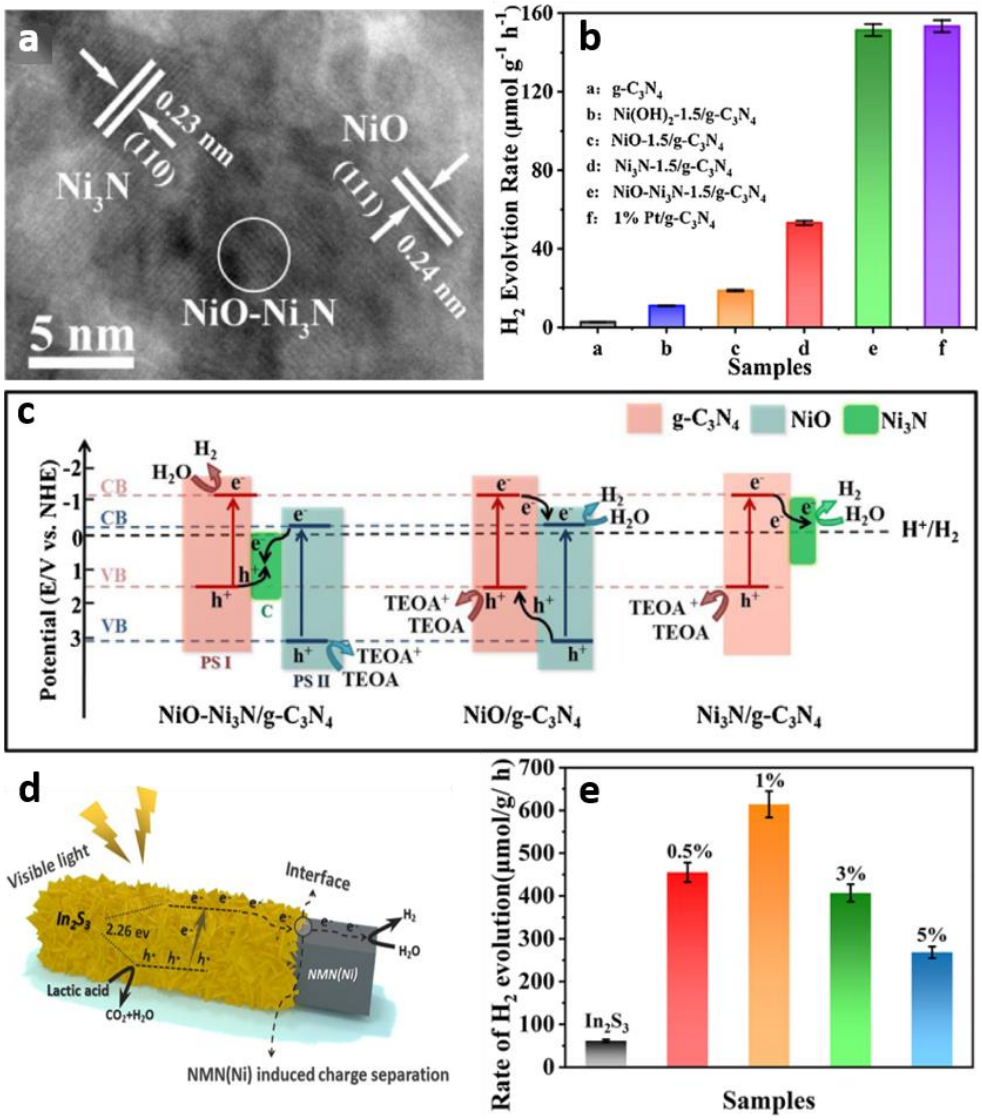

Figure 1.12 (a) High-resolution-TEM images of NiO-Ni_3N sample. (b) The comparison of the photocatalytic H_2 evolution activity of different samples under light irradiation.

(c) Schematic illustration of the photo-induced charge separation process in the NiO-Ni_3N/g-C_3N_4, NiO/g-C_3N_4 and Ni_3N/g-C_3N_4 composites. (d) Schematic illustration of Ni-Mo ternary nitrides-based one-dimensional hierarchical structures (In_2S_3-$Ni_{0.2}Mo_{0.8}N$(Ni)) that have been used to achieve visible light driven H_2 evolution. (e) The average rates of H_2 evolution under visible-light of In_2S_3, 0.5% In_2S_3-NMN(Ni), 1% In_2S_3-NMN(Ni), 3% In_2S_3-NMN(Ni), 5% In_2S_3-NMN(Ni), ($\lambda \geq 400$ nm).[116,148]

As a kind of alternative cocatalyst to noble metal, iron nitride with different ratios of Fe can act as an efficient photocatalyst based on different applications. Qi *et al*.[122] synthesized a type of MOF derived Fe_2N NPs for enhancing the photocatalytic H_2 evolution of g-C_3N_4, which achieves a rate of 88.7 μmol g^{-1} h^{-1}. This is almost 48 times that of pure g-C_3N_4 nanosheets. The loading of Fe_2N NPs obviously improves the efficiency of charge carrier separation and transportation on the surface. It also increases the active site density, improving the absorption efficiency of visible light, decreasing the overpotential of H_2 evolution and accelerating hydrogen evolution production.

Molybdenum-based compounds including molybdenum nitride have similar properties to Pt and are widely used in the hydrogenation and dehydrogenation process.[149] Molybdenum nitride is a type of compound with a gap alloy structure, which contains MoN, Mo_2N, and so on. These have noble metal-like properties, and hence are promising candidate cocatalysts in photocatalytic reactions.[150]

For the application of Mo nitride, Ran *et al*. designed and fabricated MoN ultrathin nanosheets with TiO_2 NPs, which form 0D/2D semiconductor/metal heterojunctions and improve the photocatalytic activity.[151] They achieved an optimal photocatalytic activity of 2034 μmol g^{-1} h^{-1} with 1.0 wt% loading of MoN. This improved activity is derived from the intimate electronic coupling between TiO_2 and MoN, high work function, excellent metallic conductivity, high surface area and abundant active sites.

There are several research activities Mo_2N is also a type of excellent cocatalyst for photocatalytic H_2 evolution. For example, Gong *et al*. reported that Mo_2N-based on ultrathin g-C_3N_4 nanosheet can perform a catalytic rate of 148 times higher than that of the pure precursor.[152] The result of g-C_3N_4 is because the 2D ultrathin layer morphology of g-C_3N_4 narrows the electron moving path, high charge transfer rate and more active sites exposed. In particular, the interaction between Mo_2N (111) planes and g-C_3N_4 (002) planes at the interface plays a crucial role in the improved catalytic performance.[152] Ma *et al*. found that when Mo_2N combined with CdS, the molybdenum oxides and $CdMoO_4$ formed between Mo_2N and CdS. This protected Mo_2N and inhibited the reversible reaction of H_2 production. Therefore, the photocatalytic activity and the stability of Mo_2N/CdS are increased.[153] Subsequently, this group compounded Mo_2N, Mo_2C, CdS and graphene to attain an 18 times higher hydrogen production rate than that of bare CdS.[149] This result demonstrates that the interface effect among the composites of Mo_2N, Mo_2C and CdS may lead to the superior

H_2 evolution property (**Figure 1.13a**). All of these studies emphasize the importance of interaction between interfaces and the formation of heterostructures.

In addition, modifying the morphology and orientations of Mo_2N can improve the capacitance of cocatalyst, thereby producing a better photocatalytic hydrogen evolution reaction.[127] Ma *et al*. discovered that *h*-Mo_2N rods with CdS can achieve the optimal photocatalytic efficiency compare to sheet and sphere shapes of Mo_2N, which is 30.1 times higher than that of the pure CdS (**Figure 1.13b**). This can be attributed to the lower overpotential that needs to overcome on rod morphology. The (111)-orientated *h*-Mo_2N rods have the largest capacitance and conductivity, which can store the photoexcited electrons and facile transfer of electrons, thus it has the superior cocatalytic performance.[154]

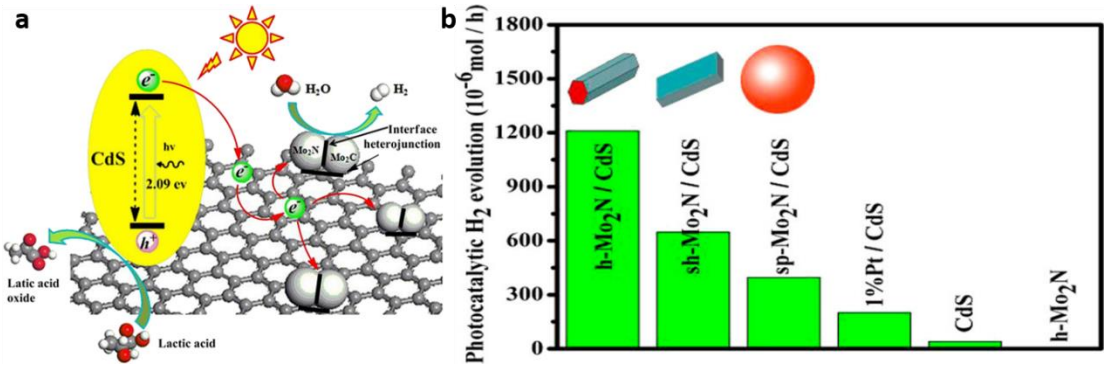

Figure 1.13 (a) The proposed mechanism of photocatalytic H_2 evolution reaction on $Mo_2N/Mo_2C/GR/CdS$. (b) Photocatalytic activities of CdS loaded with different morphologies of Mo_2N, Pt/CdS, CdS, and sole *h*-Mo_2N.[127,149]

For more TMNs used in photocatalysis, Tian *et al*. reported that VN can be applied as

a superior photocatalyst in water splitting.[128] In detail, VN-CdS photocatalyst can exhibit a high photocatalytic efficiency (6.24 mmol g^{-1} h^{-1}, 6.7 times higher than that of pristine CdS) (**Figure 1.14a**). This is because VN dramatically decreases the overpotential of CdS and makes it much easier to generate charge carriers, and inhibit the recombination of electrons and holes (**Figure 1.14b**). VN also shows considerable stability in photocatalytic reactions.[128] Qu *et al*. demonstrated that the lattice matching and the heterojunctions formed between metallic NbN and CdS improved the photocatalytic activity (10 times higher than that of bulk CdS) (**Figure 1.14c**). Theoretical calculations revealed that NbN possesses strong adsorption for H_2O on its surface. Thus, NbN is appropriate for photocatalytic hydrogen production, in particular after coupling with lattice-matched CdS.[155]

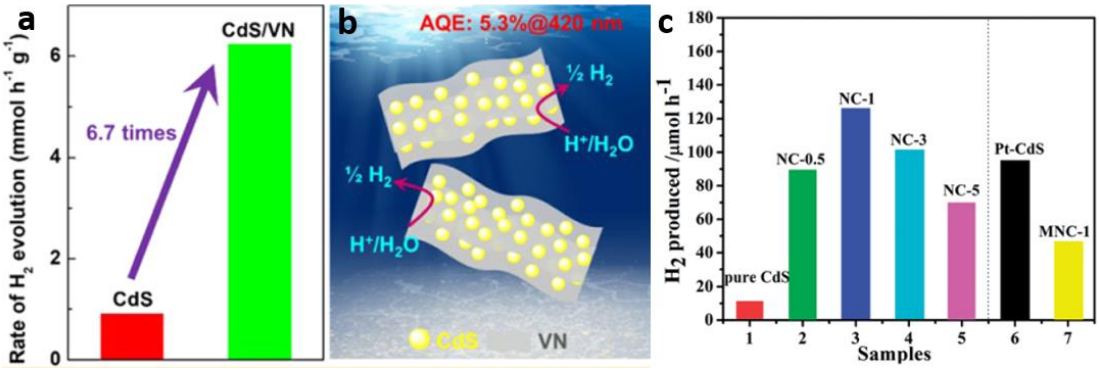

Figure 1.14 (a) Photocatalytic H_2 production activities of the VN/CdS sample compare to CdS sample. (b) The proposed mechanism of VN/CdS as a photocatalyst for water splitting. (c) Photocatalytic H_2 production activities of different samples.[128,155]

These results show that TMNs as cocatalysts can improve photocatalytic activity by

extending the visible light region, accelerating the electrons' conduction and decreasing the band gap between materials. Thus, they point out promising prospects in this field of applied photocatalysis. More types of TMNs that benefit photocatalysis are to be explored and researched.

1.3.4 Piezoelectric applications of TMNs

Due to the favorable properties and the adjustability of the d-band of TMN, this kind of material is also inferred as an ideal option to be utilized in the piezoelectric catalyst. However, since piezoelectric catalysis has developed for only a decade, a few pieces of research by utilizing TMN is published. The advantages of piezoelectric TMN are still in the process of exploration.

Guo et al. reported that the 2D group III compounds with buckled hexagonal configurations have been successfully synthesized.[156] They proved that the hydro-generated 2D nitrides (H-XN-H, X = Al, Ga and In) exhibit both the in-plane and out-of-plane piezoelectric effects in the monolayer and multilayer structure under an external strain. The relationships between the piezoelectric coefficients and their electronic, chemical and structural properties are clarified.[156] Thus, these results are able to promote the research of metal nitrides used in piezoelectric fields.

Besides, Zhang et al. have synthesized the non-noble metal Ni decorated single crystal GaN nanowires, which has 9 times higher hydrogen evolution rate than that of the pure

sample.[18] This performance is similar to that of the Pt decorated GaN nanowires. The large piezoelectric potential produced by the vibration on the small diameters (~100 nm) nanowires contributes to this superior piezoelectric catalytic efficiency.[18] This result has shown the promising perspective of piezoelectric application driven by weak mechanical energy from the environment.

1.3.5 Disadvantages and challenges of TMNs

Although TMNs have been utilized in various fields in photocatalysis and got ready to be used in piezoelectric applications, the realization of high-performance TMN catalysts for practical applications still faces a number of challenges. For instance, achieving a large-scale and reproducible synthesis of TMNs with controllable morphology and precise composition still remains a significant challenge. Generally, it is difficult to attain nitrides with considerable purity. Moreover, the pore structure and size of nanoparticles are controlled within a small synthesized scale. These problems are led by critical synthesis conditions and unstable forming processes during the nitridation. In particular, there is still a need for cost-effective and environmentally friendly synthesis methods which are also amenable to industrial production.

1.4 Porous materials and synthesis methodology for TMNs

1.4.1 Advantages of porous materials

As classic porous materials, ordered mesoporous materials and MOF have various advantages including high design flexibility, tunable pore channels, and the large ratio

of surface-to-volume.[157] **Figure 1.15** uses ZIF-67 as a sample to show the characteristics of MOFs. Besides the component, the morphology of the catalyst plays an important role in improving the catalytic performance. This is because the materials with ordered porous structures have a large specific surface area and high porosity, which can provide abundant active sites in the catalytic process.[158,159] In particular, the well-distributed nanoparticles are possible to further strengthen the synergistic effect between the guest species and host MOFs due to the enlarged interface.[160] Moreover, a well-developed porous network can further promote the diffusion of electrolytes and decrease the distance between the solution and the catalyst.[160]

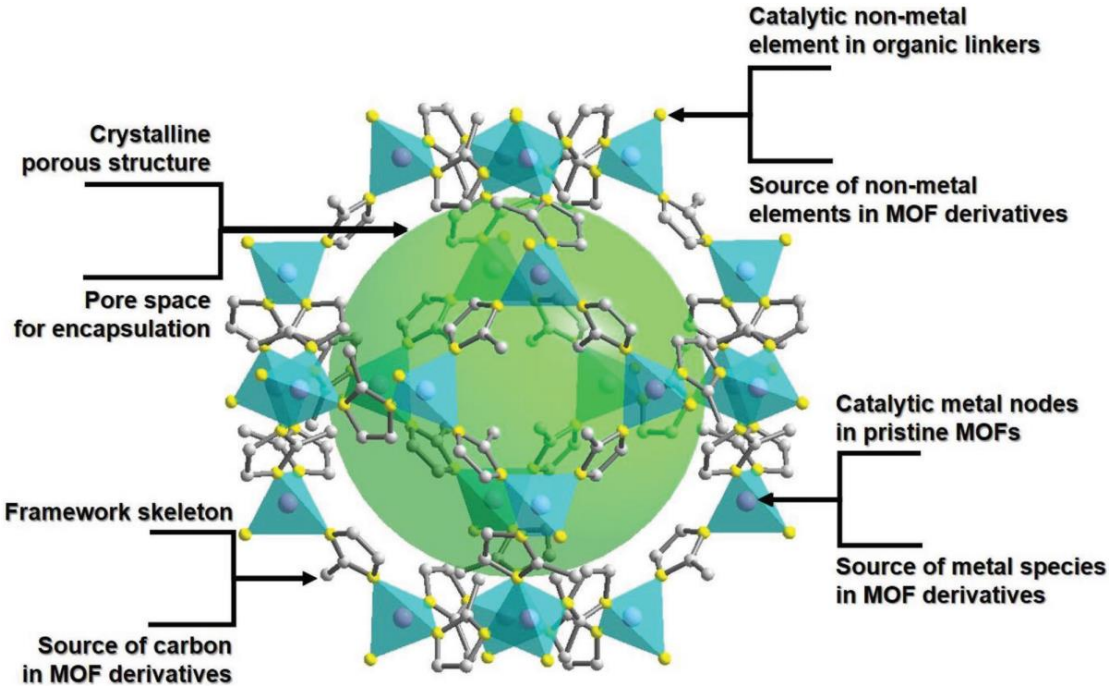

Figure 1.15 Key merits of MOFs as catalysts for HER (ZIF-67 is used here as an example, green ball: pore space; purple: Co; yellow: nitrogen; grey: carbon).[160]

So far, MOFs that consist of metal ions/clusters and coordinated organic linkers have

found uses in applications such as gas storage/separation, catalysis, sensing and drug delivery.[161–164] There are a number of publications proving the improving activity of MOF porous materials compared to that of corresponding bulk materials. For example, mesoporous Ni_3FeN and $NiCo_2N$ are found as high performance for OER.[165,166] In addition, a variety of photocatalysts such as ZnO and CdS have been synthesized by MOF precursors and used for photodegradation and hydrogen production with considerable performances, respectively.[167,168] Importantly, their high porosity and large specific surface area, as well as tunable pore size and morphology make them excellent sacrificial templates for fabricating porous MOF-derived functional materials.[169–171] For example, various MOF-derived porous carbon, metal oxides, metal sulfides, metal phosphates and their nanocomposites have been reported.[172–176] In these cases, MOFs have been used as both the precursor and porous template for the synthesis of catalysts.[177] Although ammonia treatment of MOF-derived metal/carbon nanocomposites can yield porous metal nitride/carbon composites; pure metal nitrides derived from MOFs with porous structures have been rarely reported. This is primarily due to the ease of collapse of the pore structures associated with MOF at high reaction temperatures, especially the case with long reaction times.[178,179] Thus, it can be inferred that maintaining the porous morphological structure of catalyst materials is crucial for achieving a highly efficient catalytic performance.[2,177]

1.4.2 Existing synthesized methodology for TMNs

Nitrogen or ammonia as the nitrogen source. In general, TMNs can be prepared by

maintaining a nitrogen-rich atmosphere over metal-based precursors. TMNs can be prepared from metal materials by direct calcination in the N_2 atmosphere at high temperatures. For example, vanadium nitride can be prepared at 1200℃ from metal powder or film by passing N_2 gas.[49] However, this direct synthetic route is limited by large thermodynamic barriers which are due to the making and breaking of the triple bond in dinitrogen (945 kJ mol^{-1} for N≡N).[180] It means that only highly thermally stable nitrides can be made by this method. Therefore, most nitrides are prepared using ammonothermal method at present. This means metal powder, oxides, hydroxide, halides and sulfides, *etc.* as metal-based precursors in an ammonia atmosphere at certain temperatures enable the synthesis of corresponding TMNs. Generally, ammonothermal method needs a lower temperature as compared to that prepared from using N_2 gas as the only nitrogen source. Through ammonothermal method, binary nitride, ternary nitride and nitride-based composites are widely synthesized and thereafter have been used in various fields.

In addition, fabricating metal-based precursors *via* different processes (*e.g.*, chemical reduction, solvothermal process, the electrospinning method, *etc.*), which is combined with ammonothermal method, allows for the synthesis of TMNs with unique characteristics. For example, Li *et al.* have developed an electrospinning method combined with ammonothermal method to fabricate 1D TMNs (TiN, VN, NbN nanofibers).[181]

Recently, a hard-templating approach (wherein mesoporous silica is the hard template used) has emerged as an attractive method to synthesize several mesoporous metal materials such as metal-oxide perovskites, sulfides and transition metal-phosphorus-based materials.[182–184] For instance, Y. Shi et.al. produced ordered mesoporous cobalt and chromium nitrides by using SBA-15; this yielded materials with very high specific surface area and an ordered arrangement of mesopores.[185] Jiang *et al.* used the KIT-6 template to prepare a three-dimensional ordered mesoporous cobalt nitride for fast-kinetics and stable-cycling lithium storage.[186] They used an impregnation method to prepare cobalt nitrate/KIT-6 precursor. Subsequently, calcination in air and etching by NaOH results in ordered mesoporous-Co_3O_4. Combined with ammonothermal method, the ordered mesoporous-CoN sample is prepared. Lai *et al.* designed the NiCoN/carbon hybrid nanocages composite.[187] These NiCo LDH nanoboxes are made from ZIF-67 nanocubes which are chemically etched using Ni^{2+} ions under sonication and then transformed into the NiCoN/C hybrid nanocages *via* an ammonothermal method. In this procedure, the precursor with a designed structure served as the template, which could be defined as the self-templating method.

In fact, metal-organic-framework (MOF) materials are increasingly used as metal-based precursors to fabricate TMNs due to the metal ions acting as a metal source in MOFs, which are isolated by the cage-like pores. This can significantly hinder their diffusion and agglomeration during pyrolysis.[188] Thus, upon annealing in ammonia, ultrasmall TMN nanoparticles (NPs) can be well obtained. For example, Chen and Ha

et al. use ZIF-67 as the precursor under an ammonia atmosphere at 700 ℃ and successfully prepare $Co_{5.47}N$ NP@N-PC powders.[189] Small particle size $Co_{5.47}N$ NPs were encapsulated by graphitic carbon layers, which shows excellent catalytic performance.

Nitrogen-based compounds as the nitrogen source. In addition to nitrogen or ammonia, nitrogen-based compounds can also be used as nitrogen sources for the synthesis of TMNs. Take urea, for example; when using it as the nitrogen source, ethanol is usually used to dissolve metal salts. But in some cases, metal salts do not dissolve in ethanol. If urea is added to it, dissolution increases. Urea can also form metal-ethanol-urea gels. When such gels are heated, TMNs can be produced at a relatively low temperature. For instance, Yuan *et al.* prepared ZrN NPs by a urea-glass route.[190] $ZrCl_4$ powder as the metal source was dispersed in ethanol, urea was added and the mixture was stirred until the urea dissolved and the solution was completely clear. The solution was aged for 12 h to complete the complexation of Zr by urea and the resulting colorless transparent sols. The sols are heated under an argon flow at 800 °C for 3 h, ZrN NPs can be obtained after cooling and passivating.

Compared with the ammonothermal method wherein synthesis is carried out by heating ZrO_2 in ammonia at temperatures above 1200 °C; the urea-glass route reduces the synthesis temperature, prevents aggregation and grain growth. Giordano's group uses a urea-glass route to fabricate titanium nitride.[191] And then they use TiN as a carrier to

prepare the TiN-Ni nanocomposites by impregnation method. This nanocomposite exhibits efficient catalytic activity for the hydrogenolysis of aryl ethers. In fact, Giordano's group uses this urea-glass route to fabricate a series of TMNs, such as molybdenum nitride (γ-Mo_2N), hafnium nitride (HfN) and Nitride nickel (Ni_3N), *etc*.[192–194] All of these TMNs exhibit excellent catalytic properties in the field of catalysis. Thus, urea-glass route has the advantages of simplicity, low cost and non-toxicity of the reagents, and so is very promising for scaling up to larger applications. In addition to urea, other nitrogen-based compounds (such as azide, cyanamide, melamine, dicyandiamide, *etc.*) can also be used as nitrogen sources to prepare TMNs by heating with metal salts.[195]

Deposition technique. Some deposition techniques, such as physical vapor deposition, chemical vapor deposition (CVD) and electrochemical deposition *et al.*, can also be used to prepare TMNs (usually as thin-film). Through deposition techniques, high purity nitrides film samples with controllable stoichiometry and composition can be produced. For instance, Kang *et al.* prepared nickel nitride (Ni_2N) film with a cauliflower-like nanostructure and tetrahedral crystal lattice on an FTO glass base using a reactive sputtering method under a N_2 atmosphere at room temperature.[196] Kreider *et al.* also used a reactive sputtering method to prepare thin-film nickel nitride catalyst (Ni_3N and Ni_3N dual-phase).[197] The Ni target was sputtered in a mixture of 75% Argon, 25% nitrogen plasma to deposit ~130 nm of Ni_xN. Murthy *et al.* fabricate a series of metal-doped molybdenum nitride films by magnetron co-sputtering technique.[198] Mo,

Cu, V and Ag are used as the metal targets while silicon and stainless steel plates are used as the substrates for the film fabrication. Ar and N_2 gasses were used as sputtering and reactive gasses respectively in the film deposition. However, the operations of these physical synthesis methods are complex, so it is not suitable for general synthesis.

CVD is a process whereby a solid is deposited from vapor by a chemical reaction that occurs on or near a substrate surface.[199] Cheng *et al.* reported a novel CVD method to directly synthesize single-crystalline TiN nanowires.[200] TiN nanowires are grown on a graphite bar substrate in N_2 atmosphere. Anion exchange resin D301 exchanged with $Co(NO_2)_6^{3-}$ ions and TiF_6^{2-} ions (D301-Co-Ti) was used as the precursor, acting as both Ti source and catalyst for the growth of TiN NWs. As-synthesized TiN NWs were single crystalline along the whole length with uniform 1D morphology.

TMNs can also be prepared by an electrochemical route.[49] In this method, molten salt (LiCl-KCl eutectic mixture) was used as an electrolyte. Dry NH_4Cl and $CrCl_2$ were added to a molten salt. The Nickel (Ni) plate was used as the working electrode. The counter electrode was a glassy carbon rod. The reference electrode is the Ag^+/Ag electrode. The thickness of the CrN layer increases as the applied potential becomes more negative. It is particularly noteworthy that this electrochemical route is performed at room temperature.

Salt-Assisted Synthesis TMNs. Salt-assisted methods are emerging technologies that

can be used for the fabrication of some special TMNs. The roles of the molten state salt are related to their specific properties, which can assist in the synthesis of those nitrides with special structures. Compared to carbide MXenes, nitride MXenes are difficult to prepare due to the higher formation energy of metal-nitrogen bonds.[201] Molten salt at a high temperature can selectively etch the Al layer from Ti_2AlC. Urbankowski *et al.* used salt-assisted synthesis Ti_4N_3 nanosheets.[202] Ti_4AlN_3 powder is mixed with a composite salt (LiF, NaF and KF), reacted at 550 °C for 30 min under Argon flow, and exfoliated in tetrabutylammonium hydroxide to obtain 2D $Ti_4N_3T_x$ (T = F, O, and OH). This approach could potentially be used to prepare other types of nitride MXenes from their corresponding MAX phases by a suitable molten salt assist. Except for selectively etching, molten salt also does other things to help the synthesis of TMNs. For example, Cheng *et al.* used molten salt that permit catalytic synthesis of a family of single-crystal 2D layered TMNs ($MoN_{1.2}$, $WN_{1.5}$, and $Mo_{0.7}W_{0.3}N_{1.2}$).[203] The molten salts in this method ($Na_2MoO_4{\cdot}2H_2O/K_2MoO_4$ and $Na_2WO_4{\cdot}2H_2O/K_2WO_4$) acted as catalysts instead of reactants, which are not consumed or transformed during the reaction but can facilitate the growth of 2D layered TMNs. In addition, molten salts as solvents promoted the formation of ordered structures and porous TMNs. Shalom *et al.* used dicyandiamide as the nitrogen source, for fabricating crystalline sponge-like nickel nitride by the calcination of dicyandiamide together with $NiCl_2$/LiCl salt melt mixture.[204]

Other strategies. Without a doubt, there are some other methods and techniques that

can be used to synthesize TMNs. For instance, Xie *et al.* fabricate the atomically-thin MoN nanosheets by liquid exfoliation of the bulk material.[205] Wu *et al.* prepared copper nitride nanocubes (Cu_3N) directly by a wet chemical method.[206] Zhang *et al.* directly synthesized cobalt nitride (CoN) by subjecting the Co_3O_4 to N_2 radio frequency plasma treatment at room temperature within 3 min.[207] More strategies to synthesize TMNs easily, quickly and cheaply are likely to be developed in the times to come.

1.4.3 Difficulties of synthesis methodology for TMNs

As mention in above sections, it is obvious that the TMN materials are traditionally synthesized by methods involves long-time, high-temperatures, long heating times, high pressure, or complex synthesized process. The products thus formed tend to have larger particle sizes instead of porous structure, which is oftentimes a requirement in several applications of energy storage and conversion. Hence these products are rarely suitable for catalytic purposes.[114,122,208–210]

Furthermore, conventional ammonothermal and nitridation techniques pose significant challenges to scalability. This in turn makes its relevance to industrial applications. However recently, due to synthetic developments, TMN materials can be synthesized in the nano-regime with different morphologies.[114,122,211–214] Currently, both (i) low temperature, rapid and high yield methods of preparation, and (ii) nanosizing is imperative for the eventual success of TMNs in catalysis, and related areas. In particular, there is value in developing methods that enable the production of porous 3D TMNs

using soft chemical approaches. Clearly, the development of such a technique merits further attention.

In conclusion, it is important to explore a suitable and simple synthesized method for enabling low-pressure rapid preparation of TMNs while keeping their ordered porous morphology, for improving their performance in catalytic processes.

1.5 Thesis Structure

Based on the above introduction and discussion, the purpose of the research of this thesis is to explore a new strategy of synthesis for TMNs while maintaining their porous morphology. Then, these produced functional TMNs are used for hydrogen production through photocatalysis and piezoelectric catalysis. Finally, the d-band structure and the component of these catalysts can be tuned by doping elements for improving their activity. The details are listed below:

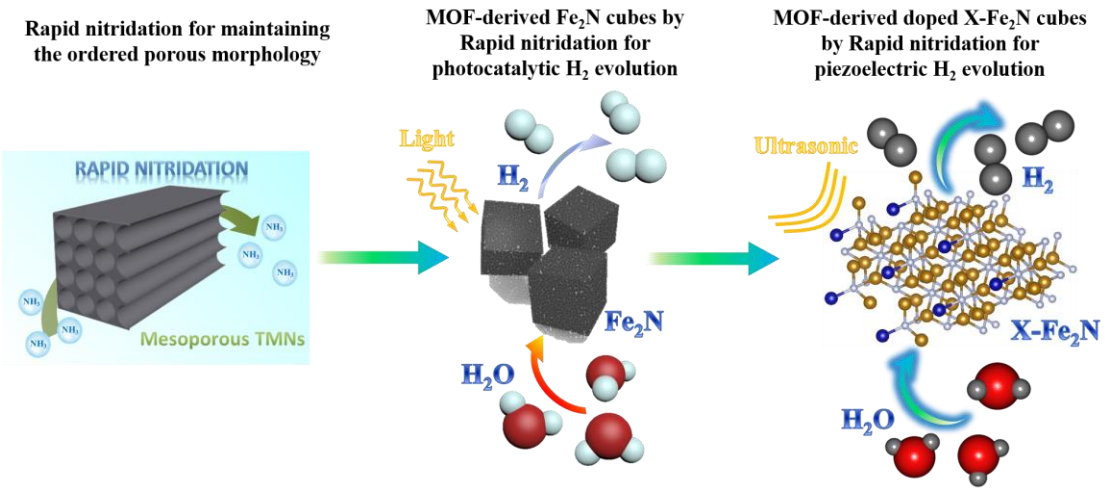

Figure 1.16 The logic flow chart of three parts research.

(1) A new hard template/rapid-nitridation method for the synthesis of ordered mesoporous metal nitrides had been reported, which was based on a nanocasting-thermal nitridation process. The hard template of 2D ordered hexagonal mesoporous SBA-15 was used to derive the mesoporous structure of products. A series of TMNs with ordered and regular mesoporous structures had been successfully synthesized. It was proved that this rapid synthesis method was necessary and in fact generically useful for the production of various TMNs to maintain their ordered porous structures. Thus, as a newly created methodology, rapid-nitridation is valuable for simply producing regular nanostructural TMNs.

(2) As a type of famous MOF porous material, PB was selected as the precursor to obtaining pure porous Fe_2N nanocubes with maintaining the MOF pattern and structure. The process applied two-step operation including oxidation and rapid-nitridation mentioned above. The produced samples were sensitized by using EY in photocatalytic HER. The Fe_2N with cube-like morphology had achieved an excellent high H_2 evolution rate, which was rationally higher than that of the nanoparticle sample. This performance was duly rationalized by DFT-based calculation and the reason for metallic nature was also duly elaborated.

(3) Based on the results of the last part, a series of PB-derived Fe_2N with different types of doped elements (Co, Cr, W and V) were successfully synthesized. The synthesized

method of rapid-nitridation had been applied again to produce the samples with cube-like morphology. These doped Fe_2N samples had been utilized for piezoelectric catalytic H_2 evolution and the Co-doped Fe_2N had achieved the highest activity. It was proved that the doping ratio would influence the catalytic performance critically.

Furthermore, morphology was found be to another important factor for the piezoelectric performance because the nanocubic sample had a much higher H_2 evolution rate than that of the nanoparticle sample. These doped Fe_2N catalysts also had the ability to degradation of different types of dye, while improving their H_2 production efficiency. In addition, the reason for the improved activity of doped nitrides had been demonstrated by the DFT calculation.

In summary, this thesis reports several ordered porous TMN materials. They have exhibited considerable activity and properties in the application of H_2 evolution. The relationship between the performance and the morphology as well as nanostructure has been demonstrated. These results provide the possibility for further research of TMNs used in more fields.

Chapter 2

Methodology and Techniques

2.1 Synthesis methods

2.1.1 Reagents

All chemicals were analytical grade and obtained from commercial suppliers and used without further purification. Nonionic triblock copolymer Pluronic P123 (M = 5800) was purchased from Sigma-Aldrich, Inc. Potassium hexacyanoferrate (II) trihydrate {$K_4[Fe(CN)_6]•3H_2O$, AR}, Polyvinylpyrrolidone K30 {$(C_6H_9NO)_n$, GR}, Hydrochloric acid (HCl, AR), Ferric nitrate nonahydrate ($Fe(NO_3)_3•9H_2O$, AR) and ethanol (C_2H_5OH, AR) were purchased from Sinopharm Chemical Reagent Co., Ltd. Cobalt nitrate hexahydrate ($Co(NO_3)_2•6H_2O$, AR), chromic (III) nitrate nonahydrate ($Cr(NO_3)_3•9H_2O$, AR), phospho-tungstic acid hydrate ($H_3[P(W_3O_{10})_4]•xH_2O$, AR), Sodium tungstate dihydrate ($Na_2WO_4•2H_2O$, AR), Sodium metavanadate ($NaVO_3$, 99.9%), Triethanolamine (TEOA, $C_6H_{15}NO_3$, AR) and tetraethyl orthosilicate (TEOS, $C_8H_{20}O_4Si$, AR) were purchased from Aladdin Chemical Co., Ltd. Nickel nitrate hexahydrate ($Ni(NO_3)_2•6H_2O$, AR) was purchased from the Tianjin Kermel Chemical Reagent Co., Ltd. Eosin Y disodium salt ($C_{20}H_6Br_4Na_2O_5$, RG) was purchased from Adamas Reagent, Ltd.

2.1.2 Synthesis of mesoporous materials

Synthesis of SBA-15 Mesoporous Silica. Mesoporous SBA-15 hard template was synthesized following the procedure described by Zhao et al.[215] First, 3 g of nonionic triblock copolymer Pluronic P123 was dissolved in 16.5 mL of HCl (12 mol L^{-1}) and 112 mL of water. Then the solution was vigorously stirred for 3 h at 40℃. After the

complete dissolution of Pluronic P123, 7.427 g of TEOS was rapidly added to the acidic solution under continuous stirring. A synthesized gel was obtained after the mixture was allowed to stand for 24 h at 40℃; then the mixture was heated at 90℃ for 24 h under static conditions. The precipitate obtained after filtration was subsequently washed and dried. Finally, the template was removed from as-synthesized SBA-15 by calcination (550℃, 8 h).

Synthesis of Ordered Mesoporous TMOs. Ordered mesoporous oxides were synthesized following a nanocasting route using SBA-15 as the hard template route, following Deng et al.[216] Typically, 0.5 g of SBA-15 and 0.8 mol L^{-1} of metal nitrates were used as precursors (*i.e.* $Co(NO_3)_2•6H_2O$, $Ni(NO_3)_3•6H_2O$, $Cr(NO_3)_3•9H_2O$, and $Fe(NO_3)_3•9H_2O$). Tungsten oxide was the only exception wherein the starting precursor used was phosphotungstic acid hydrate $H_3[P(W_3O_{10})_4]•xH_2O$), which was dissolved in 3.6 mL of ethanol.

To synthesize mesoporous mixed oxides, we used a similar process to the one described above. The only difference being that in this case, a ratio of 3:1 for $Ni(NO_3)_3•6H_2O$ and $Fe(NO_3)_3•9H_2O$ was applied respectively. After 30 min of stirring at room temperature, ethanol was removed using evaporation through heating of the mixture (overnight at 60℃). Thereafter, the resulting precursor filled mesoporous silica composite was heated in a ceramic crucible at 250℃ for 4 h to completely decompose the nitrate species. The impregnation step was repeated with the metal salt solution according to

the above procedure in order to achieve higher loadings. After the evaporation of the solvent, the resulting metal precursor/silica composites were calcined at 550℃ for 6 h. The silica template was removed by treatment with 2 mol L^{-1} NaOH solutions. This was followed by several washes with deionized water and ethanol; thereafter the material was vacuum dried at 60℃. Then the TMO samples were attained.

Synthesis of Ordered Mesoporous TMNs. Ordered mesoporous nitrides were synthesized from the corresponding nanostructured mesoporous oxides. The resulting mesoporous oxide (10 mg) was put in a quartz boat and then placed in the middle of a long quartz tube. After that, the air was pumped out and ammonia was filled into the tube; this process was repeated at least 3 times. Next, the temperature programming started after making sure that the furnace was placed in the right position, enabling homogeneous hydrothermal nitridation. Thereafter, when the setting temperature had reached, we waited for ~10 min (or more) for confirming its stability. Notably, it started to record the reaction time when the tube furnace was pushed to the position of the sample and starts heating.

For the materials studied in this work, these conditions were applied: heating 330℃ for 15 min of CoN, 600℃ for 10 min of WN, 800℃ for 30 min of CrN and 380℃ for 30 min of Ni_3FeN. The furnace was then cooled down naturally to room temperature in ammonia. The mesoporous nitride samples were duly collected. This process is called rapid-nitridation.

2.1.3 Synthesis of photocatalysts and piezoelectric catalysts

Synthesis of MOF PB cubes and elements doped PB cubes. Potassium hexacyanoferrate (II) trihydrate (0.1 g) {$K_4[Fe(CN)_6]•3H_2O$} and Polyvinylpyrrolidone K30 (3.8 g) {$(C_6H_9NO)_n$} were dissolved in 50 mL, 0.1 mol L^{-1} HCl solution. The solution was then vigorously mixed and stirred for 30 mins at room temperature. Subsequently, the solution was moved to a hydrothermal vessel and heated for 24 h at 80°C. The precipitates were collected by vacuum filtration or centrifugation and washed extensively using deionized water. Finally, the precipitates were dried at room temperature. The product thus obtained was MOF PB cubes. To synthesize elements doped PB cubes (Co, Cr, W, V for doping), the mole ratios of Co, Cr, W and V were regulated as 5 at% (15 at% also for V) of Fe element by adding the corresponding amount of $Co(NO_3)_2•6H_2O$, $Cr(NO_3)_3•9H_2O$, $Na_2WO_4•2H_2O$ and $NaVO_3$ into the HCl solution, respectively.

Synthesis of oxide and nitride cubes. As-synthesized PB or doped PB (0.1 g) was put in a quartz boat and dispersed to achieve a well-distributed state. The boat was then put in a muffle furnace and the temperature ramp was set at 1°C min^{-1}. When the temperature reached 350°C, the sample was allowed to soak for 1 h.

Subsequently, 10 mg of the oxide obtained was moved to the middle of the tubes. The tube was placed in a rail tube furnace. After that, the air was pumped out and the tube

was filled with ammonia. This was repeated thrice, to avoid oxygen contamination. When the temperature approached 400℃, the sample was allowed to soak for ~10 mins for confirming the stability of the temperature. The reaction time of rapid nitridation was 30 mins, subsequent to which Fe_2N or doped Fe_2N (Co, Cr, W, V for doping) was produced. Then the sample obtained was used for measurements.

2.2 Structure characterization

2.2.1 Characterization of Samples

XRD measurements were performed using a powder X-ray diffractometer (Rigaku Miniflex 600) with Cu-K_α radiation (λ = 1.54178 Å). The 2θ range was set from 10° to 80° and the measurements rates were kept at 1° min^{-1}. The small-angle XRD measurements were carried out using an X-ray diffractometer (D8 Advance Davinci) with Cu-K_α radiation (λ = 1.54178 Å) in the 2θ range from 0.3° to 5° at 1° min^{-1}.

The morphological structure and microstructures of the samples were characterized using SEM (FE-SEM, Hitachi S4800, Japan) and TEM (JEOL model JEM 2100 EX instrument) measurements. In addition, the high-resolution TEM, the SAED and elemental mapping measurements were also characterized using the same TEM instrument.

The diffuse reflectance spectra of the samples were measured in the range of 200-800 nm using a UV-Vis spectrophotometer (UV-Vis DRS, Hitachi U-3900, Japan) equipped

with an integrating sphere attachment.

XPS was performed using an AXIS Ultra DLD (Shimadzu, Japan) spectrometer with Al K_α excitation (1486.6 eV); Carbon was used as the internal standard (C1s=284.9 eV).

Nitrogen adsorption using BET area method (Micromeritics ASAP 2010, USA) was used to process the surface area measurement, whereas the pore size was assessed by the Barrett-Joyner-Halenda (BJH) method from the desorption branch of the isotherm.

2.2.2 Characterization principles

X-ray diffraction.[217] The periodic arrangement of atoms in 3D space would form the crystalline materials. Diffraction is a kind of scattering phenomenon. If the wavelengths of waves are similar or smaller than the diffracting object size at the atomic level, the diffraction would occur. The electrons that decelerate sharply would radiate high frequency electromagnetic waves, so the X-ray is produced when high-speed moving electrons collide with the anode target. The anode target is usually selected to be Cu-K_α. Because the X-ray has a short enough wavelength, the crystal can be used as a spatial diffraction grating for X-rays. A beam of X-rays passing through the crystal would be diffracted; thereafter the superposition of diffracted waves would strengthen or weaken the intensity of rays in different specific directions. This phenomenon can be utilized to study the crystal structure and obtain detailed information on the chemical composition. The distribution of diffraction patterns is exclusive and determined by the

size, shape and orientation of the unit cell. The intensity of the diffraction line is determined by the atom types and their position in the unit cell.

Bragg's equation is a simple expression of the relationship between the diffraction line direction and crystal structure.

$$2d_{hkl}sin\theta = n\lambda$$

where d is an interplanar spacing, θ is the incident beam angle, n is an integer given by the diffracted beam order, λ is the X-ray wavelength, 2θ is the diffraction angle, hkl is the Miller indices, which can characterize the sets of parallel atomic planes and influence the diffraction peaks (**Figure 2.1**).

The crystal planes have characteristic d-spacings in a different orientation for a specific crystal. When the monochromatic beam strikes the crystal at an angle theta θ, the diffraction only occurs when the d-spacing equals an integer of the wavelengths nλ. Different θ can lead to different d-spacings that satisfy Bragg's equation conditions. The resulting diffraction peaks with different strengths and positions produce a characteristic pattern of the sample.

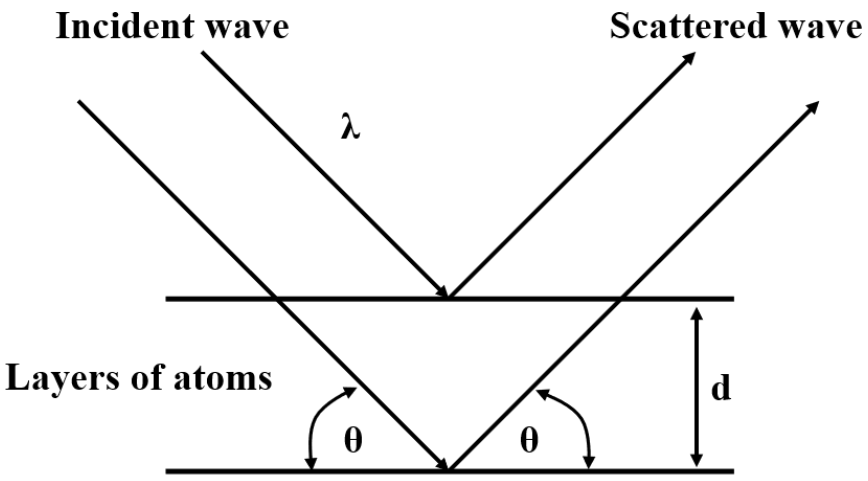

Figure 2.1 Bragg's Law diffraction.[218]

The lattice spacing that wide-angle X-ray diffraction can measure ranges from a few tenths to a few nanometers, which is the information of atomic arrangement. The materials that have a few to tens of nanometers structure require the small incident beam angle θ (~1-2°). In this range, the mesoporous structure can be clearly observed by small angle X-ray diffraction.

Scanning electron microscope.[219] When a beam of ultrathin high energy incident electrons strikes the surface of samples, the exciting area will produce secondary electron, Auger electrons, characteristic X-ray and backscattered electrons. The backscattered electrons are part of the incident electrons that are reflected by the solid sample atoms, they can be used as imaging signals for analyzing the morphology and perform the qualitative composition analysis. The secondary electrons, which come from the range of 5-10 nm away from the surface, are the extranuclear electrons bombarded by incident electrons. They are sensitive to the surface state of the sample

and used for effectively displaying the microscopic morphology. When the inner electron of atoms is excited, the process of energy level transition would release characteristic energy by X-ray, which is called characteristic X-ray. Otherwise, another electron outside the nucleus would be ejected and become a secondary electron called Auger electron. The Auger electronic signal is appropriate for determination of surface chemical composition. These signals mentioned above would be collected by the detector and transported to the kinescope; then the image is displayed by raster scan (**Figure 2.2**).

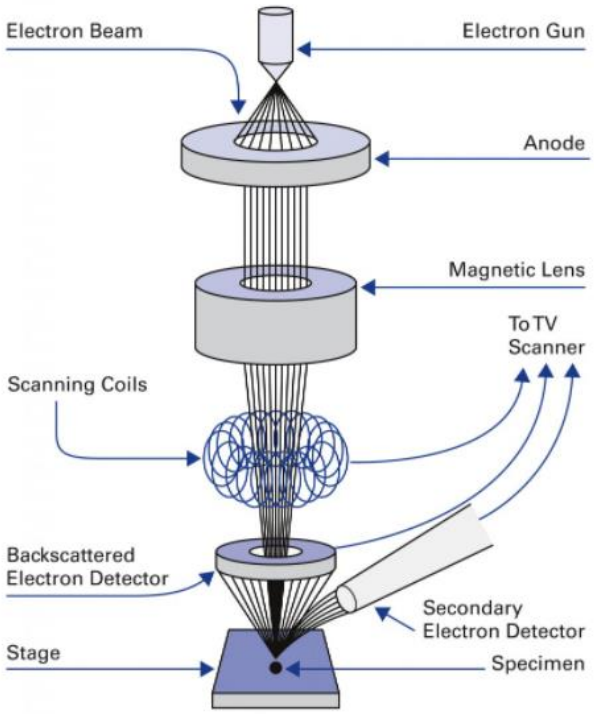

Figure 2.2 System of scanning electron microscopy.[220]

Transmission electron microscopy.[221] Similar to X-ray, electrons can also be utilized for diffraction. TEM uses electrons generated by an electron gun for diffraction studies.

According to the de Broglie equation λ = h/mv and the kinetic energy equation E = $mv^2/2$, the electron wavelength is:

$$\lambda = \frac{h}{\sqrt{2mE}}$$

When the electron beam has a high enough accelerating voltage of 120 kV, the crystal structure would be obtained. Here the wavelength λ is 0.0335 Å.

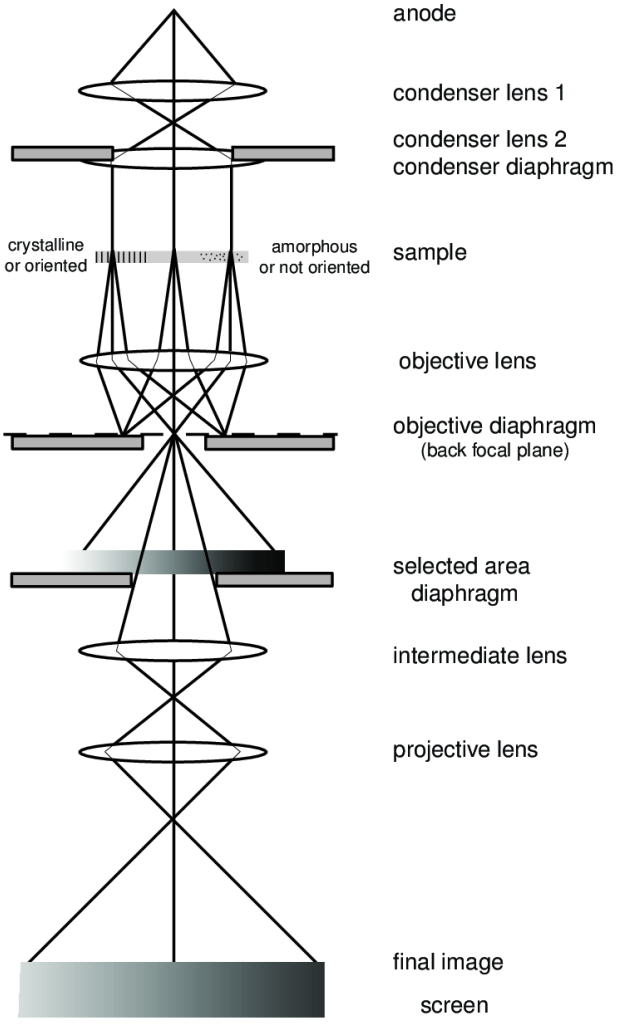

Figure 2.3 The system of transmission electron microscopy.[222]

Moreover, TEM is also utilized as microscopy that can achieve a higher resolution than a normal optical microscope due to the wavelength of the electron is much shorter than

that of the visible light. The electron beam can carry the structural information inside the sample. Because the amounts of electrons transmitted through the dense and sparse parts are different. The scattering angle of electrons is large at the thick positions of sample. Thus, fewer electrons can pass through these positions, which leads to the darker brightness of image.

Ultraviolet and visible spectrophotometry.[223] The UV-vis spectrophotometry is a method of measuring the absorbance of substances in the wavelength range of 190~800 nm, which is used for identification, impurity inspection and quantitative determination. When the monochromatic light radiation passes through the measured substance solution, the relationship among the physical quantities can be described by Lambert-Beer's Law as follows:

$$A = lg\frac{1}{T} = Ecl$$

where A is the absorbance, T is the light transmittance, E is an absorption coefficient (the absorbance value when the solution is 0.01 g/mL and the liquid layer thickness is 1 cm), c is the weight (g) of the substance contained in the 100 mL solution, l is the liquid layer thickness.

In the concern experiments, a series of test solutions have been prepared, their absorbances are tested at the specified wavelength, then the contents are calculated based on the absorption ratios.

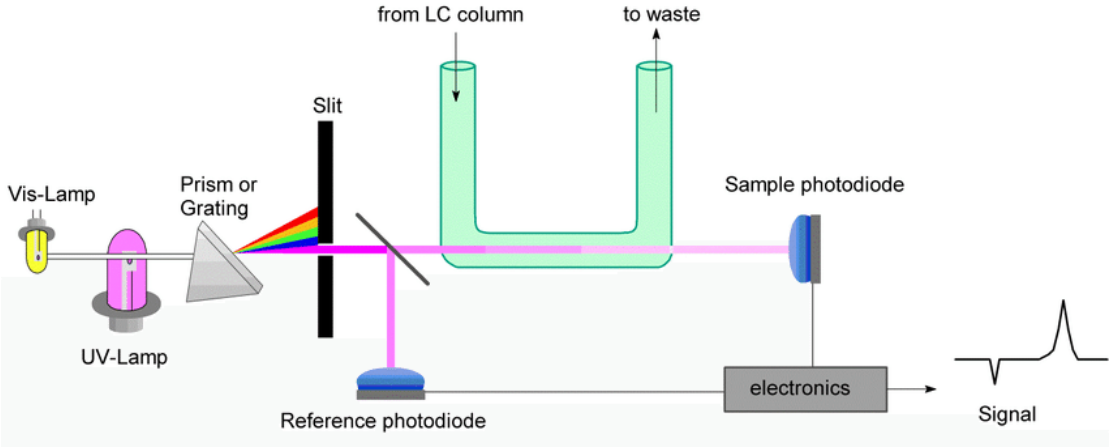

Figure 2.4 The principle of ultraviolet and visible spectrophotometry.[224]

X-ray photo-electron spectroscopy.[225] XPS can be used for qualitative analysis and semi-quantitative analysis. Generally, the information of element composition, chemical state and molecular structure on the surface can be obtained from the peak position and shape of the XPS spectrum. The element concentration can be obtained from the peak intensity.

When a beam of photon irradiates the surface of the sample, the photon can be absorbed by the electron in the atomic orbit of a certain element, so that this electron is released from the atom with a certain kinetic energy and become a free photoelectron (**Figure 2.5**). Meanwhile, the left atom would become an excited ion. According to the Einstein's Law of photoelectric emission:

$$Ek = h\nu - EB$$

where Ek is the kinetic energy of the emitted photoelectron, hν is the energy of X-ray source photon, EB is the binding energy on a specific atomic orbital.

It is obvious that for a specific monochromatic excitation source and a specific atomic orbital, the photoelectron energy is characteristic. Thus, it is possible to analyze the element types of substances based on the binding energy of photoelectrons. In addition, due to the different chemical environments of atoms, the inner shell electron binding energy would have a change, which is performed as the shift of the peak on the spectrum. Significantly, XPS is a typical surface analysis method because only the photoelectrons emitted from a thin layer near the surface of the sample can escape. The information depth (d) is decided by the electron escape depth (λ), which follows the equation of d = 3λ. Generally, the λ for metal is 0.5-3 nm, for inorganic non-metal material is 2-4 nm, for organic compound and polymer is 4-10 nm.

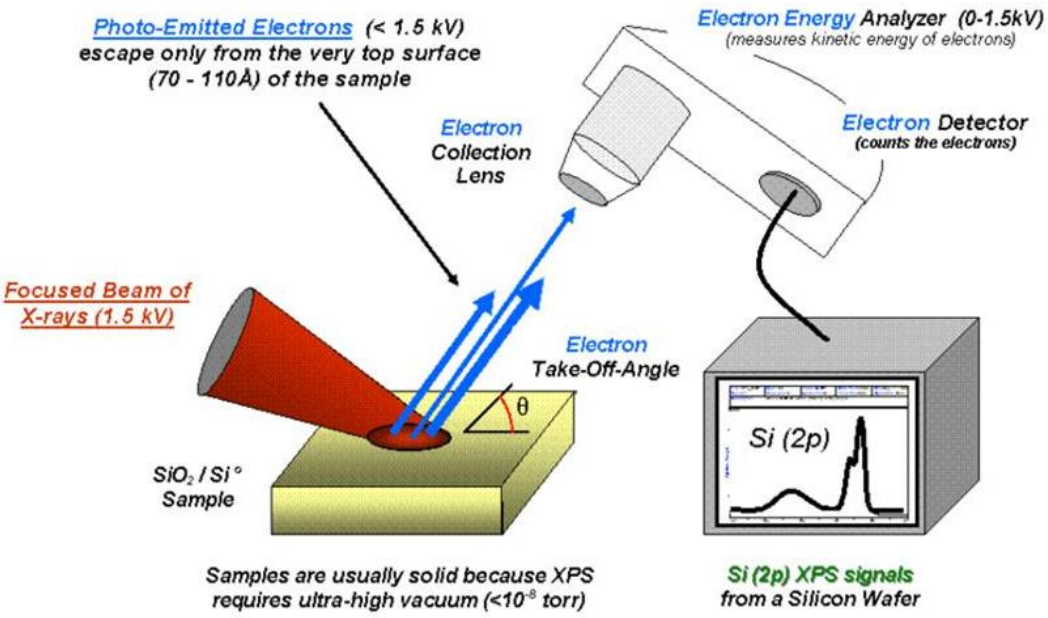

Figure 2.5 The principle of X-ray photo-electron spectroscopy.[226]

Brunauer-Emmett-Teller area method.[227] Brunauer, Emmett and Teller proposed the BET multi-molecular layer adsorption theory in 1938 and expressed the conclusion as BET equation. The basic assumptions of the model used in the derivation are: (1) the solid surface is uniform and multi-layer adsorption occurs; (2) the adsorption heat of each layer except the first layer is equal to the heat of liquefaction of the adsorbate.

Nitrogen and helium are used as the adsorbate and carrier gas. These two kinds of gases are mixed in a certain proportion to reach the specified relative pressure, then they flow through the solid sample. When the sample tube is put into liquid nitrogen, the sample starts to physically adsorb the nitrogen in mixed gas, which shows the adsorption peak. After the liquid nitrogen is removed, the adsorbed nitrogen is desorbed, which shows the desorption peak. Finally, a known volume of pure nitrogen is injected into the mixed gas to obtain a correction peak. According to the peak areas of the correction and the desorption peak, the adsorption capacity of the sample under the relative pressure can be calculated. By changing the mixing ratio of nitrogen and carrier gas, several adsorption capacities under different relative pressures of nitrogen can be measured. The specific surface area can be calculated according to the BET equation.

2.3 Photocatalytic and piezoelectric catalytic activity measurements

2.3.1 Photocatalytic H_2 evolution measurements

Photocatalytic H_2 evolution activities were carried out in a Pyrex top-irradiation vessel connected to a glass closed gas circulation system. The temperature of the reactant

solution was maintained at 5°C through the flow of cooling water during the reaction. A 300 W Xenon lamp (PLS-SXE300C, Perfectlight) was used as the visible light source. The irradiation area was 18.1 cm^2 and the incident light power density was 304 mW cm^{-2}. Typically, 5 mg of the catalyst and 80 mg of EY were dispersed in 80 mL of a 10% (v/v) triethanolamine-water (TEOA-H_2O) solution by ultrasonication for 15 mins.

The cyclic stability of the catalyst was tested as follows and the initial reaction amount of EY was 20 mg. After the first run, under visible light irradiation, the photocatalytic system was thoroughly degassed. Then 20 mg of fresh EY, 2 mL of TEOA and 15 mL deionized water were added without any other treatments like centrifugation and washing. Subsequently, the thoroughly degassed system was irradiated again using a 300 W Xe lamp. For simplification treatment and comparison, unless specifically mentioned, the photocatalytic activity of hydrogen evolution was carried out at pH = 11. The pH values of the reaction solution were adjusted by the addition of hydrochloric acid (HCl) or sodium hydroxide (NaOH). This measurement was processed by an online gas chromatograph with a thermal conductivity detector (Scion GC-9790, Ar as carrier gas).

2.3.2 Piezoelectric H_2 evolution measurements

The piezo-catalytic reaction was performed in a hermetic Ar atmosphere under room temperature. The ultrasound resource was from a Kunshan Jielimei ultrasound cleaner (KS-100DE, 120 W). The output power was set as 100% as the default value and the

frequency was 40 kHz. Then 5 mg of catalyst was added in 10 mL deionized water in a Pyrex reaction cell. In order to degas the air in the system, the solution was purged by argon for 10 min before the reaction. By default, the reaction was continued for 1 h for H_2 evolution. The mixed gas containing H_2 production in the reaction cell was extracted by a 100 mL injector for measurement. This measurement was processed by an online gas chromatograph with a thermal conductivity detector (Scion GC-7900, Ar as carrier gas).

2.4 Electrochemical measurements

2.4.1 Electrochemical characterization

The electrochemical tests were conducted on an electrochemical workstation (CHI760E, CH instrument) with a conventional three-electrode cell. A Pt plate (1 cm × 1 cm) was employed as the counter electrode and an Ag/AgCl (saturated KCl) electrode was used as the reference electrode. The working electrode was prepared on a rotating ring-disk GCE with a diameter of 5 mm. The exposed area of the working electrode was 0.19625 cm^2. The GCE was polished with α-Al_2O_3 powder with decreasing sizes (1.0 - 0.05 μm), and it was then ultrasonically washed with deionized water and absolute ethanol before the samples were coated on it.

The electrode materials in **chapter 4** were prepared by dispersing 5 mg of the catalyst and 1 mL mixed solution, which was compounded by 25 μL of Nafion solution, 250 μL of ethanol and 750 μL of water. The mixture was then sonicated for about 1 h at room

temperature to form a homogeneous ink. 10 μL of the ink (containing 0.05 mg of catalyst) was loaded onto the GCE, giving a loading mass of 0.25 mg cm^{-2}. The same procedure was used for all of the samples during their electrode preparation. The EIS and CV measurements were respectively performed in the Fe ions solution ($K_4[Fe(CN)_6]$ and $K_3[Fe(CN)_6]$ with mole ratio of 3:2) by applying an AC voltage with -1.5 mV amplitude in a frequency range from 100 kHz to 1 Hz. The bias sweep range was from -0.4 V to 0.8 V; the scanning rate of 0.1 V/s. The polarization curve was performed in the 0.2 M aqueous Na_2SO_4 solution with the bias sweep range from -1.6 to 0 V *vs.* Ag/AgCl. The specific capacitance was calculated according to the formula of $C = \frac{\int IdV}{V\Delta E}$, where *C (F)* is the total capacitance, $\int IdV$ is the areas of close curves, ΔE is the electrochemical window, *v* is the scanning rate.

The experimental method of **chapter 5** had shown here. The 2.5 mg samples were dispersed into 500 μL N, N-dimethylformamide solution with 0.15% Nafion solution. After ultrasonication for 30 min (*i.e.* to form a paste-like suspension), the slurry was obtained. Then, 10 μL of the slurry was spread onto the rotating ring-disk electrode, giving a loading mass of 0.25 mg cm^{-2}. The working electrode was further dried at 60°C for 10 min to improve adhesion. The same procedure was used for all of the samples during their electrode preparation. The EIS and CV measurements were respectively performed in 0.2 M aqueous Na_2SO_4 solution by applying an AC voltage with -1.5 mV amplitude in a frequency range from 100 kHz to 0.01 Hz. The bias sweep range was from -1.6 V to 0.6 V; the scanning rate of 0.1 V/s. The polarization curve was performed

in the same above-mentioned three-electrode system, while the bias sweep range was from -1.5 to -0.5 V *vs.* Ag/AgCl with the electrolyte of 0.2 M aqueous Na_2SO_4 solution. The specific capacitance was calculated according to the formula of $C = \frac{\int IdV}{V\Delta E}$, where *C (F)* is the total capacitance, $\int IdV$ is the areas of close curves, ΔE is the electrochemical window, *v* is the scanning rate.

2.4.2 Electrochemical characterization principles

Cyclic voltammetry.[228] CV is generally a method of applying a voltage with a constant scanning speed to the electrode and continuously observing the relationship between the electrode surface current and the electric potential. It can be used to characterize the reaction on the electrode surface and to explore the mechanism of the electrode reaction. CV is usually utilized in the measurement of solution systems and used to characterize the properties of electrode modification materials and soluble molecules. CV can be qualitatively analyzed as follows. It is done by evaluating: (1) reversibility of electrode reaction, (2) reaction steps and mechanism, and (3) performance of electrode materials.

The input signal of CV is a cyclic triangular wave, the obtained current voltage curve includes two branches. When the first half of the potential is scanned to the cathode, the electroactive substance will be reduced on the electrode and produce a reduction wave. Then the second half of the potential is scanned to the anode, the reduction product will be oxidized on the electrode again and produce an oxidation wave. After a

triangular wave scanning, the electrode completes a cycle of reduction and oxidation process.

The peak height and symmetries of the oxidation and reduction waves in the cathode and anode directions can indicate the reversibility of the reaction of electroactive substances on the electrode surface. If the reaction is reversible, the curve is symmetric; vice versa. In general, with the increase of the sweep speed, the distance between two tops of peaks also increases (**Figure 2.6**). The reverse reaction of irreversible reaction is very slow so that the current peak in the back sweep usually vanishes.

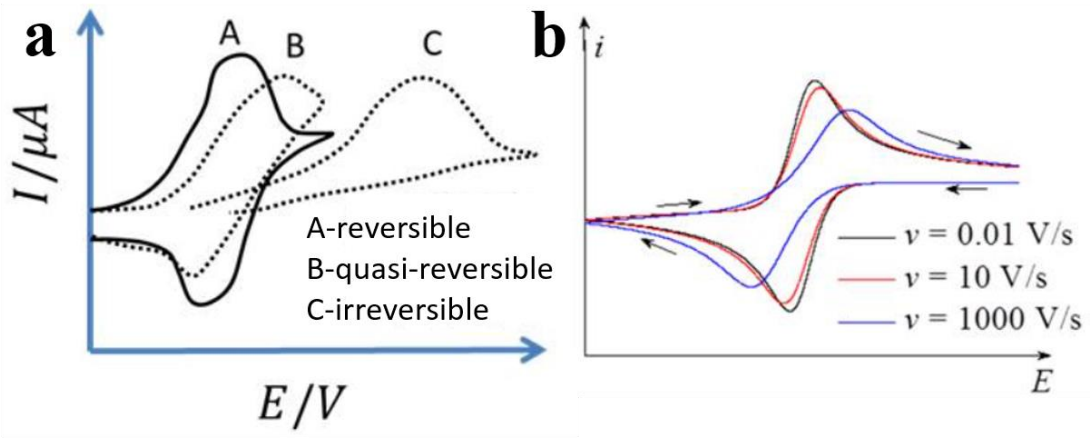

Figure 2.6 (a) Typical examples of CV curves. (b) CV curves under conditions of different sweep speeds.[229]

Electrochemical impedance spectroscopy.[228] EIS is also called AC impedance. When the electrochemical system is regarded as an equivalent circuit, EIS is defined as a kind of electrochemical measurement method using a small amplitude sine wave

current as input disturbance signal. The output is a sine wave potential signal and the transmission function is called impedance. The three basic conditions of EIS are causality, linearity and stability.

The impedance Z is a vector that varies with the frequency, which is usually expressed by the complex function of angular frequency ω:

$$Z = Z' + jZ''$$

where the j is the imaginary unit, Z' is the real part and the Z'' is the imaginary part. The norm and the phase angle Φ are calculated as follow:

$$|Z|^2 = Z'^2 + Z''^2$$

$$\tan\phi = \frac{-Z''}{Z'}$$

Under different frequencies, these results are expressed as various EIS curves (Nyquist and Bode images).

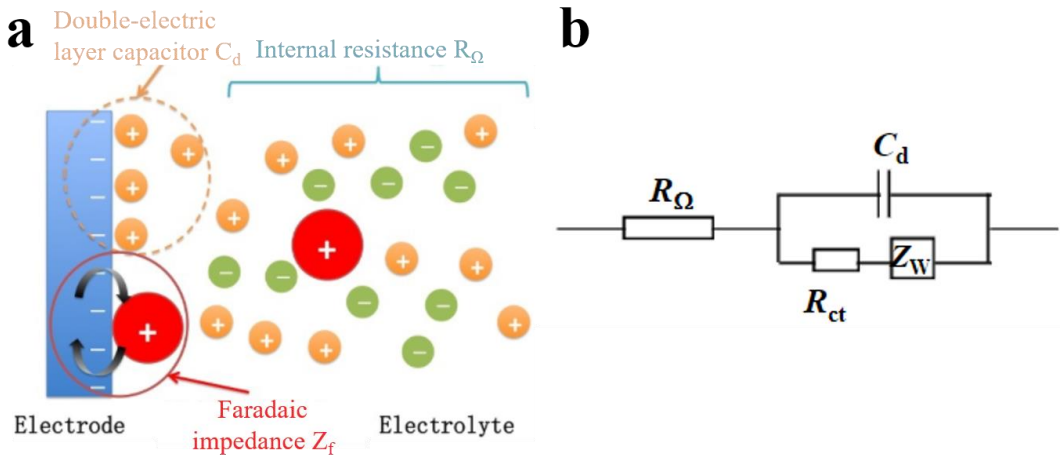

Figure 2.7 (a) The simulated electrochemical environment. (b) The equivalent circuit.[230]

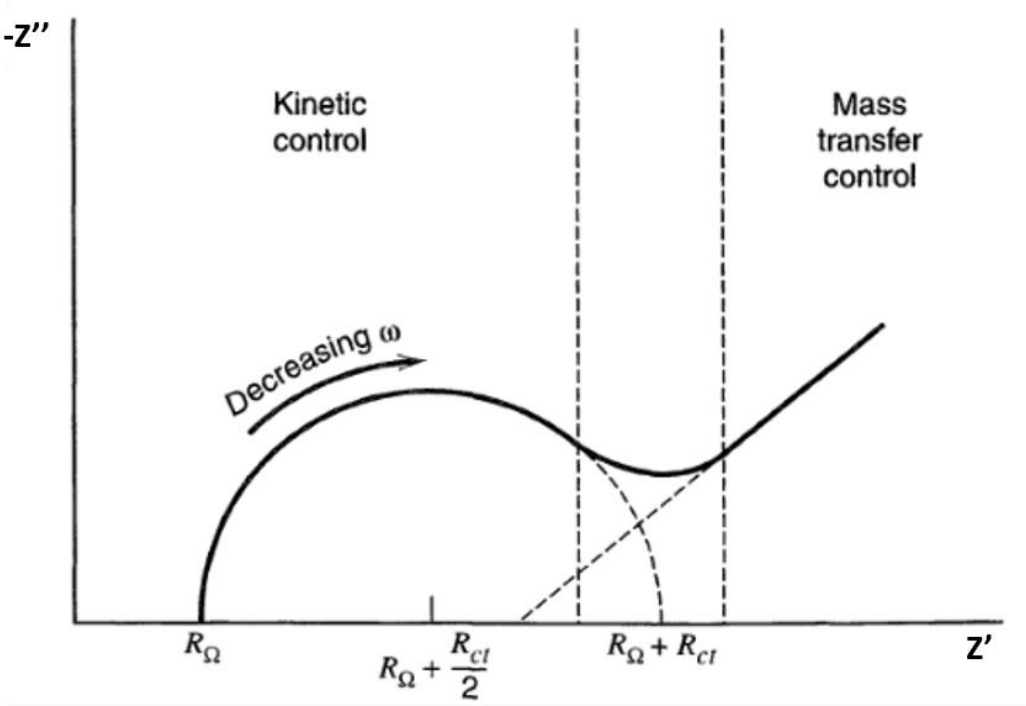

Figure 2.8 The typical EIS Nyquist image.[230]

The impedance Z of the equivalent circuit in **Figure 2.7** is:

$$Z = R_\Omega + \frac{1}{j\omega C_d + \frac{1}{R_{ct} + \sigma\omega^{-\frac{1}{2}}(1-j)}}$$

where the R_Ω is the internal resistance including the resistance of the solution and the measuring circuit; the C_d is the surficial double-electric layer capacitance; the R_{ct} is the charge transfer resistance during the electrochemical reaction; the Z_w is the impedance caused by diffusion process; the σ is a coefficient related to the transfer of matter. The typical EIS image result is shown in **Figure 2.8**. The ω decreases from the left side of the semicircle (∞) to the right side (0). Here, the ω in the midpoint of the semicircle and the Z' at the intersection of the slope line and the x-axis are:

$$\omega = \frac{1}{R_{ct}C_d}$$

$$Z' = R_\Omega + R_{ct} - 2\sigma^2 C_d$$

The transfer control is expressed as a straight line with a slope equal to 1.

Linear Sweep Voltammetry.[229] LSV usually applies three electrode systems composed of a working electrode, counter electrode and reference electrode for analysis. The working electrode and the reference electrode form a potential loop to control the input potential signal, meanwhile the working electrode and the counter electrode form a current loop to collect the output current signal. Then the qualitative and quantitative analysis of the material is performed.

In LSV testing system, the polarization mainly occurs on the working electrode, so the charge and material transfer process at the working electrode - solution interface has become the speed control step of the whole current loop, which determines the change of current and the shape characteristics of the diagram. The Faraday current produced on the working electrode generally consists of three parts: (1) the transfer or transport of electrons on the electrode conductor; (2) the heterogeneous electron transfer process; (3) the matter transfer from the liquid phase mass to an electrode - solution interface.

By changing the potential of the working electrode, the highest energy level (Fermi level) occupied by electrons on the electrode has changed. The negative or positive shift of electrode potential leads to the rise or fall of Fermi level, respectively. In the

electrode reduction or oxidation process, the applied electrode voltage should be enough to make the electrode potential higher than the LUMO energy level or lower than the HOMO energy level; then the electrons would transfer from the electrode to the solution and promote the reaction. The difference between Fermi level and LUMO or HOMO is larger, the activation energy is higher and the electron transfer is faster.

2.5 Computational methodology

The electronic characteristic calculations in **chapter 4** were conducted based on DFT implemented in the quantum Espresso Package on a plane wave basis.[231] The experimental data were used as the initial structure and the optimization was performed using Broyden, Fletcher, Goldfarb, and Shannon (BFGS) algorithm until the residual forces were less than 10^{-4} eV.[232] In wave vector k space, plane wave cut-off energy was set to 45 Ry and a 6×6×6 Monkhorst-Pack k-point mesh was used to sample the Brillouin zone of slabs.

All density functional theory (DFT) calculations in **chapter 5** were performed in Quantum Espresso Package.[231] The projector augmented wave (PAW) pseudo-potentials were for considering the interaction of ions and core electrons. The valence electronic configurations were 2s 2p for N and 3d 4s for Fe, 3s 3p 4s 3d for Co, V, Cr, while 5d 6s of W was treated as the valence electrons. We had used the generalized gradient approximation (GGA) of Perdew, Burke and Ernzerhof (PBE) to calculate the exchange and correlation terms.[233] Broyden, Fletcher, Goldfarb, and Shannon (BFGS)

algorithm was adopted for the variable cell optimizations.[232] The (001) surface of Fe_2N was built via the slab model. One of the top Fe atoms had replaced with the dopant atom on the Fe_2N surface. A vacuum region of 15 Å was considered above the doped surfaces to prevent interactions between surfaces and periodic images. The same number of atoms consists of 2×2×4 unit cells in 8 layers had been used for all the slabs. The experimental result was used as a starting point and then the crystal structure was fully relaxed until the residual forces on each atom were less than 10^{-4} eV/Å; the tolerances for geometry optimization were within 10^{-6} eV/atom. In wave vector k space, plane wave cut-off energy was set to 55 Ry and a 6×6×1 Monkhorst-Pack k-point mesh was used to sample the Brillouin zone of slabs. In addition, the d-band center model is also considered an outstanding descriptor for hydrogen catalytic reactions.[234,235]

2.6 TON and TOF calculation

For the photocatalytic water splitting, the TON was measured when the photocatalytic reaction reached the material surface, while the TOF was measured in forming time during the reaction.

$$\mathrm{TON} = \frac{the\ molar\ amount\ of\ gas\ production}{the\ molar\ amount\ of\ surface\ atoms\ of\ catalyst}$$

$$\mathrm{TOF} = \frac{the\ molar\ amount\ of\ gas\ production}{the\ molar\ amount\ of\ surface\ atoms\ of\ catalyst\ \times reaction\ time\ (s)}$$

Chapter 3

Ordered Mesoporous Transition Metal Nitrides Prepared through Hard Template Nanocasting and Rapid-Nitridation Process

3.1 Introduction

Although there are various of synthesis methods for producing TMNs, it is not equally easy to make various porous nitride materials. That is, certain porous nitrides lend themselves to high-temperature synthesis rather readily, while others do not. For instance, CoN and CrN are synthesized readily using long nitridation processes; these materials do not show the collapse of the nanostructures even after long nitridation runs.[185] This is due to their low diffusion rate coefficient and surface oxide layers that stabilize the material.[236,237] Therefore, there is a need to synthesize nitrides of transition metals, including those whose constituent elements have high diffusion rates (*e.g.* W, Fe).[238] To achieve this, a rapid process that is also high yield would be important.

Most of TMNs can be synthesized by rapid-nitridation while keeping their expected patterns, especially including some metal nitrides that are extremely hard to approach pure phase and order structures. The rapid process of heating can aid in bypassing the collapse of structures and forming pure phases. Furthermore, ensuring rapid phase formation helps avoid aggregation, grain growth, and coalescence. Especially, the method of rapid-nitridation has not been researched in the previous paper according to the introduction in **chapter 1**, so it could become a promising synthesis field in the future. Hence it is evidently valuable to develop methods for the rapid synthesis of nitrides.

Herein, we report a novel hard template/rapid-nitridation synthesis of ordered mesoporous metal nitrides, which is based on a nanocasting-thermal nitridation process. This method uses 2D ordered hexagonal mesoporous SBA-15 as the hard template, which in turn offers the necessary stable scaffold for high-temperature crystallization and large specific surface area. A series of TMNs including CoN, WN, CrN, and Ni_3FeN with ordered and regular mesoporous structures have been successfully synthesized within 30 min using temperatures in the range ~330-800℃ from the corresponding mesoporous oxides. A comparative experiment shows that when long heating processes are employed, ordered mesopores are hard to maintain anymore. This proves the necessity and universality of this synthesis method of rapid-nitridation for keeping nanostructures of materials.

3.2 Results and discussion

3.2.1 Synthesis and XRD, BET characterizations of mesoporous TMNs

The preparation of mesoporous nitrides via a nanocasting-rapid thermal nitridation approach is performed using hexagonal mesoporous silica SBA-15 as a hard template. The BET specific surface area of the as-synthesized SBA-15 template is 733.8 m^2g^{-1}, with a pore volume of ~1.15 $cm^3\ g^{-1}$ and a pore diameter of ~6.8 nm (**Figure 3.1**).

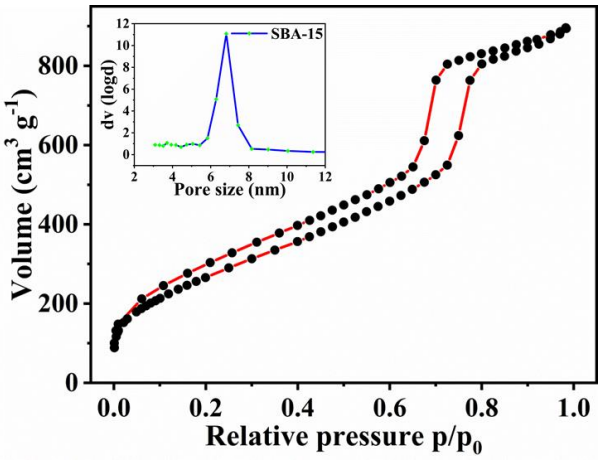

Figure 3.1 BET isotherm curve and pore size distribution of as-synthesized SBA-15 template.

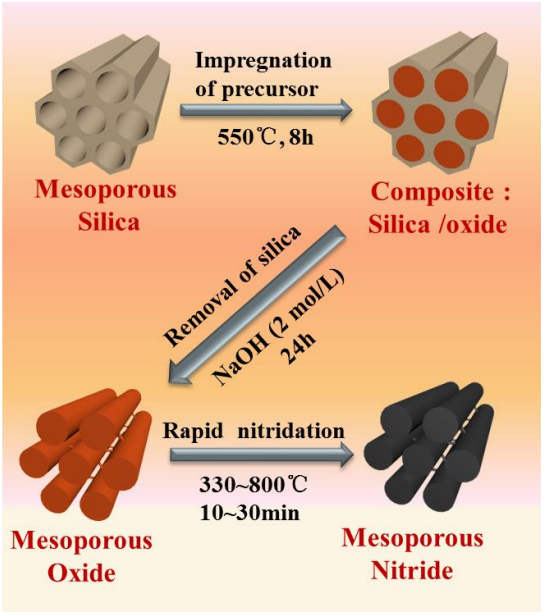

Figure 3.2 Schematic illustration of the synthesis strategy of mesoporous nitrides.

The synthesis procedure involves a cooperative templating mechanism. As is illustrated **(Figure 3.2)**, the process involves three steps: (i) impregnation of metal nitrates precursor, (ii) removal of silica hard template, and (iii) subsequent rapid-nitridation. Firstly, the hexagonal SBA-15 hard template is prepared under

hydrothermal and calcination conditions according to the previously established procedures.[185,215] Afterwards, several types of mesoporous metal oxides including Co_3O_4, WO_3, Cr_2O_3 and Ni_3FeO_x are synthesized through impregnation of their corresponding metal nitrates in mesoporous hard templates in ethanol solution.

After the evaporation/calcination process, a second reimpregnation and subsequent in situ conversion lead to metal oxides/SBA-15 composites, after calcination at 550°C. The silica template is then removed with a concentered hydroxide sodium solution (2 mol L^{-1}). Finally, the mesoporous TMNs are obtained through rapid-nitridation in a tube furnace from the corresponding oxides. The conditions of 330°C for 15 min, 600°C for 10 min and 800°C for 30 min were used to obtain CoN, WN and CrN, respectively. Likewise, 380°C is used for 30 min to obtain Ni_3FeN. It should be noted that all the reaction times are calculated based on the time wherein they enter the set temperature region, to the time wherein they quit the heating environment. Finally, these nitrides are stored in sample cells for further tests and measurements.

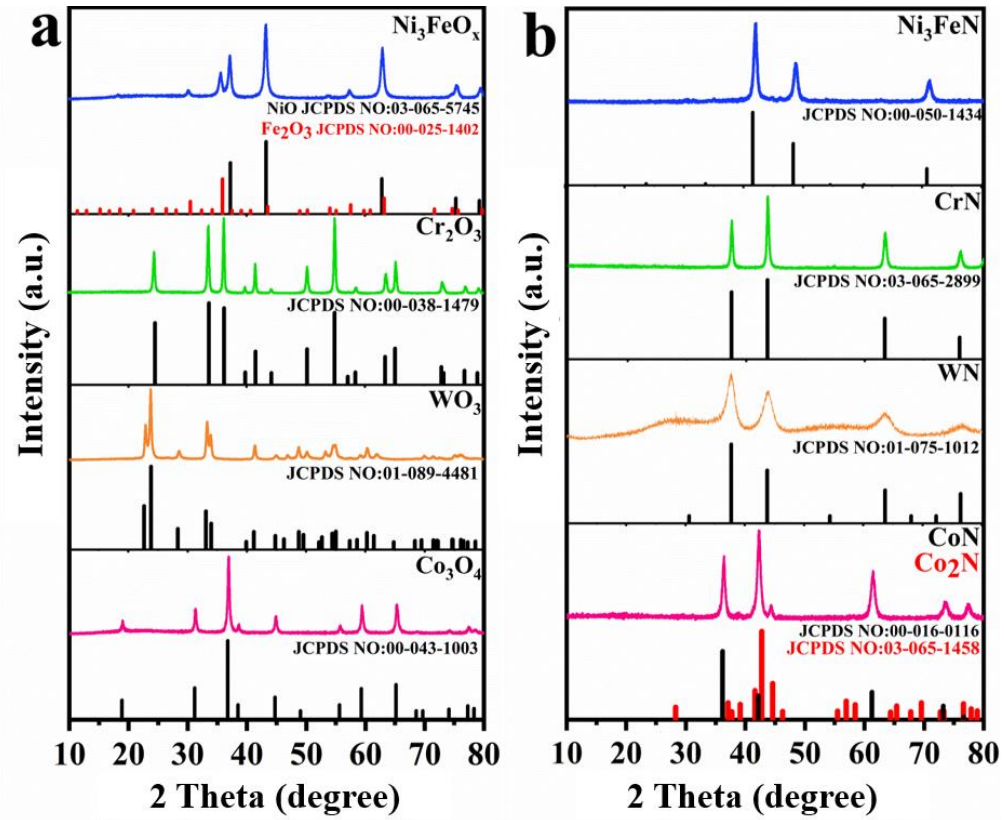

Figure 3.3 (a) Wide-angle XRD patterns of mesoporous transition metals oxides and (b) their corresponding mesoporous transition metals nitrides.

The structural properties of a series of mesoporous TMOs precursors and their derived TMNs have been studied using XRD and TEM analysis. The wide-angle XRD patterns of TMOs are displayed in **Figure 3.3a**. All of the monoxide samples show well-defined diffraction peaks corresponding to their standard cards. For instance, the samples of Co_3O_4, WO_3 and Cr_2O_3 are indexed as the crystal faces of the cubic phase (JCPDS card 00-043-1003), tetragonal phase (JCPDS 01-089-4481), and trigonal phase (JCPDS 00-038-1479), respectively. The XRD pattern of the mesoporous mixed-oxide Ni_3FeO_x shows characteristic diffraction peaks that could be well indexed to a mixture of NiO and Fe_2O_3 oxides.

The diffraction peaks appearing at 2θ = 30.27°, 35.69°, 37.31°, 43.34°, 57.40°, 63.01°, 74.54° and 79.55° are attributed to (206), (119), (226), (0012), (1115), (4012), (3315) and (4412) crystal planes of the cubic phase Fe_2O_3 (JCPDS card 00-025-1402), respectively. Among these main peaks, the diffraction peaks observed are at 37.26°, 43.29°, 62.88°, 75.42° and 79.41°. These correspond to (111), (200), (220), (311) and (222) crystal planes of the cubic phase NiO (JCPDS card 03-065-5745), respectively.

Figure 3.3b shows the XRD profiles of all the binary nitrides (CoN, WN and CrN). The peaks correspond to the expected cubic phases (JCPDS card 00-016-0116, 01-075-1012 and 03-065-2899). Ternary Ni_3FeN nitride has its main peaks at 41.53°, 48.34° and 70.82°, which is attributed to the (111), (200) and (220) lattice planes of the cubic phase Ni_3FeN phase (JCPDS card 00-050-1434). Typical Rietveld refined XRD patterns of mesoporous nitrides show that CoN, WN and CrN crystallize in the NaCl-type cubic phase (**Figure 3.4**). The Ni_3FeN sample shows a reverse perovskite phase. Notably, the CoN sample includes two phases, which is confirmed by the presence of peaks at 42.66° and 44.49° indexing to the (111) and (210) planes can be assigned to CoN in Pnnm (58) space group, while there is a very slight peak at 44.49°; this can be indexed to the (210) lattice plane of Co_2N accompanied by the increase of the intensity of the peak at 42.66° (JCPDS card 03-065-1458). This phase may be produced by over-reduction.

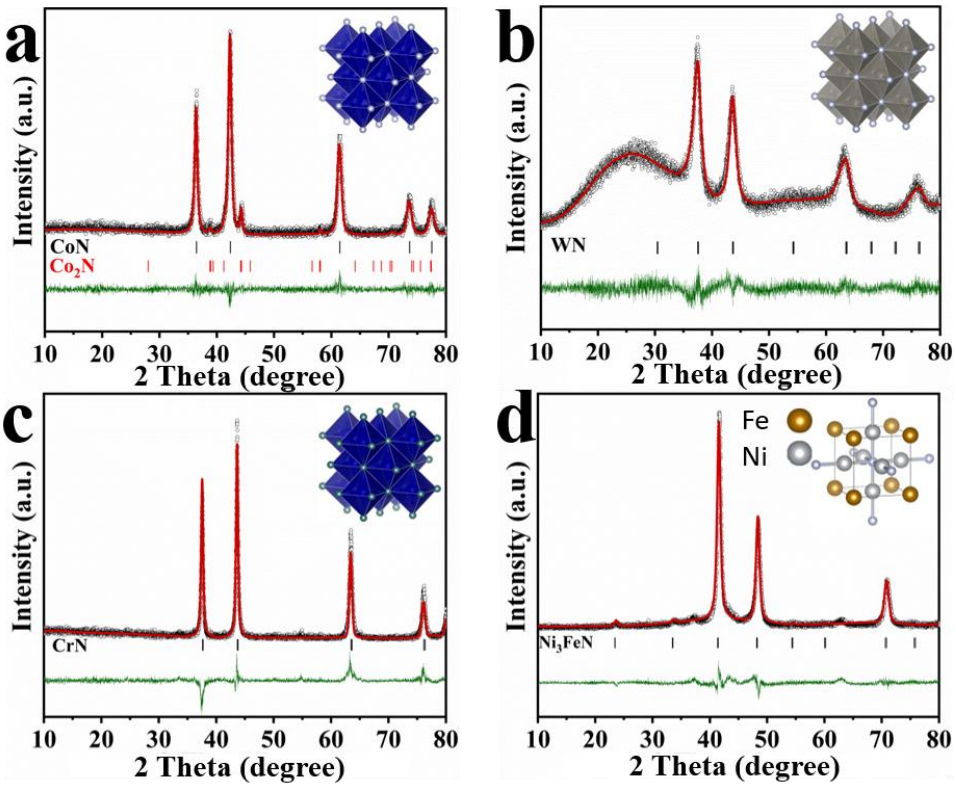

Figure 3.4 Rietveld refined XRD pattern of the samples (inset show their simulated crystal structure); (a) CoN (Co_2N), (b) WN, (c) CrN and (d) Ni_3FeN.

To investigate the regularity of mesopores, materials are examined using low-angle XRD. **Figure 3.5** displays low-angle XRD patterns of the mesoporous silica SBA-15, intermediate replica mesoporous oxides and corresponding metal nitrides. The diffractograms of the hard template SBA-15 exhibits obvious diffraction centered at $2\theta = 0.93°$, and two low-intensity peaks at about $2\theta = 1.86°$ indexed to (100), (110) and (200), respectively. This indicates the hexagonal crystal structure of SBA-15.[239,240] After the nanocasting process, compared with the template SBA-15, all of the diffractograms of mesoporous oxides and their corresponding nitrides show a diffraction peak assigned to (100) reflection,

indicating the presence of a well-ordered mesostructure. The wide-angle powder XRD patterns of mesoporous SBA-15 (**Figure 3.6a**) shows a very broad single peak at about 23° in 2θ with a Cu-K_α source, which is a characteristic of the amorphous silica to the pristine.[241] This peak disappears for all of the mesoporous oxides confirming the removal of the template.

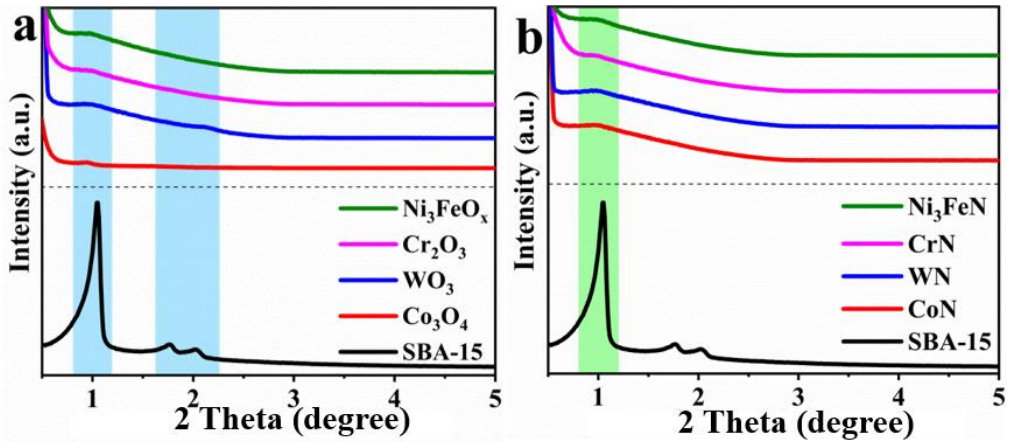

Figure 3.5 (a) Low-angle XRD patterns of SBA-15, Co_3O_4, WO_3, Cr_2O_3 and Ni_3FeO_x, as well as those of (b) SBA-15, CoN, WN, CrN and Ni_3FeN.

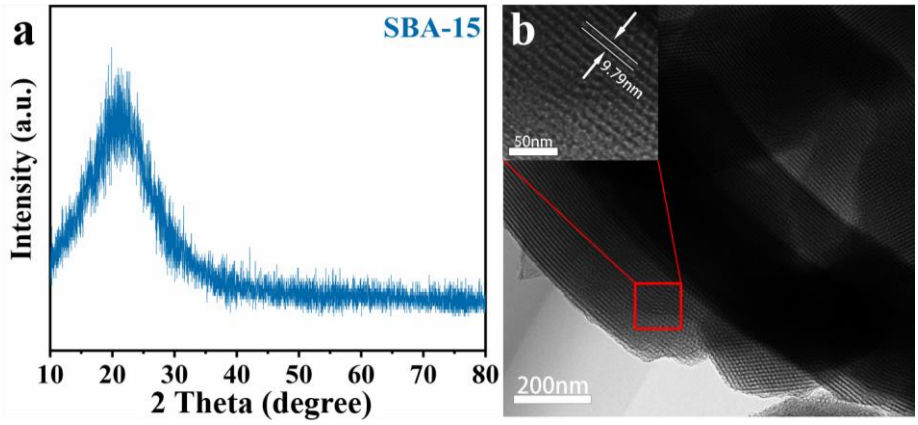

Figure 3.6 (a) Wide-angle powder XRD patterns of mesoporous SBA-15. (b) TEM images of mesoporous hard template SBA-15.

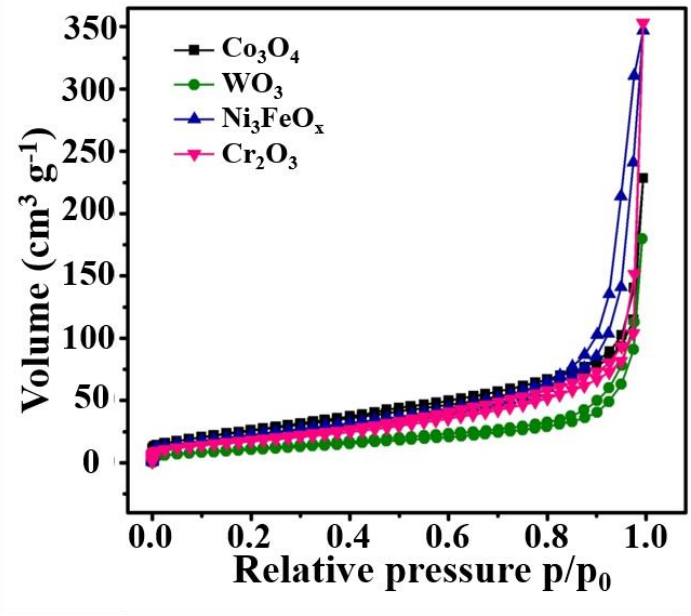

Figure 3.7 BET isotherm curve of mesoporous Co_3O_4, WO_3, Cr_2O_3 and Ni_3FeO_x.

To further confirm the mesoporous nature of as-synthesized materials, the N_2 adsorption-desorption isotherms of samples are measured and displayed (**Figure 3.7**). The nanocasting mesoporous oxides show a type IV isotherm with a clear hysteresis loop between $p/p_0 = 0.75$ and $p/p_0 = 0.9$, which is characteristic for mesoporous materials. The multiple-point BET surface area is 99.92, 83.75, 67.22, 43.15 m^2g^{-1} for Co_3O_4, Ni_3FeO_x, Cr_2O_3 and WO_3. The pore-size distribution determined by the BJH method indicates the mesopore-size distribution with wide distribution at the range of 5-7 nm. According to the result of previous research of a similar synthesis method (hard-template approach), the template-free mesostructured Ni_3FeN has BET surface area of 52 m^2g^{-1} with pore size distributions ranging around 5-8 nm.[165] Thus, the surface area of Ni_3FeN is decreasing due to the slight collapse of the sample in nitridation. The pore size

range is still similar, which means the mesostructures are maintenance.

3.2.2 Morphology and XPS characterizations of mesoporous TMNs

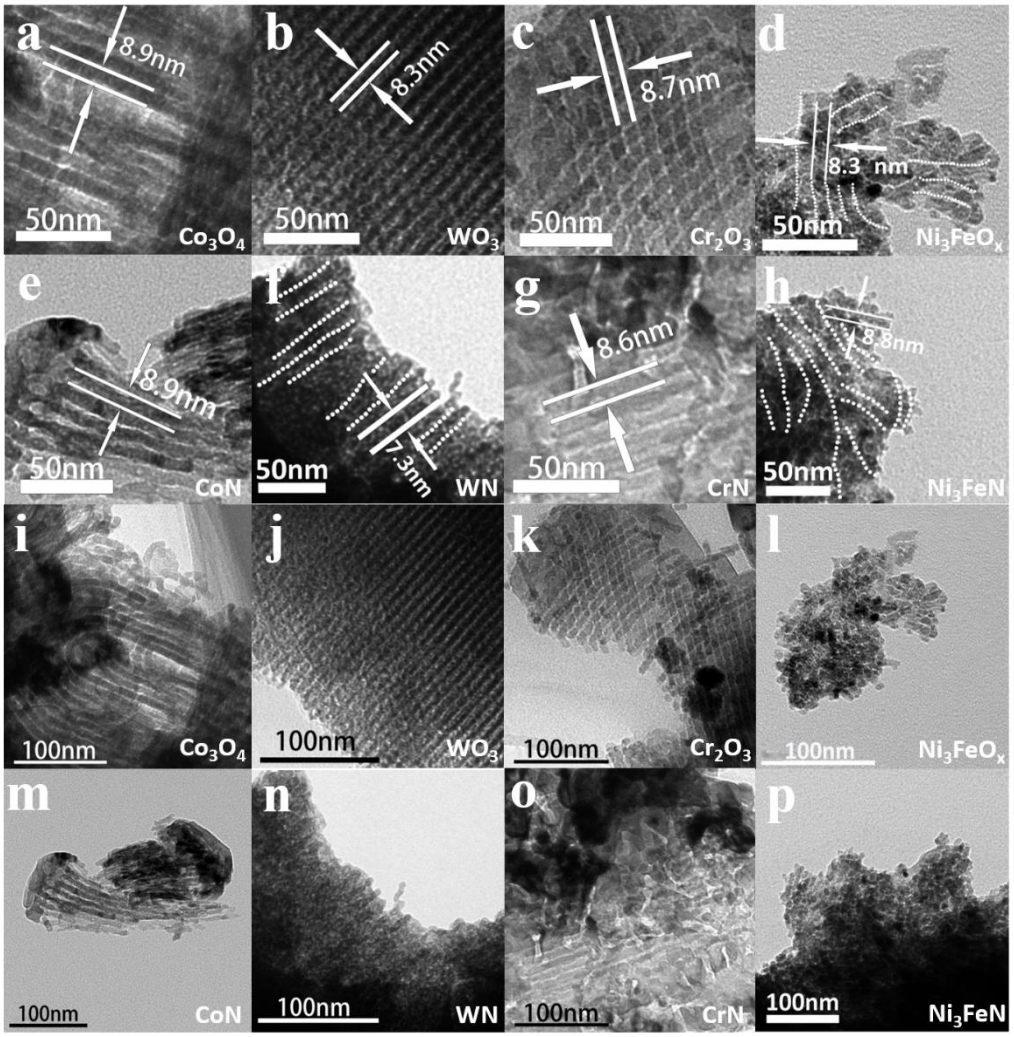

Figure 3.8 The high- and low-magnification TEM images of (a, i) Co_3O_4, (b, j) WO_3, (c, k) Cr_2O_3, (d, l) Ni_3FeO_x and (e, m) CoN, (f, n) WN, (g, o) CrN, (h, p) Ni_3FeN.

The texture of the mesoporous materials is investigated using TEM. The high-magnification images of the synthesized mesoporous TMOs and TMNs have been shown. As illustrated in **Figure 3.8a-d**, all four types of TMOs reveal a

highly ordered mesoporous structure with uniform distribution of nanoparticles in agreement with low-angle XRD. This ordered mesoporous structure derived from their SBA-15 template has been shown in **Figure 3.6b** highly ordered mesoporous structure with a two-dimensional straight-channel. The wall thickness of mesoporous oxides Co_3O_4, WO_3, Cr_2O_3 and Ni_3FeO_x is found to be about 8.9 nm, 8.3 nm, 8.7 nm and 8.3 nm, respectively. This is consistent with the known diameter of SBA-15 suggesting that the metal nitrates are indeed confined and grow into the hexagonal SBA-15 channels.[114,239,240]

As the results have shown, after the fast nitridation process the TEM of mesoporous nitrides CoN, WN, CrN and Ni_3FeN remain a similar nanoarchitecture with a wall thickness of 8.9 nm, 7.3 nm, 8.6 nm and 8.8 nm, respectively (**Figure 3.8e-h).** Evidently, the nitridation process does not affect the mesoporous nature of nitride materials. These results are further supported by the low-magnification TEM images of TMOs and TMNs (**Figure 3.8i-p)**. The morphology observed is very close to that of the parent template demonstrating the retention of the mesoporous structure during the reduction and oxidation.[242] The TEM images indicate that the composition does not have much effect on the final morphology of the as-prepared nitrides. The nitrides in fact achieve similar porosity to their mother oxides after rapid-nitridation. This is in line with previously reported works after solid/solid transformations.[243–245] The uniform spherical mesopores are consistent with low-angle XRD and transmission

electron microscopy (TEM), which reveal that the mesostructures can be well maintained.

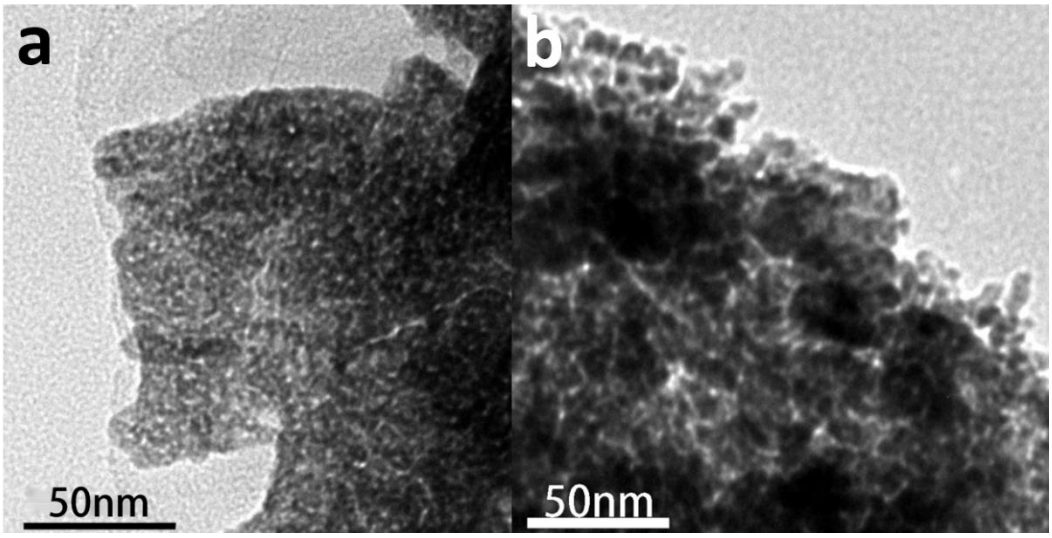

Figure 3.9 TEM images of (a) WN and (b) Ni_3FeN after long-time reaction (60 min).

To investigate the effect of time nitridation, **Figure 3.9** displays TEM of WN and Ni_3FeN synthesized in the same condition but at relatively long thermal nitridation durations (60 min). Compared to previous samples, these samples exhibit irregular and collapsed mesoporous structures due to prolonged heating time. This is because the metal with high diffusion rates can react with NH_3 and increase the disorder under a long reaction duration, which makes the crystal structure accomplish the process of collapsing. This comparative study evidently proves that the synthesis of WN and Ni_3FeN with rapid-nitridation time keeps the intact mesoporous structure, allows for interconnected pores and prevents the closure and collapse of pores.

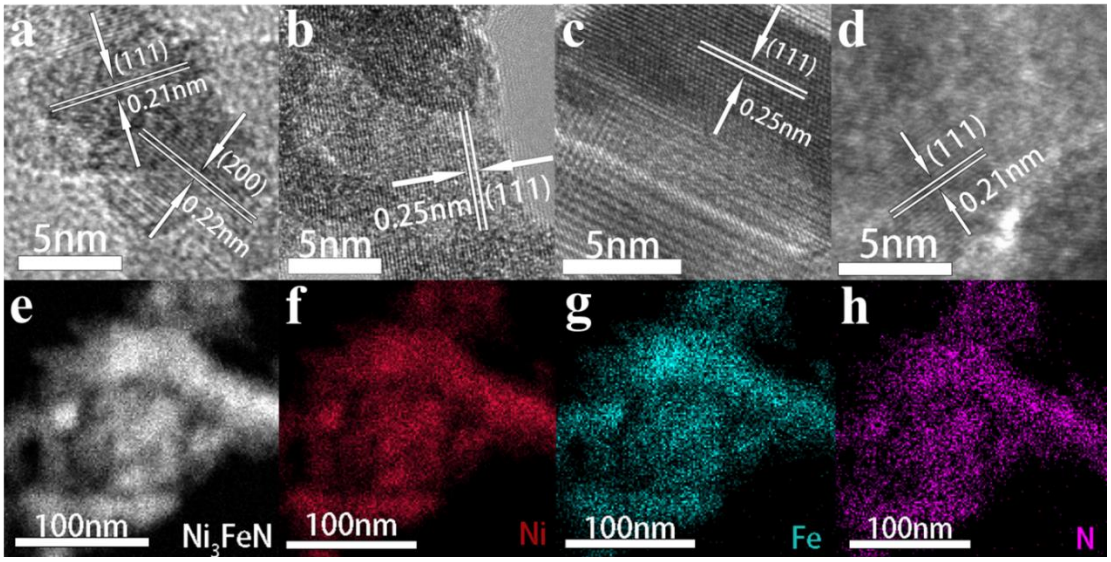

Figure 3.10 HRTEM images and their SAED pattern (inset) of (a) CoN, (b) WN, (c) CrN and (d) Ni_3FeN. Elemental mapping of images of Ni_3FeN nanoparticles. (e) EDS line scanning profiles of (f) Ni, (g) Fe and N (h).

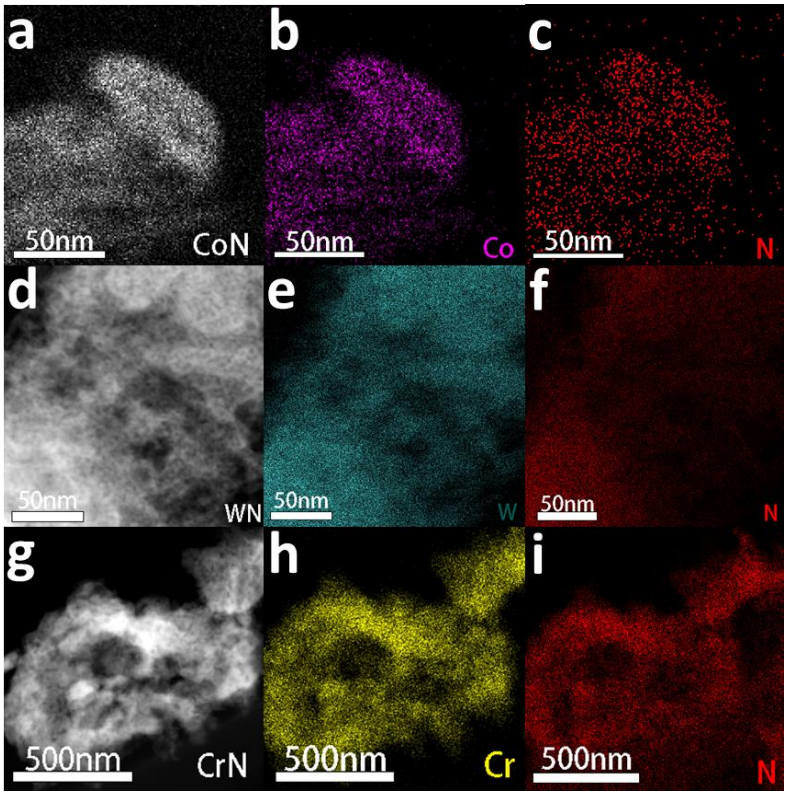

Figure 3.11 Elemental mapping of ordered mesoporous CoN (a-c), WN (d-f),

and CrN (g-i).

To further investigate the lattice structures and distribution of elements in mesoporous TMNs, the results of the HRTEM and the elemental mapping images of Ni_3FeN sample are shown. It can be seen from the HRTEM image (**Figure 3.10a**) that there are two clearly distinct lattice fringes with an interplanar distance of about 0.22 and 0.21 nm corresponding to the (200) crystalline plane in CoN phase and (111) crystalline plane of Co_2N phase. This is in agreement with the XRD results. For the other mesoporous nitride samples, **Figure 3.10b-d** shows distinct lattice fringes associated with WN, CrN and Ni_3FeN; these indicate interplanar distances of 0.25 nm, 0.25 nm and 0.21 nm, respectively. Additionally, all of them coincide with their (111) crystalline in the cubic phase. This indicates that the crystal structures of all mesoporous patterns are rather uniformly orientated. The elemental mapping images of mesoporous ternary nitride Ni_3FeN (**Figure 3.10e-h**) confirm the homogeneous distribution of Ni, Fe, and N elements. Furthermore, we can observe a uniform distribution for each element in all of the binary nitrides (**Figure 3.11)**.

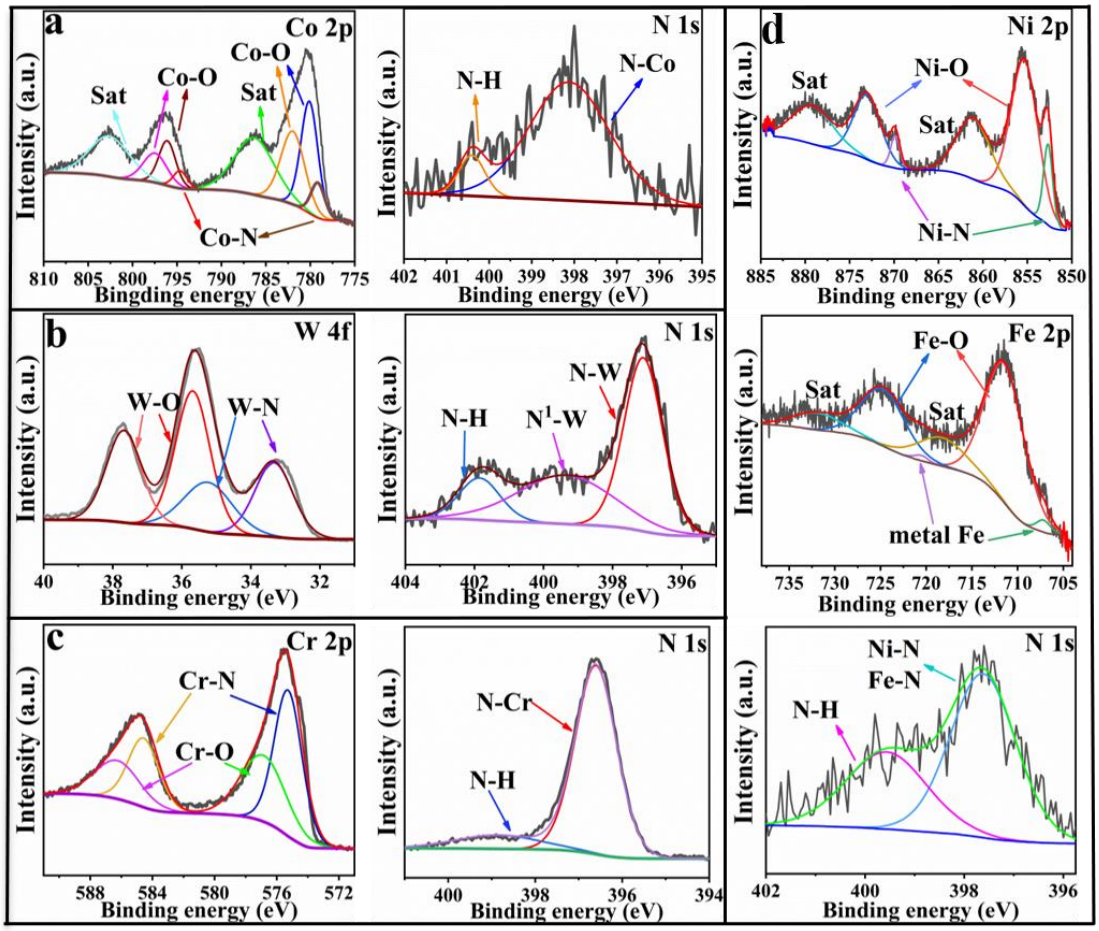

Figure 3.12 High-resolution XPS spectra for (a) Co 2p and N 1s of CoN, (b) W 4f and N 1s of WN, (c) Cr 2p and N 1s of CrN and (d) Ni 2p, Fe 2p and N 1s of Ni_3FeN.

Meanwhile, XPS is employed to further investigate the chemical states of as-synthesized mesoporous TMN. **Figure 3.12a** displays the XPS high-resolution Co2p and N1s in the CoN sample. The Co2p spectra are fit for two binding energy $Co2p_{1/2}$ and $Co2p_{3/2}$ and each one is divided into four components. The main peaks that exist at 779.2 eV can be assigned to the metallic Co.[246] The peak centered at 780.1 eV is attributed to Co^{2+} suggests the partial oxidation of the surface.[108,247,248] The fitted components centered at the binding energy of

782.0 and 786.3 eV correspond to Co^{3+} and Co2p satellite peaks which are similar to previous reports.[249]

The N1s peak indicates two contributions. The peak at 398.1 eV confirms the presence of the Co-N species on CoN. The high binding-energy component noted at 400.4 eV is likely from the incomplete reaction of mesoporous mixed-oxide with NH_3. This feature is most of the time detected at the surface of high energy metal nitrides such as metallic Ni_3N nanosheets cobalt molybdenum nitrides.[250,251] Similarly, **Figure 3.12b** displays high-resolution peak images of W and N in the WN sample. The W4f is fitted in two peaks centered at 35.7 eV and 37.8 eV W-O in ($4f_{7/2}$) and ($4f_{5/2}$) respectively. On the other hand, the components at 33.4 eV and 35.2 eV, corresponding to metallic tungsten in WN. Also, their N1s spectra also exhibit metal-N peaks at 397.1 eV and 399.4 eV, while the N-H peaks are centered at 401.9 eV. These results mean that the tungsten has been successfully combined with the nitrogen element. Also, there is a slight reduction in the oxide with NH_3.

As shown in **Figure 3.12c,** the high-resolution XPS of Cr and N in CrN. Cr2p exhibits two doublet binding energy Cr ($2p_{3/2}$) and Cr ($2p_{1/2}$); each one is divided into two components and assigned to the Cr-N and Cr-O.[108,248,249,252] The N1s spectrum exhibits two components that can be associated with the Cr-N peaks at 396.6 eV and the N-H bond centered at 398.9 eV (in accordance with previous

reports).[108,248,249,252]

According to **Figure 3.12d,** the high-resolution Ni2p, Fe2p and N1s spectra of mesoporous bimetallic iron-nickel nitride. Ni2p exhibits three main $2p_{3/2}$ peaks at 852.6 eV, 855.3 eV and 861.0 eV, which can be attributed to Ni-N, Ni-O and Ni satellite peaks. They coincide with the $2p_{1/2}$ peaks at 869.9 eV, 873.0 eV and 879.0 eV.[250,251] For Fe2p component, four peaks can be observed at 707.1 eV ($2p_{3/2}$) ,720.5 eV ($2p_{1/2}$), 711.4 eV ($2p_{3/2}$) and 724.7 eV ($2p_{1/2}$). These are assigned to metal-Fe, Fe^{3+} in the oxide.[240,253,254] The Fe satellite peaks are located at 718.2 and 732.0 eV. As far as N1s spectra can be divided into two peaks at 397.62 and 399.57 eV, which in turn can be assigned to Ni/Fe-N bond and N-H.[108,253,255,256]

The structural, textural, and spectroscopic results confirm the formation of mesoporous TMOs and subsequent formation of corresponding nitrides; which retain the mesoporous nature.

3.3 Conclusions

In summary, a series of ordered mesoporous TMN materials namely CoN, WN, CrN and Ni_3FeN are successfully synthesized using a hard-template-based method, and rapid-nitridation process within 30 min using a rather modest (in comparison with most ammono thermal processes) temperature range of 330-800°C. Utilization of (i) ordered porous precursors, (ii) pre-heating and (iii) pre-

passing the ammonia for rapid-nitridation process is proved to be the key factors for efficiently shortening the nitridation and suppressing the closure or collapse of the mesoporous structures of TMNs materials.

These results indicate that the template-based rapid-nitridation approach for the synthesis of mesoporous nitrides is indeed an effective means of generating catalysts in a rapid and readily scalable manner. Hence this work paves way for a promising way to produce ordered mesoporous nitrides for a wide range of applications.

Chapter 4

Metal Organic Framework-derived Porous Fe_2N Nanocubes by Rapid-nitridation for Efficient Photocatalytic Hydrogen Evolution

4.1 Introduction

According to the section on TMN properties in **chapter 1**, TMN represents an important category of materials with interesting optoelectronic, catalytic, electrochemical, and structural functions.[257–261] In particular, the Pt-group like properties of TMNs lead to significant binding and hence strong adsorption of hydrogen. These characteristics make them promising in the field of catalytic hydrogen production.[114,122,123,125,250,262,263] Meanwhile, based on the rapid-nitridation method in **chapter 3**, mesoporous TMNs had been successfully synthesized. However, the hard template method is relatively complex and not convenient for large scale production of TMNs. Thus, another type of porous material precursor is required.

As a subclass of MOFs, Prussian blue (PB) created from the supramolecular assembly of iron components with N-containing organic ligands has attracted considerable interest. This is due to its diverse architectures and morphologies it offers.[264] In fact, there exist reports on topotactic transformation for the fabrication of various nanomaterials derived from PB or PB analogues. Materials obtained using this approach include porous metal phosphates, sulfides, carbides, oxides and so on.[265–268] However, PB-derived porous metal nitrides have not been explored extensively. Previously, the synthesis of PB-derived metal nitrides was reported, which yielded nanoparticles without substantial porosity.[122] Therefore, a novel synthesis process is highly desirable for achieving MOF-derived porous metal nitrides which retain the specific structure of the parent precursor. This would hold significant promise for

catalytic applications.

In this work, the PB precursors are first oxidized and then subjected to rapid-nitridation to obtain porous Fe_2N nanocubes. The nanocubes obtained are phase pure. The process employed for heating is essential to obtaining the material. Using a slip furnace for pre-heating and rapid cooling also reduces the reaction time. The samples obtained thus are sensitized using Eosin-Y (EY) in photocatalytic HER. PB-derived porous Fe_2N nanocube has been synthesized while maintaining the pattern and structure of the parent MOF precursor. Besides, the performance of cube-like Fe_2N is duly rationalized using DFT-based calculations and its metallic nature is also duly elaborated. The superior metallic conductivity of Fe_2N boosts the separation and migration of charge carriers excited from EY. Besides, the porous structure of PB-derived Fe_2N nanocube contributes to the high density of active sites, which in turn yields desirable kinetics for photocatalytic hydrogen evolution. The optimal Fe_2N/EY system exhibits excellent photocatalytic hydrogen evolution performance with a H_2 generation rate at 14.5 mmol $g^{-1}h^{-1}$.

4.2 Results and discussion

4.2.1 Synthesis and characterizations of the MOF-derived porous samples

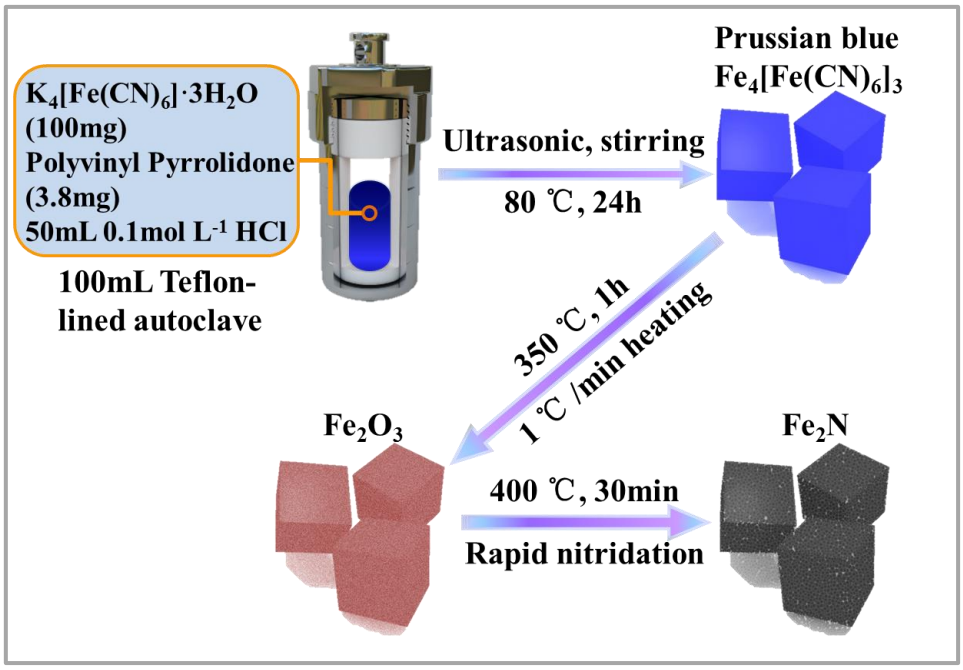

Figure 4.1 Schematic illustration of the synthesis of PB cubic MOF under acidic aqueous solution environment using $K_4[Fe(CN)_6]$, PVP (K30).

As shown in **Figure 4.1**, PB-derived Fe_2N nanocube has been synthesized via a two-step process, i.e. oxidation followed by rapid-nitridation. In brief, PB is first synthesized via a hydrothermal method.[269] Then, PB precursors are heated in air at 350℃ for 1 h forming Fe_2O_3. Finally, the as-prepared Fe_2O_3 is treated in the NH_3 atmosphere at 400℃ for 30 min. This is in fact the rapid-nitridation step that yields Fe_2N. The typical Rietveld refined XRD patterns of the as-prepared samples are shown in **Figure 4.2a-c**. PB precursor, the iron oxide derived from it, and the corresponding nitride belongs to the Fm-3m, Fd-3m and Pbcn space groups, respectively. The details of the results can be seen in **Table 4.1**; there is no indication of oxygen or nitrogen vacancies. Hence the occupancies for oxygen and nitrogen sites are fixed at 1.0. Notably, for the iron oxide sample, the yellowish-brown sample suggests that Fe^{3+} makes up the majority of the

compounds. Refinement shows that there are obvious vacancies at the iron sites (the site occupancy of Fe is only about 0.6 ~ 0.7 as shown in **Table 4.2**). However, the Fe occupancy of the iron nitride sample is 0.9398 (**Table 4.3**), which is consistent with the simple model of the fully nitrogenated Fe_2N.

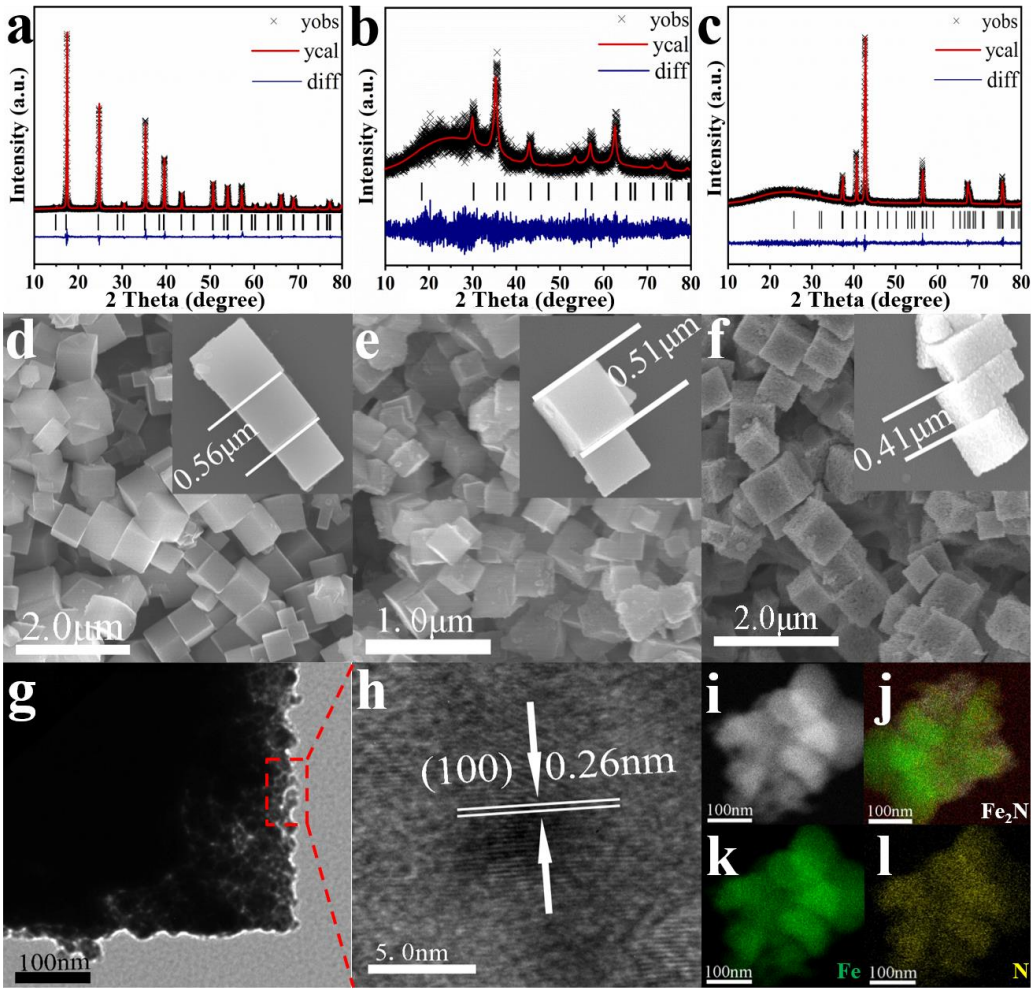

Figure 4.2 (a,b,c) Rietveld refined XRD pattern and (d,e,f) SEM images of PB, Fe_2O_3 and Fe_2N as well as inset show their cube sizes in high magnification. (g) Low magnification of TEM image, (h) HRTEM images and (i-l) the elemental mapping images of Fe_2N.

Table 4.1 Refined crystal structure parameters of PB at room temperature.

Atom	g	x	y	z
Fe1	0.8477	0	0	0
Fe2	1	0.5	0	0
Fe3	0.4519	0.25	0.25	0.25
C	1	0.1944	0	0
N	1	0.2987	0	0

Table 4.2 Refined crystal structure parameters of Fe_2O_3 at room temperature.

Atom	g	x	y	z
Fe1	0.7036	0.125	0.125	0.125
Fe2	0.6380	0.5	0.5	0.5
O	1	0.2437	0.2437	0.2437

Table 4.3 Refined crystal structure parameters of Fe_2N at room temperature.

Atom	g	x	y	z
Fe	0.9398	0.2471	0.1211	0.0838
N	1	0	0.3766	0.25

Notes: Numbers in parentheses are standard deviations of the last significant digit. **g**: site occupancy.

The morphology of the as-prepared samples has been observed by SEM images. As

shown in **Figure 4.3**, PB exhibits uniform cube-like morphology with a smooth surface. Its average size is found to be ~0.53 µm. After the oxidation process, Fe_2O_3 retains the cube-like morphology while its size shrinks to ~0.47 µm. This size shrinkage is due to the oxidation of the ligands in PB. As shown in **Figure 4.2d-f**, further nitridation of Fe_2O_3 nanocubes leads to the formation of Fe_2N with a rougher surface and marginally smaller size (~0.43 µm). TEM analysis clearly indicates the coarse surface associated with the Fe_2N cube (**Figure 4.2g**). In addition, the lattice fringes in the HRTEM of Fe_2N indicate the interplanar distance of ~0.26 nm (**Figure 4.2h**). This corresponds to the (100) crystalline planes of Fe_2N, which confirms the XRD results. Furthermore, elemental mappings (**Figure 4.2i-l**) confirm the homogeneous distribution of Fe and N contents in the binary Fe_2N sample.

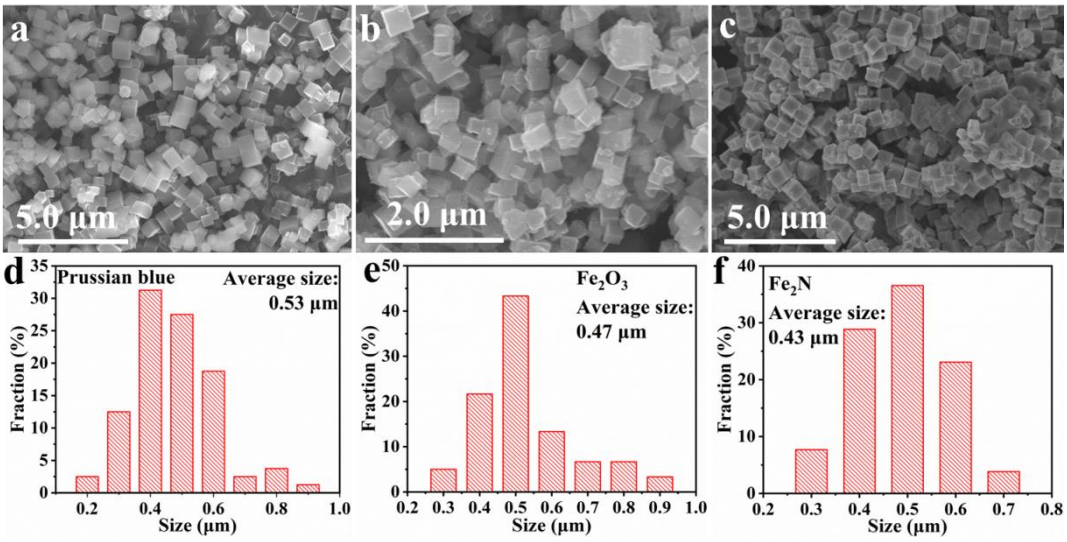

Figure 4.3 Low magnification of SEM image of (a-c) PB, Fe_2O_3 and the Fe_2N that was synthesized by oxidation and nitridation; (d-f) histograms showing the distribution of diameters associated with PB, Fe_2O_3 and Fe_2N cubes.

It is important to note that the oxidation step plays a critical role in forming Fe_2N nanocubes by retaining the morphology of PB. The oxidation process plays an important role in enabling the contraction for the nanocubes to a certain extent so that no collapsing happens in the nitridation process. As shown in **Figure 4.4**, although pure phase metal nitride is observed, direct rapid-nitration of PB leads to collapsed Fe_2N particles. In addition, the purity and morphology of PB-derived Fe_2N samples are also heavily influenced by the nitridation time and temperature.

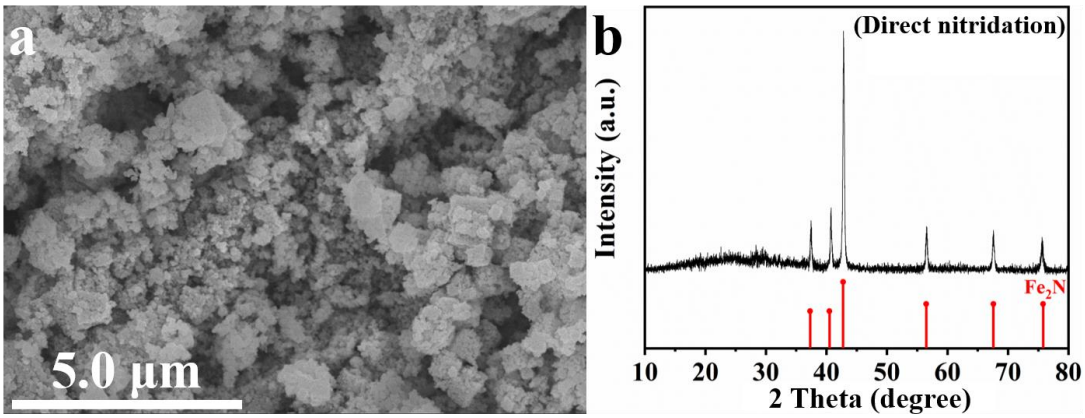

Figure 4.4 (a) The Fe_2N synthesized by direct nitridation (prolong to 2 hours reaction) from the precursor. (b) XRD pattern of Fe_2N derived from direct nitridation (prolong to 2 hours reaction).

XPS is employed to investigate the surface compositions and chemical states of the samples. As shown in **Figure 4.5**, Fe 2p of PB exhibits four main peaks at 708.0 eV ($2p_{3/2}$), 720.9 eV ($2p_{1/2}$), 709.4 eV ($2p_{3/2}$) and 722.6 eV ($2p_{1/2}$) with their satellite peaks at 712.7 eV and 726.3 eV. These peaks can be associated with the components of Fe^{2+} and Fe^{3+}, respectively.[270–272] For sample of Fe_2O_3, the Fe 2p state has also shown four

main peaks at 709.6 eV ($2p_{3/2}$), 723.2 eV ($2p_{1/2}$), 711.7 eV ($2p_{3/2}$) and 725.3 eV ($2p_{1/2}$), which demonstrate the existence of Fe^{3+} in oxide.[273–275] The two corresponding satellite peaks are located at 718.1 eV and 730.8 eV. For the Fe_2N sample, the peaks centered at 706.5 eV and 720.3 eV correspond to Fe $2p_{3/2}$ and Fe $2p_{1/2}$ of metallic Fe.[276,277] Besides, the peaks centered at 710.2, 711.7 eV and 723.5, 725.3 eV corresponding to the Fe $2p_{3/2}$ and Fe $2p_{1/2}$ of Fe^{2+} and Fe^{3+} suggest the formation of nitride phase and the surface oxidation in Fe_2N.[278,279] This is in agreement with other reported metal nitrides.[253,255] The N 1s spectra of the Fe_2N sample can be divided into three peaks at 396.13 eV, 397.84 eV and 399.48 eV, respectively, which in turn can be assigned to metal nitride, pyridinic-N and pyrrolic-N.[253,255]

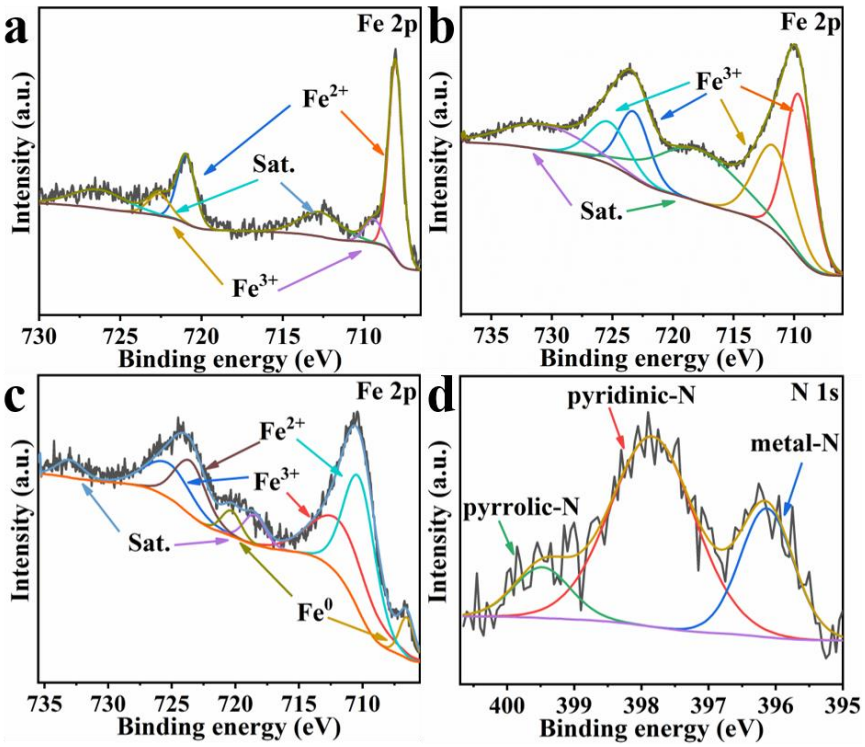

Figure 4.5 The High-resolution XPS spectra for Fe 2p of (a) PB, (b) Fe_2O_3 and (c) Fe_2N as well as (d) N 1s of Fe_2N.

The N_2 adsorption-desorption isotherms and pore structure parameters of PB and Fe_2N samples are summarized in **Figure 4.6** and **Table 4.4**. The specific surface area of PB is 5.74 m^2g^{-1}, which is consistent with previous reports.[264] It can be clearly seen that the porous structure of PB is retained during oxidation and rapid-nitration processes. In fact, the surface area of the Fe_2N sample (10.12 m^2g^{-1}) is larger than that of PB. This is due to the roughness that is brought about during the processing stages.

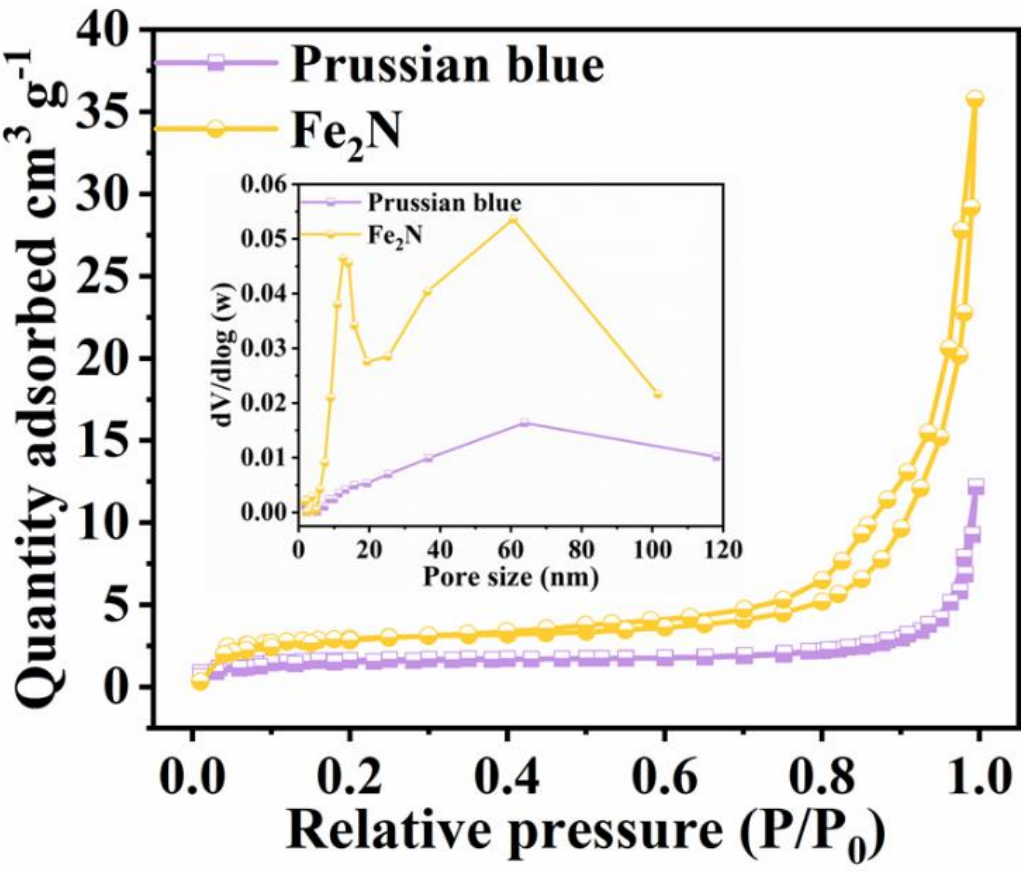

Figure 4.6 N_2 adsorption-desorption isotherms and the corresponding pore size distribution curves (inset) of PB and Fe_2N.

Table 4.4 Porosity characters of PB and Fe_2N.

Photocatalyst	**BET surface area (m^2g^{-1})**	**Mean pore size diameter (nm)**	**Pore volume (cm^3 g^{-1})**
PB	5.74	36	0.017
Fe_2N	10.12	24	0.054

4.2.2 Photocatalytic activity characterization

The photocatalytic hydrogen evolution activities of the Fe_2N sample under different conditions are investigated using EY dye and TEOA as the photosensitizer and the electron donor, respectively. The sacrificial agent would be consumed during the reaction but the input amount is in excess. As can be seen in **Figure 4.7b**, with an increase in the mass of EY, the amount of evolved hydrogen increases until it reaches a maximum value (14.5 mmol $g^{-1}h^{-1}$). This result comes from the condition of the maximum EY amount of 80 mg (while the mass of catalyst is still 5 mg). This is consistent with the fact that the dye indeed sensitizes and provides sufficient electrons for the reaction. This is in fact consistent with the literature.[280] Furthermore, the increase of dye concentration improves the adsorption of EY on the Fe_2N surface, which makes a higher hydrogen evolution rate.[280] Beyond the optimal dye loading, there is a reduction in the activity. This is likely due to the light shielding effect, which means that the light absorption by redundant dye decrease the efficiency of light utilization.[281,282] It means that beyond a certain optimal concentration, EY in a free

state in fact and it quenches the reaction on the active sites. This also prevents sufficient absorption of photons necessary for ensuring sufficient reaction rates.

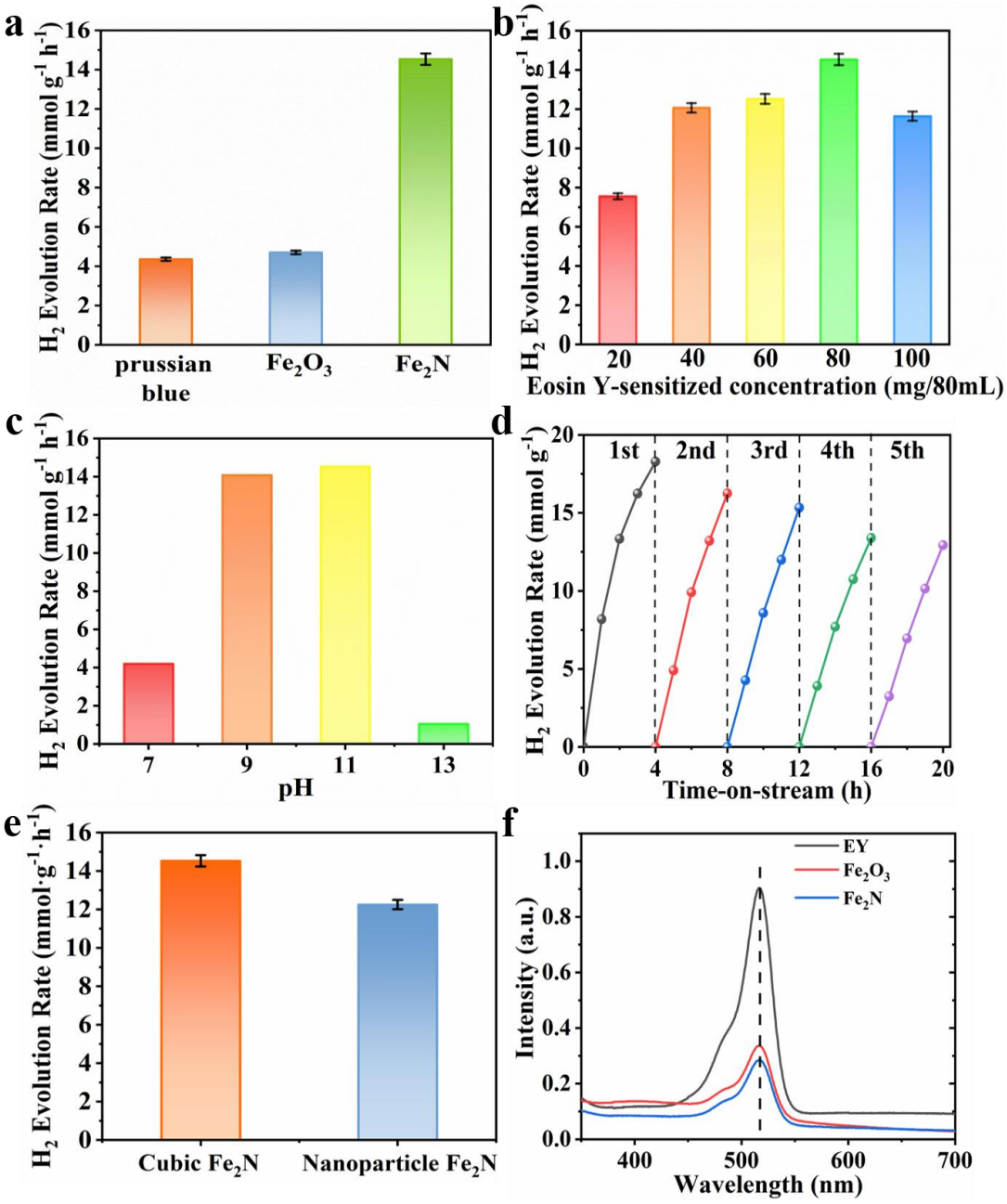

Figure 4.7 (a) Comparison of activity among PB, Fe_2O_3 and Fe_2N under optimal conditions. Photocatalytic H_2 evolution (b) over Fe_2N with different amounts of EY, (c) at different pH values and 80 mg of EY for 2 h using TEOA as the sacrificial agent. (d)

Stability examination for the Fe_2N sample of H_2 production (evacuation every 4 h). (e) Comparison of photocatalytic H_2 evolution rate between the nanoparticle Fe_2N and the nanocubic Fe_2N under optimal conditions. (f) The UV-Vis spectra of pure EY solution, and that of EY solution with Fe_2O_3 and Fe_2N after 2h reaction.

Table 4.5 Comparison of recently reported earth-abundant metal catalysts for photocatalytic Eosin Y-sensitized HER.

Catalyst	**H_2 evolution rate ($mmol\ g^{-1}h^{-1}$) (Cal)**	**pH of reactant aqueous solution**	**Ref.**
Fe_2N	**14.5**	**10% TEOA (pH = 11)**	**This work**
Co-NCNT-800	14.7	10% TEOA (pH = 8.5)	R[283]
NP-FG	2.74	10% TEOA (pH = 11)	R[284]
CoS	1.2	5% TEOA (pH = 7)	R[285]
W-Co_3S_4	12.5	15% TEOA (pH = 11)	R[286]
NiB/GO	6.5	10% TEOA (pH = 11)	R[287]
Ni@MOF-5	9.5	10% TEOA (pH = 11)	R[288]
NiP	2.3	10% TEOA (pH = 11)	R[284]
$Ni(OH)_2/TiO_2$	1.6	5% TEOA (pH = 9)	R[289]
Pt/C_3N_4	0.5	5% TEOA (pH = 9)	R[290]
rGO/MOF/Co-Mo-S	6.8	15% TEOA (pH = 9)	R[280]
Sb doped SnO_2	0.25	10% TEOA (pH = 11)	R[291]

Note: The data of H_2 evolution rate are all calculated from the original data to the unit of **mmol $g^{-1}h^{-1}$**.

Fe_2N exhibits better activity for HER when pH = 11, when compared to the situation wherein pH is set to 9. The observed trends are given in **Figure 4.7c**. Clearly, Fe_2N is well suited for HER in an alkaline condition. **Figure 4.7a** compares the hydrogen production activity of PB, Fe_2O_3 and Fe_2N photocatalyst under irradiation over 2 h of reaction with the usage of 80 mg EY, at a pH = 11. The activity of Fe_2N (14.5 mmol $g^{-1}h^{-1}$) is over three times higher than PB (4.3 mmol $g^{-1}h^{-1}$) and Fe_2O_3 (4.7 mmol $g^{-1}h^{-1}$). The very favorable photocatalytic activity of Fe_2N is aided by the more abundant active sites associated with the nitride phase.[124] In this alkaline condition (pH = 11), the HER activity of Fe_2N is comparable to most of the previously reported photocatalytic EY sensitized systems (**Table 4.5**). Additionally, TON of 57.8 and TOF of 0.016 s^{-1} are obtained when 5 mg of Fe_2N is used. This also proves the considerable catalytic ability of Fe_2N.

If the dye or sacrificial agent component is removed, the H_2 evolution rates of Fe_2N are rather negligible and difficult to be detected. It is proved that in all cases, EY and TEOA as sacrificial agents are necessary for the HER process. In addition to the photocatalytic activity, stability has also been tested through several reaction cycles. As can be seen in **Figure 4.7d**, Fe_2N show slightly decreased activity. This is likely due to the adhesion between the sample and the magnetic stirrer, which in turn leads to a decrease in the

effective interfacial area between catalyst and solution. Moreover, controlled experiments with prolonged reaction times have been tested. As shown in **Figure 4.7e**, the synthesized sample exhibits a pure Fe_2N phase with nanoparticle morphology. The photoactivity of the Fe_2N nanoparticles has also been tested. The H_2 evolution rate of nanoparticle Fe_2N is 12.26 mmol $g^{-1}h^{-1}$, which is lower than that of nanocubic Fe_2N. This demonstrates the morphology and pore structural advantages of the cubic Fe_2N sample to a certain extent. Finally, **Figure 4.7f** has shown the UV-Vis absorption spectra of diluent EY solution, the EY solutions after 2 h reaction with Fe_2O_3 and Fe_2N samples. The results show that Fe_2N has the highest dye degradation efficiency.

4.2.3 Electrochemical characterization

Figure 4.8a displays the CVs of PB, Fe_2O_3 and Fe_2N with obvious cathodic and anodic peaks. In CV measurements, the reaction that processing on the electrode is quasi-reversible. Hence the current density is only related to the electron transfer rate of the electrode materials.[292–295] The current density obtained over the Fe_2N electrode is higher than that obtained over PB and Fe_2O_3. This is again an indicator of Fe_2N's ability to enable the transfer of charge carriers required for catalysis. EIS is carried out and the corresponding Nyquist plots of different samples are given in **Figure 4.8b**. It is observed that the diameter of the semicircle, which means R_{ct} (charge transfer resistance), of the Fe_2N sample, is smaller (~20 Ω) than that of PB and Fe_2O_3. This means the electrons transfer readily from the electrode surface and across the interface double electric layer for the reaction. This in fact is consistent with earlier inferences

drawn from CV; Fe_2N indeed has higher efficient interfacial charge transfer capabilities.[31,296]

Figure 4.8c shows the polarization curves and the overpotential comparison. It is clear that Fe_2N achieves a higher current density at a fixed potential range. For a current density of 10 mA cm^{-2}, the overpotential of Fe_2N (-1470 mV) is lower than that of Fe_2O_3 (-1484 mV). Once again this indicates that the TMN promotes H_2 reduction reaction.[297] Furthermore, specific capacitance performance is measured in a specific region of potentials (**Figure 4.8d**). Fe_2N has a much larger enclosed area than the other two samples, illustrating that Fe_2N can facilitate electronic storage.

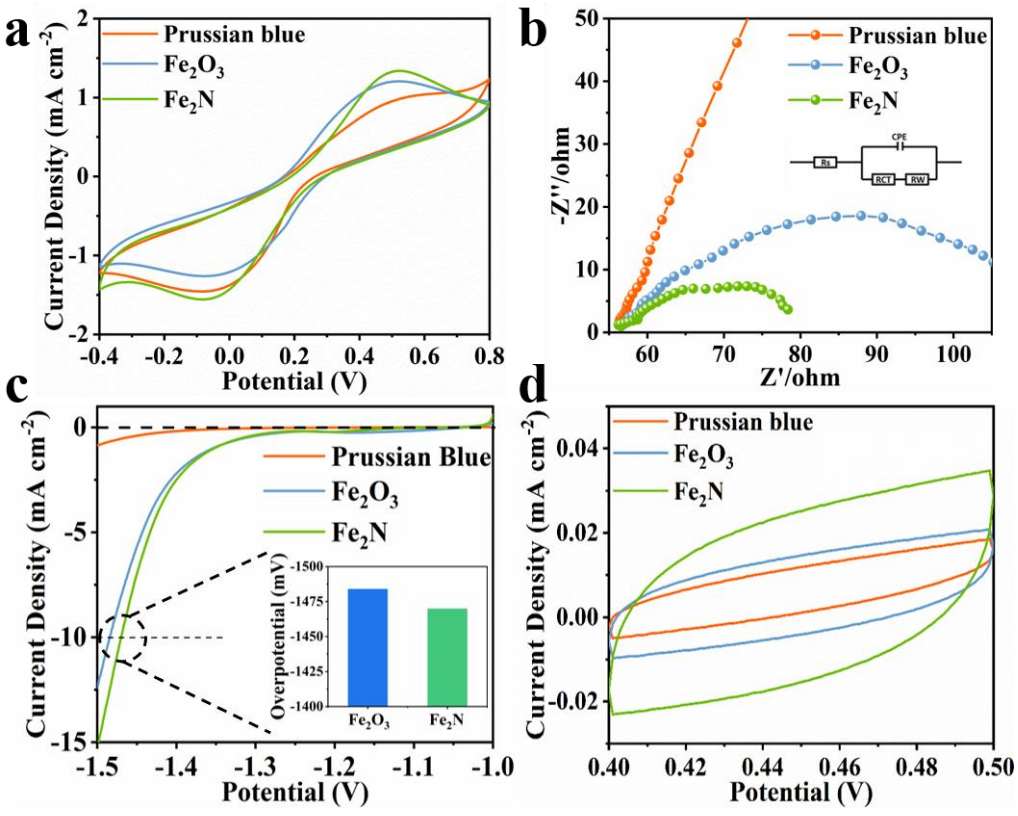

Figure 4.8 (a) CVs, (b) EIS Nyquist plots, (c) polarization curves and (d) specific

capacitance performances (CV) of PB, Fe_2O_3 and Fe_2N.

4.2.4 Theoretical calculation and photocatalytic mechanism

The optimized structure of Fe_2N and the calculated PDOS are presented in **Figure 4.9a** and **4.9b**, respectively. The theoretical calculation clearly illustrates the metallic character of the material according to **Figure 4.9b** and **c**, illustrating the existence of free electrons, which are responsible for the high metallicity of Fe_2N.[298] Besides, **Figure 4.9c** shows that the VB passes through the Fermi level (zero energy) to overlap with the CB, confirming the metallicity character of the material. Considering the DOS plot, while there is p-d hybridization between Fe and N in the energy ranges of -9 to -5.8 eV, the material metallicity mostly arises from the Fe-3d distributions around the Fermi level. The conductivity of TMN is clear from the calculation of DOS, and it is found to be consistent with other reports.[124,259–261,299]

The mechanism of photocatalytic H_2 production enabled through EY sensitized Fe_2N system is proposed in **Figure 4.9d**, which is based on the previous literature.[39,280,300] First, the molecules absorb photons from visible light and form the single excited state EY^{1*}. Subsequently, a more stable three excited state EY^{3*} is formed through an intersystem crossing (ISC). In the presence of TEOA as an electron donor, EY^{3*} is reduced to form $EY^{\cdot-}$. This ion in fact has strong reducing ability. The electrons of $EY^{\cdot-}$ are conducted into the surfaces of Fe_2N owing to its metallic-like properties. A reduction reaction occurs here which results in the production of H_2. At the same time,

reduced EY dye molecules return to the ground state. Because of the considerable ability of dye degradation, electronic storage and transfer of Fe_2N structure, the recombination of photo-generated charges and holes is limited.[280] Therefore, the efficiency of photocatalytic hydrogen production is improved.

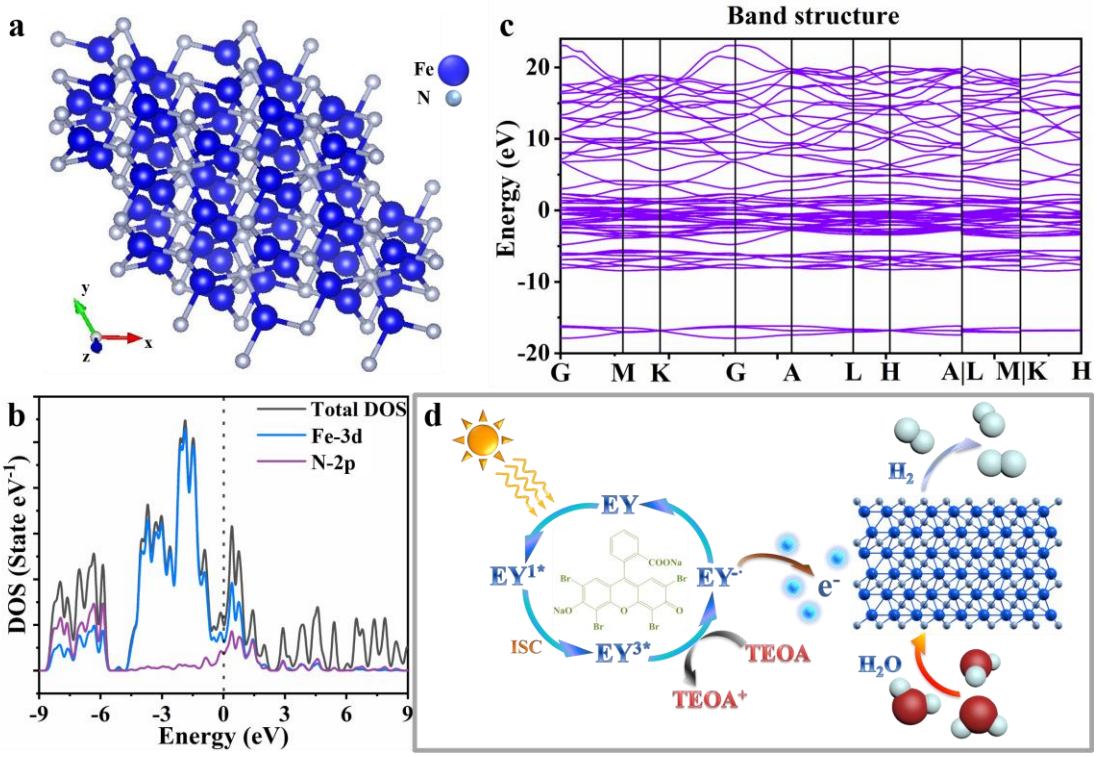

Figure 4.9 (a) Optimized structural representations of bulk Fe_2N, iron and nitrogen atoms are shown in blue and silvery colors respectively. The metallic character of the material is obvious due to the zero band-gap of the plot. (b) Total DOS and Fe-3d, N-2p PDOS projected on iron and nitrogen atoms. The Fermi level is set at zero. (c) The energy band structures where Fermi level is taken at zero. (d) Proposed photocatalytic hydrogen production mechanism over the EY sensitized Fe_2N under visible light irradiation.

4.3 Conclusions

In conclusion, MOF derived porous Fe_2N has been synthesized using a two-step process, oxidation followed by the rapid-nitridation technique. MOF based on PB, which is made from a supramolecular assembly of iron components with N-containing organic ligands, has been employed. Usage of this MOF ensures that the nitride samples retain the shape of the precursor while showing only a nominal shrinkage during the chemical transformation (hence indicating a topotactic transformation). The preparation process is both quick and rather chimie douce (soft chemical).

Fe_2N samples thus obtained have a high specific surface area, and offer abundant exposed active sites for photocatalytic activity. Fe_2N is sensitized using EY for boosting photocatalytic hydrogen evolution. Hydrogen production rates close to ~14.5 mmol $g^{-1}h^{-1}$ are observed, which is considered desirable. The superior conductivity of Fe_2N offers enhanced electron transfer performance between the catalyst and photosensitizer, so that the reduction reaction can be processed faster. Meanwhile, the separated reaction sites of dye degradation by the electron donor of the sacrificial agent and the electron capture by the Fe_2N catalyst also limit the electron-hole recombination, hence yielding the observed high hydrogen production rates. Calculations show that free electrons in Fe_2N, responsible for its metallic-like properties, arise primarily because of Fe-3d. Overall, this work provides a new means of producing MOF derived TMN materials, which in conjunction with suitable dyes, offer high-efficiency and low-cost avenues for making photocatalysts for hydrogen production.

Chapter 5

Metal Organic Framework-derived $Fe_{2-x}M_yN$ (M = Co, Cr, W, V) Nanocubes for Efficient Piezoelectric Hydrogen Evolution

5.1 Introduction

Based on the discussion in **chapter 1**, piezoelectric catalysis is a new strategy that attracted considerable attention for producing hydrogen with a high energy conversion rate. Besides, TMNs have a variety of unique material properties including considerable conductivity, chemical stability, acid and alkali resistance and noble-metal-like properties due to the tunable d-band.[9,17] These advantages are beneficial to the separation of piezo-induced charge carriers and transportation of free electrons, which provide the potential of practical utilization in piezocatalysis.

In addition, the morphology of TMN can be tuned by the synthesis methodology of rapid-nitridation mentioned in **chapter 3** for gaining ordered mesoporous nanostructure with high specific surface area, which can provide large mechanical energy capture area and abundant active sites. Among these synthesis methods of morphological materials, the way of MOF derivation mentioned in **chapter 4** has been regarded as a considerable choice due to the high flexibility of the nanostructural frameworks.[301]

For further improving the piezo-catalytic activity of TMN catalyst, element doping serves as an ideal strategy. This is because the electronic configuration of the d-band of metal centers could be redistributed further after the element doping, which forms a new spin-polarized valence band and leads to the improvement of electron donor and the electrical conductivity.[302] On the other hand, element doping is an efficient strategy for forming the asymmetric properties of piezoelectric materials. This means that the

doped element atoms on the surface have uneven distribution and enhance the piezoelectric performance through the non-centrosymmetric nanostructure.

Herein, the materials of MOF-derived nanocubic Fe_2N with different types of doped elements (Co, Cr, W and V) are completely synthesized. Rapid-nitridation had applied as the synthesized method, which is efficient for retaining the morphology of catalyst. The regular nanocubic pattern of samples has been maintained. The doped Fe_2N have been utilized for piezoelectric catalytic H_2 evolution and the Co-doped Fe_2N has achieved the highest activity (122.8 μmol $g^{-1}h^{-1}$). After tuning the doping ratio, Co and V doped Fe_2N have greatly improved their H_2 evolution performance. According to the control experiments, the sample with nanocubic morphology has a higher H_2 evolution rate than that of the nanoparticle sample. Doped Fe_2N catalysts also have the ability to degrade different types of dye, while improving their H_2 production efficiency. Besides, the DFT calculation has elucidated the activity improvement of doped nitrides.

5.2 Results and discussion

5.2.1 Synthesis and characterizations of the MOF-derived porous samples

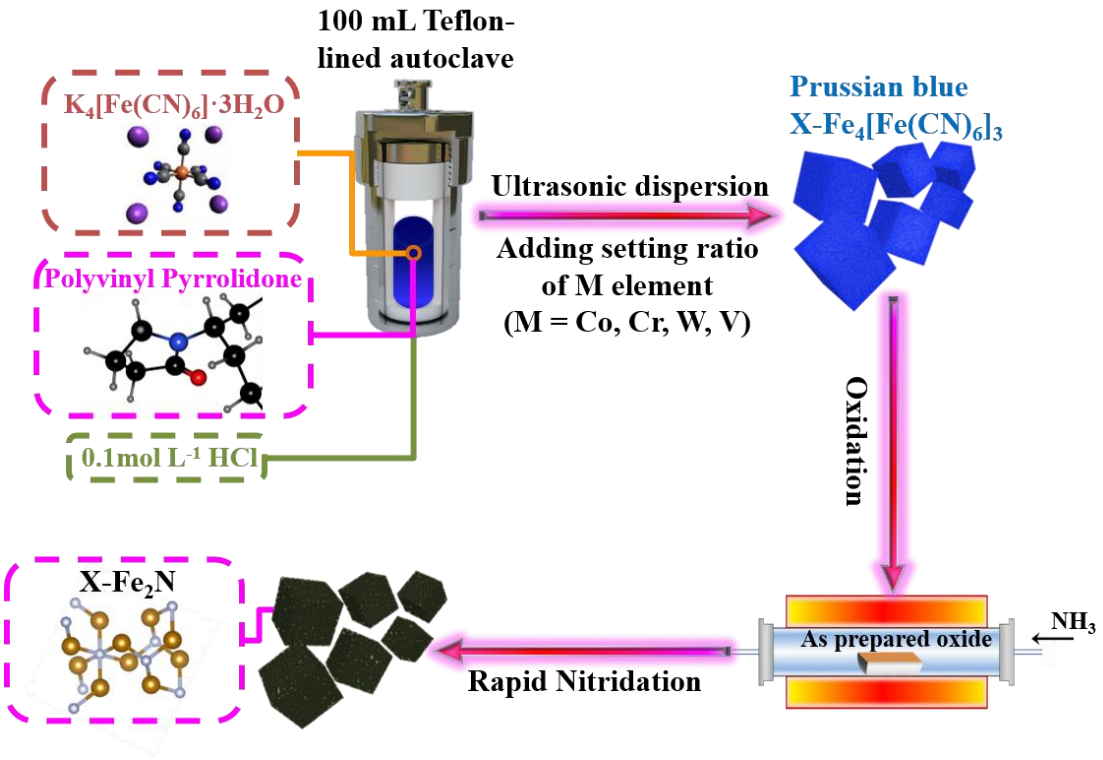

Figure 5.1 Schematic illustration of the synthesis of blank cubic Fe_2N or element doped $Fe_{2-x}M_yN$ (M = Co, Cr, W and V) nanocomposites.

As illustrated in **Figure 5.1**, a series of PB-derived Fe_2N with different types of elements doping (Co, Cr, W and V) have been synthesized through the two-step process of oxidation and rapid-nitridation at 400°C for 30 min. **Figure 5.2** has shown the powder XRD patterns of PB and PB-based doped samples, with their corresponding Fe_2N-based samples. The patterns indicate that all the diffraction peaks are similar and well matched with PB (JCPDS 00-052-1907) and Fe_2N (JCPDS 01-072-2126). However, the series of PB-based samples can be observed a slight peak shift at the angle range of ~17.8°, and that of the series of Fe_2N-based samples can be observed at ~42.9°. They are attributed to (200) and (011) crystal planes of cubic phase PB and hexagonal phase Fe_2N, respectively. Compare to the pure PB sample, all of the doped samples

have slightly increased degrees of this diffraction peak.

In comparison with pure Fe_2N, the Co and Cr doped samples have increased diffraction peak degrees, and the W and V doped samples show decreased degrees. According to the Bragg's Law $2dsin\theta = n\lambda$ (d is interplanar spacing, θ is the X-ray incidence angle, λ is wavelength), the angle shift is attributed to the change of interplanar spacing and lattice constant, which may be due to the doping of atoms with different radius and the contraction of unit cells.[303] Here, the radius of Co and Cr atoms are 1.26 and 1.27 Å, while that of Fe is 1.27 Å, those of W and V are 1.41 and 1.35 Å. It can be found that doping of similar atoms makes the diffraction peaks shift positively, while doping of bigger atoms makes the peaks shift negatively.

Typical Rietveld refined XRD patterns of the as-prepared doped nitride samples are shown in **Figure 5.3**. It can be seen that the calculation results are mainly consistent with the observation results. All of these samples belong to the P-3m1 space group and their lattice constants have been shown in **Table 5.1** and **Table 5.2** in detail. There is no indication of oxygen or nitrogen vacancies in all samples. Thus, the occupancies of nitrogen are fixed as 1.000. The Fe occupancy of the doped iron nitride samples is calculated as 0.950, which is consistent with the default setting doping ratio (5 at%) of other elements, as well as the simulated model of the fully nitrogenated Fe_2N.

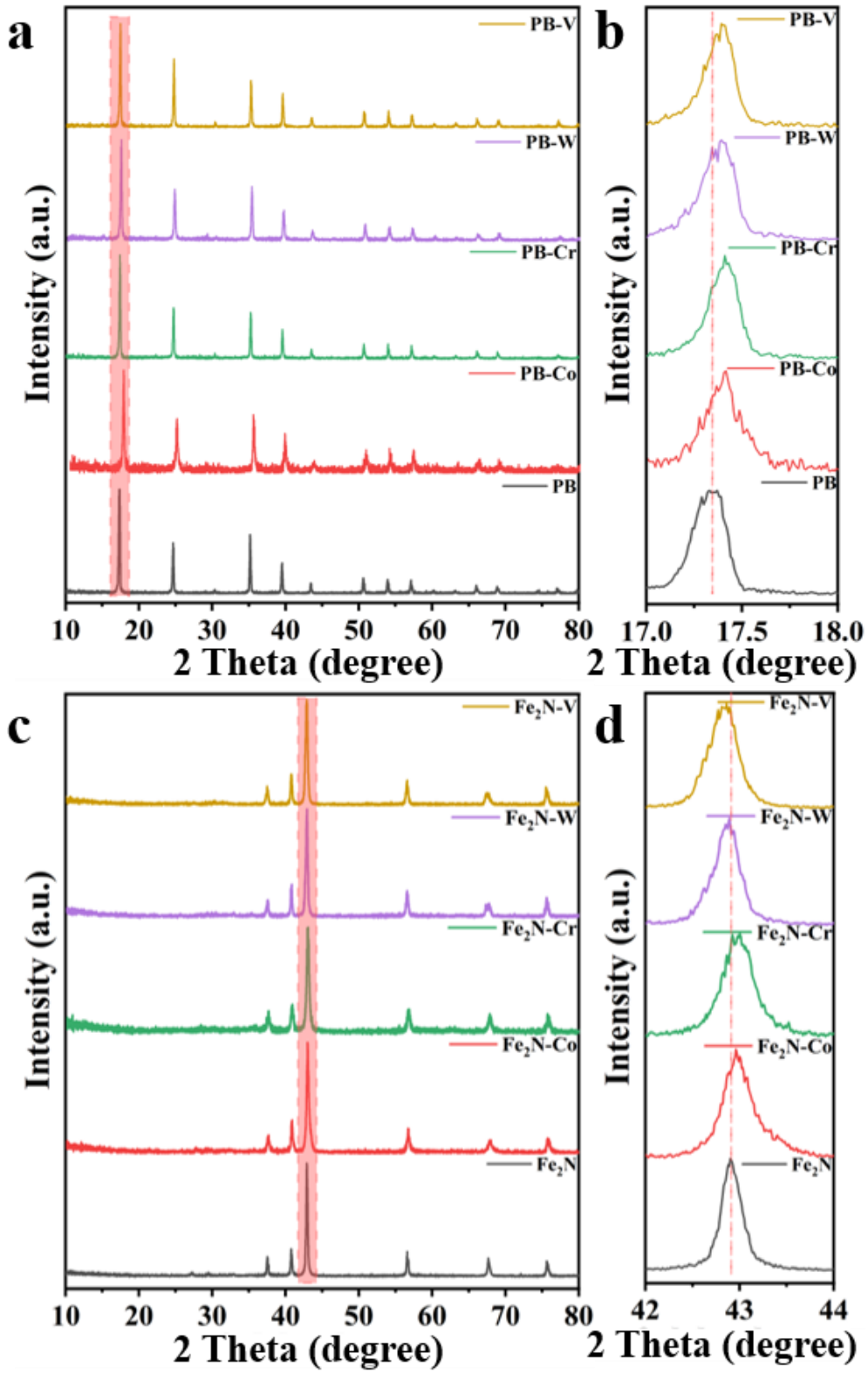

Figure 5.2 The XRD and high-resolution XRD patterns of (a,b) PB and PB-based doped samples with different kinds of elements (Co, Cr, W and V) by a ratio of 5 at%, with (c,d) their corresponding Fe_2N-based samples.

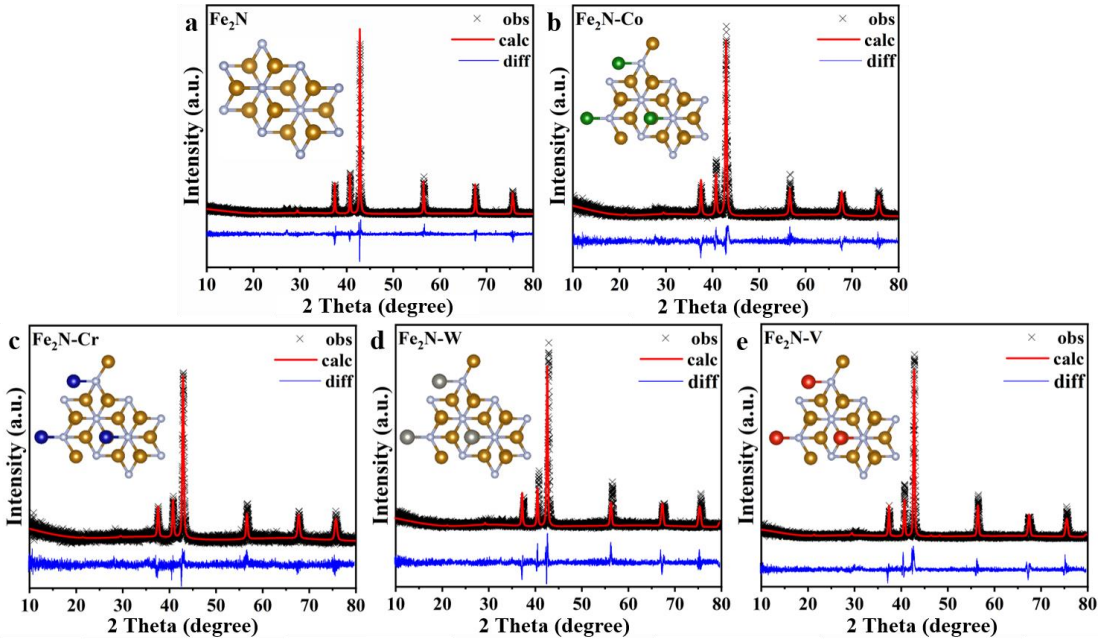

Figure 5.3 The Rietveld-fitted XRD pattern of (a) pure Fe_2N and (b-e) Co, Cr, W and V (5 at%) doped $Fe_{2-x}M_yN$. The insets are the corresponding simulated crystal structure.

Table 5.1 Refined crystal structure parameters of pure Fe_2N at room temperature.

Atom	x	y	z	frac	Uiso
Fe1	0.33	0.33	0.25	1.00	0.01
N1	0.33	0.67	0.50	1.00	0.01
N2	0.67	0.33	0.00	1.00	0.01

Table 5.2 Refined crystal structure parameters of X-Fe_2N (X = Co, Cr, W and V) at room temperature.

Atom	x	y	z	frac	Uiso
Fe1	0.33	0.33	0.25	0.95	0.01
X1	0.33	0.33	0.25	0.05	0.01
N1	0.33	0.67	0.50	1.00	0.01
N2	0.67	0.33	0.00	1.00	0.01

Notes: frac: site occupancy, **Uiso**: isotropic thermal parameter.

The morphology of the as-prepared samples has been tested by SEM in **Figure 5.4**. PB exhibits uniform cube-like morphology with a smooth surface with an average size of ~0.64 μm. After the oxidation process, Fe_2O_3 maintains the cube-like morphology with a decreased size of ~0.55 μm. Further nitridation of the oxide cubes produces the Fe_2N cubes with a rougher surface and a marginally contractive size of ~0.43 μm. The size shrinkage in both steps is due to the oxidation and nitridation of ligands in PB. Statistics associated with diameter have been exhibited in **Figure 5.5** with their average particle sizes.

According to the SEM images and histograms, it can be found that all of the doped samples have maintained their cubic morphology in each process stage. Their average sizes, on the whole, follow the shrinkage trend at pace with the oxidation and nitridation process. Specially, the series of Co-doped samples show a relatively extreme small size (0.16, 0.11 and 0.10 μm for Co-doped PB, Fe_2O_3 and Fe_2N). The reason is probably

that the Co dopants remarkably influence the growing process of MOF, leading to the formation of the framework in advance with a much smaller size.[304]

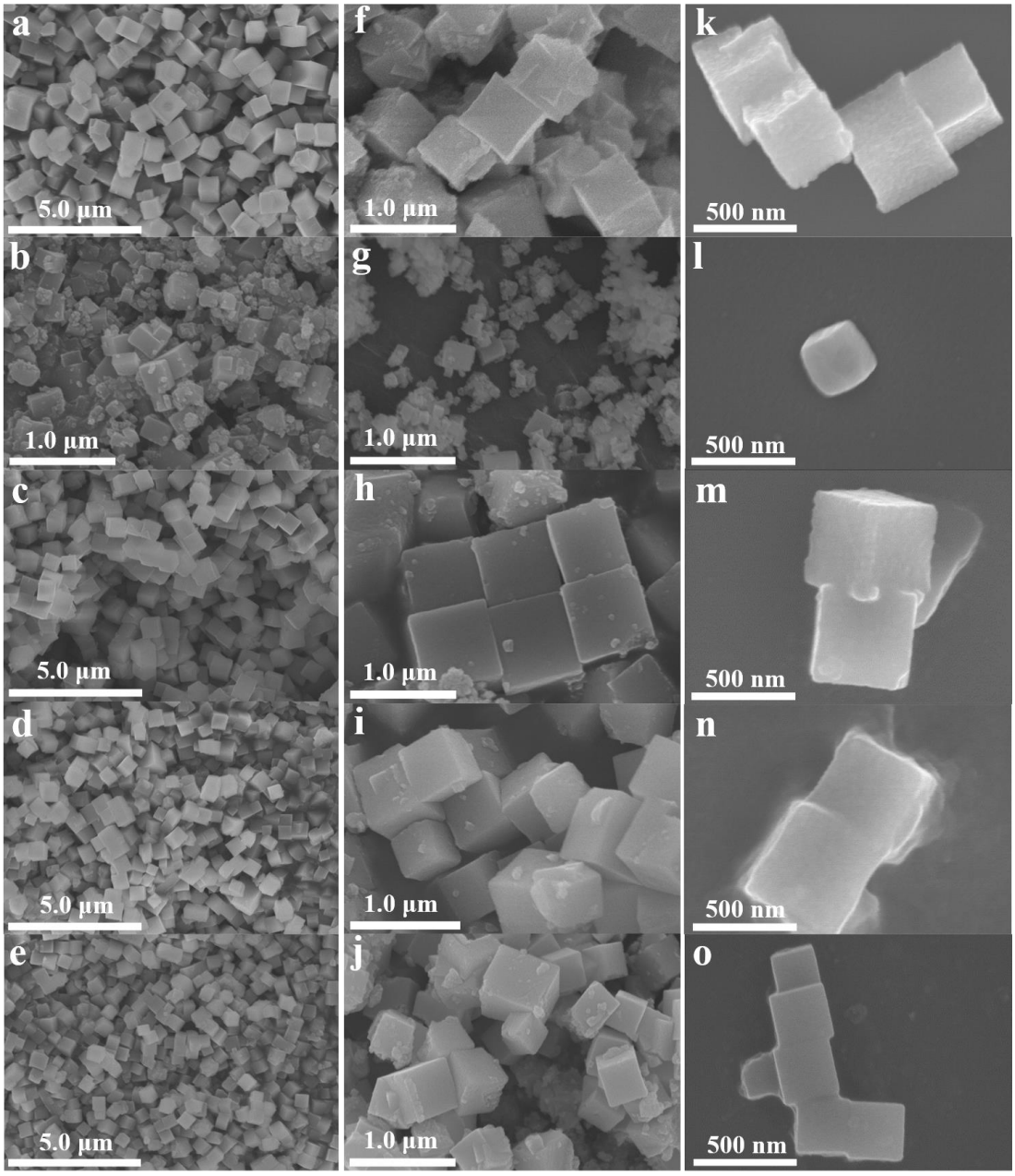

Figure 5.4 The SEM images of (a) PB and (b-e) the series of Co, Cr, W and V doped PB samples (5 at%), the corresponding oxide (f) Fe_2O_3 and (g-j) doped PB derived X-Fe_2O_3, and the corresponding nitride (k) Fe_2N and (l-o) doped oxide derived X-Fe_2N.

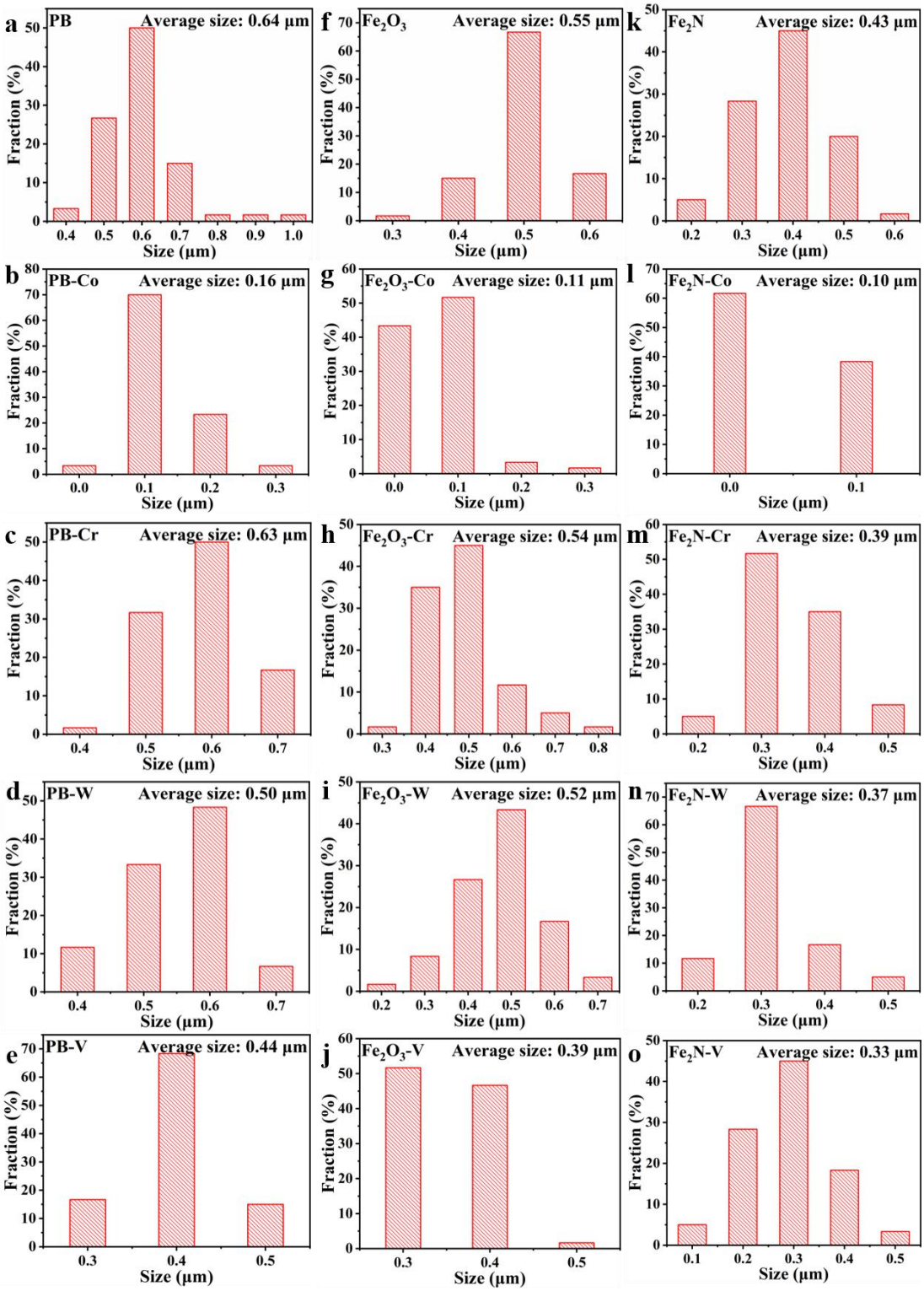

Figure 5.5 The diameter statistic histograms of PB, Fe_2O_3 and Fe_2N cubes and their corresponding Co, Cr, W and V element doped cubes.

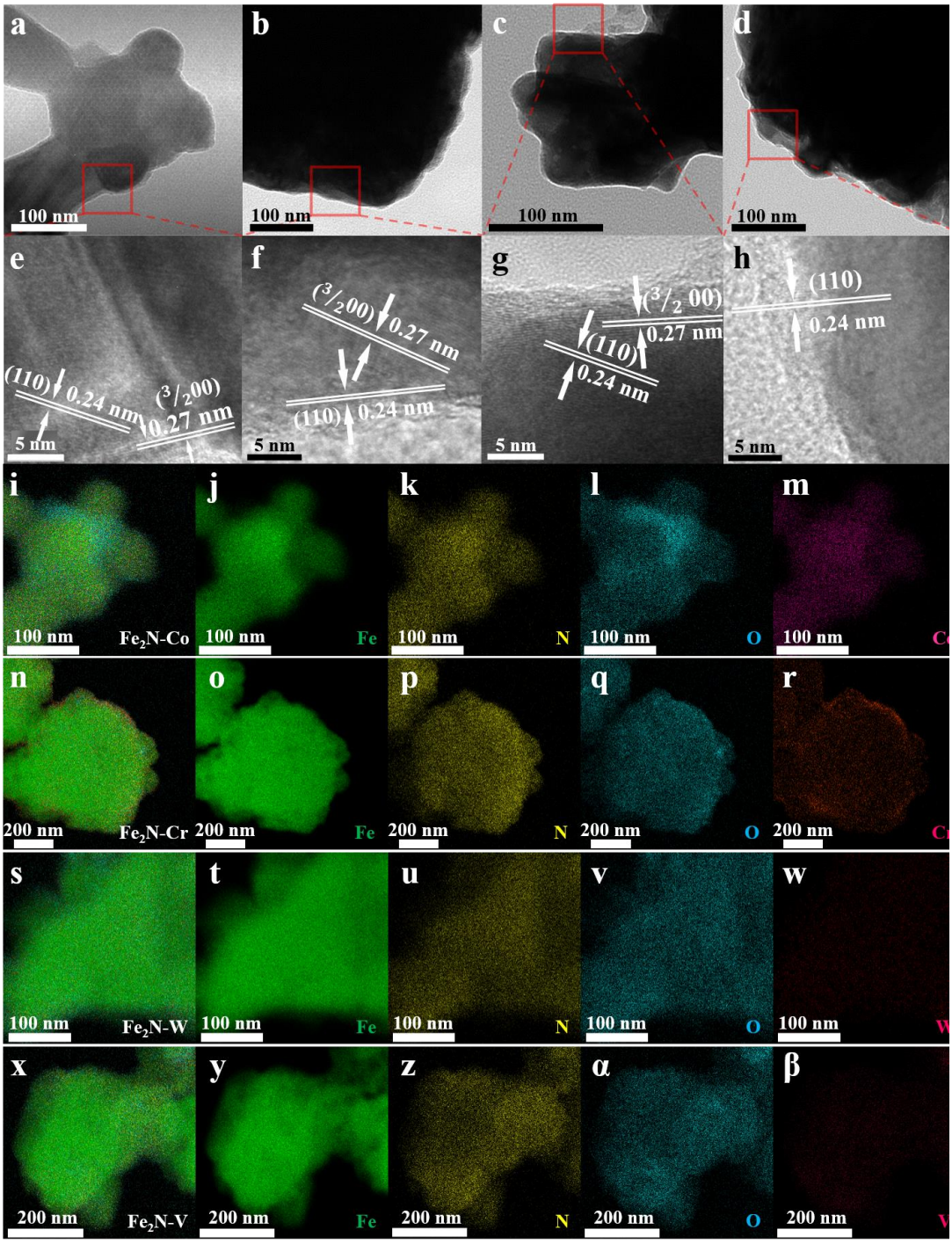

Figure 5.6 (a-d) Low magnification TEM, (e-h) high-resolution TEM images and (i-β) elemental mapping images of Co, Cr, W and V doped Fe_2N samples.

The TEM analysis in **Figure 5.6** has clearly illustrated the cubic shape associated with Fe_2N cubes. Besides, the lattice fringes have been exhibited in high-resolution TEM

images. The interplanar distances of Co, Cr, and W doped Fe_2N are measured as ~0.27 and ~0.24 nm, which indicates the ($^3/_2$00) and (110) crystalline planes, respectively. Moreover, the angles between these two plane directions are near 30°, which is consistent with the results of Rietveld refined calculation. Simultaneously, the interplanar distance of V doped Fe_2N is ~0.24 nm, which is consistent with the (110) crystalline plane. Furthermore, elemental mappings confirm the homogenous distribution of each element's contents in all the doped Fe_2N samples. The obscure color distributions of W and V illustrate that their doping ratios seem much less than those of Co and Cr, which is consistent with the result of the element content test below.

In order to explore the effect of different doping ratios, a decreased ratio of Co (2.5%) and an increased ratio of V (15%) have been doping into PB and the corresponding Fe_2N sample has been synthesized. **Figure 5.7** have shown the XRD patterns of these two types of PB and Fe_2N samples. It can be seen that the patterns of samples with different doping ratios are similar, which indicates that the change of doping ratio would not influence the formation of the pure phase. The SEM images (**Figure 5.7e** and **f**) have illustrated that the doped samples with various ratios have still maintained cube-like morphology to a certain extent.

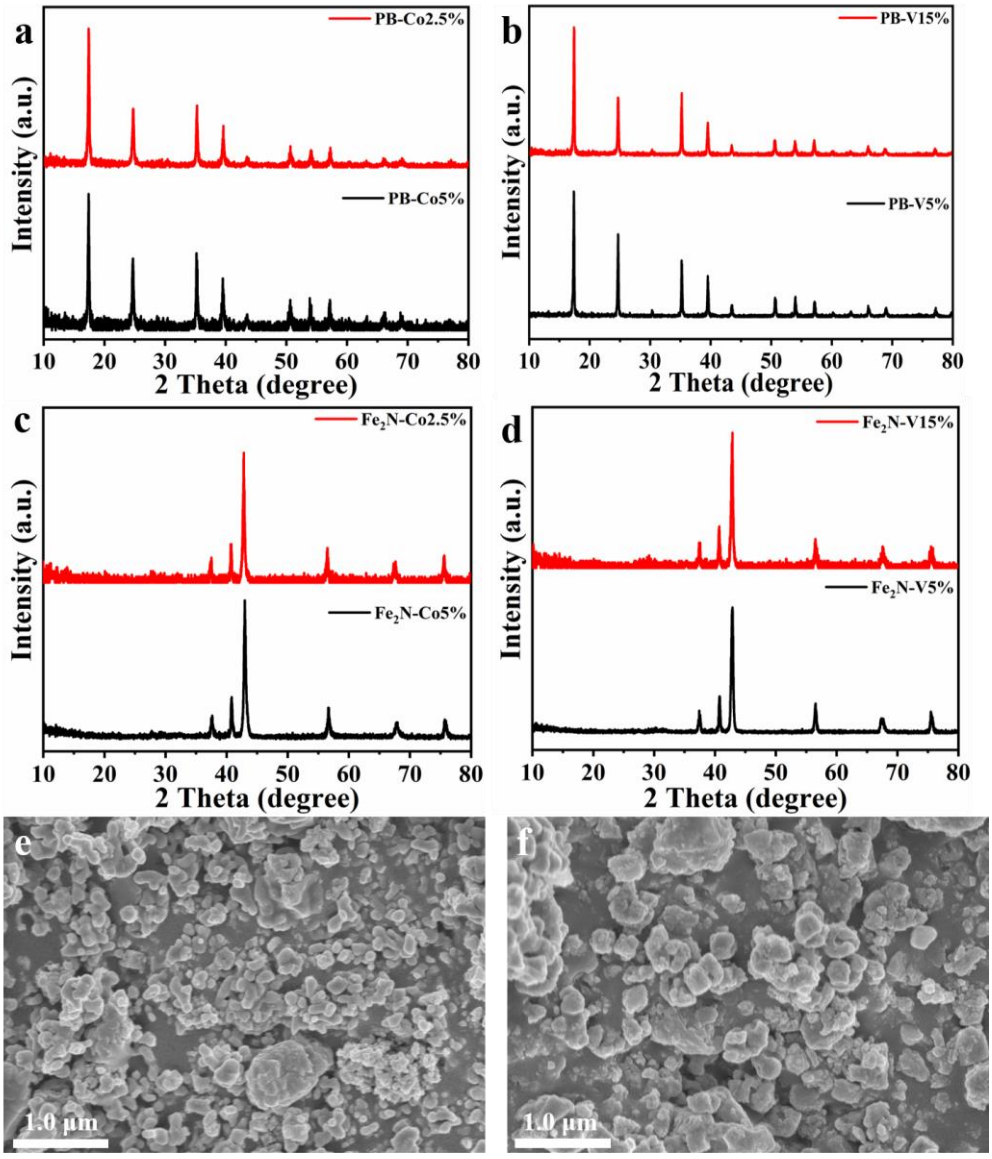

Figure 5.7 The XRD patterns of (a) Co doping PB by a ratio of 2.5% and 5%; (b) V doping PB by a ratio of 15% and 5% (c) the corresponding Co doped Fe_2N sample, (d) the corresponding V doped Fe_2N sample. The SEM images of (e) 2.5% Co and (f) 15% V doped Fe_2N samples.

It is worth mentioning that the oxidation process is important in forming the Fe_2N nanocubes with maintained cubic morphology from PB. This is because the oxidation enables the contraction of the nanocubes and relief the collapse during the nitridation

process. Besides, the rapid-nitridation process is also significant for retaining morphology. In contrast with the rapid-nitridation synthesized sample, the Fe_2N particles that were synthesized by the long-term nitridation process have also been tested by XRD and SEM. **Figure 5.8** has exhibited their similar XRD patterns and different kinds of morphology. These results mean that although the pure phase of Fe_2N has been produced, the long-term nitridation leads to the collapse of Fe_2N nanocubes and produces nanoparticles.

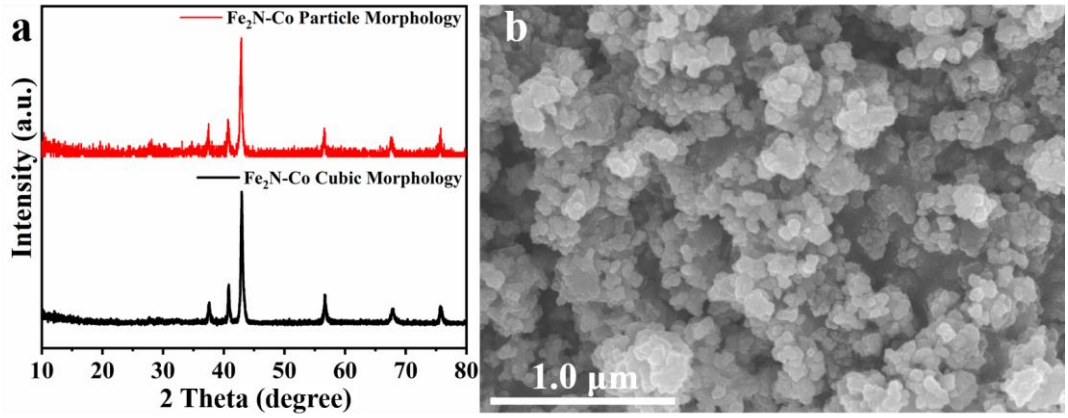

Figure 5.8 (a) The XRD patterns of Co (5 at%) doped Fe_2N that synthesized by rapid-nitridation (400°C, 30 min) and long-term nitridation (400°C, 5°C min^{-1}, 2 h). (b) The SEM images of Co (5 at%) doped Fe_2N by long-term nitridation.

XPS is employed to further investigate the surface elemental components and chemical states of the samples. As shown in **Figure 5.9a**, the high-resolution spectra depict Fe 2p orbitals. For the Fe_2N sample, the dominant $2p_{3/2}$ peaks of Fe^{3+}, Fe^{2+} and metallic Fe^0 center at 710.3 eV[305], 708.6 eV[306] and 706.9 eV[253]. The satellite peak is located at 717.1 eV. This result suggests that the valence state of Fe ions in the Fe_2N sample is

a mixture of Fe^{3+} and Fe^{2+}, which is caused by the surface ultrathin oxidized layer of Fe_2N. This ultrathin layer can protect the TMN from further oxidation and does not offer any hindrance to electron transport.[190]

For other doped Fe_2N samples, all the peaks of Fe^{3+}, Fe^{2+} and Fe^0 have shown various slight shifts within 0.3 eV. Co-doped Fe_2N exhibits peaks of Fe^{3+} $2p_{3/2}$, Fe^{2+} $2p_{3/2}$ and Fe^0 $2p_{3/2}$ at 710.7 eV, 708.8 eV and 706.7 eV. This displays shifts within 0.2 eV compared to those of the pure Fe_2N sample, which indicates that the electronic structure has not been significantly changed by element doping.[302] The Fe^{3+} peaks of Co, Cr and W doped samples have relatively large areas compared to the other three samples, which make their shapes of spectrum different from the pure and V doped samples. This indicates the Fe^{3+} component of these three types of samples has larger proportions than the other two types.

Figure 5.9b has exhibited that the N 1s spectra of the series of Fe_2N samples can be divided into three or four peaks. For all the five kinds of samples, the peaks at 396.3 eV and the region of slightly negative shift can be assigned to metal-nitrogen bonds.[307] For the middle dominant peaks, compared to that of pure Fe_2N (397.9 eV), the Co, Cr and W doped samples have slightly negative shift peaks at 397.7 eV, while V doped sample showing a peak with obscure shift (397.9 eV). These middle dominant peaks can be assigned to pyridinic nitrogen due to the residual organic ligand structure from the MOF precursor.[307,308] The third peak of Fe_2N centered at 399.8 eV, which

corresponds to pyrrolic nitrogen.[307,308] Compare to Fe_2N, the corresponding peaks of other doped samples have a slight shift within 0.2 eV. The pure and Co, Cr doped samples can be found in the oxidized nitrogen peaks at the range of about 402 eV. Reasonably, the W and V samples should have similar peaks, but the results have not shown any obvious signal at the corresponding range, which may due to the trace amounts which are hard to detect.

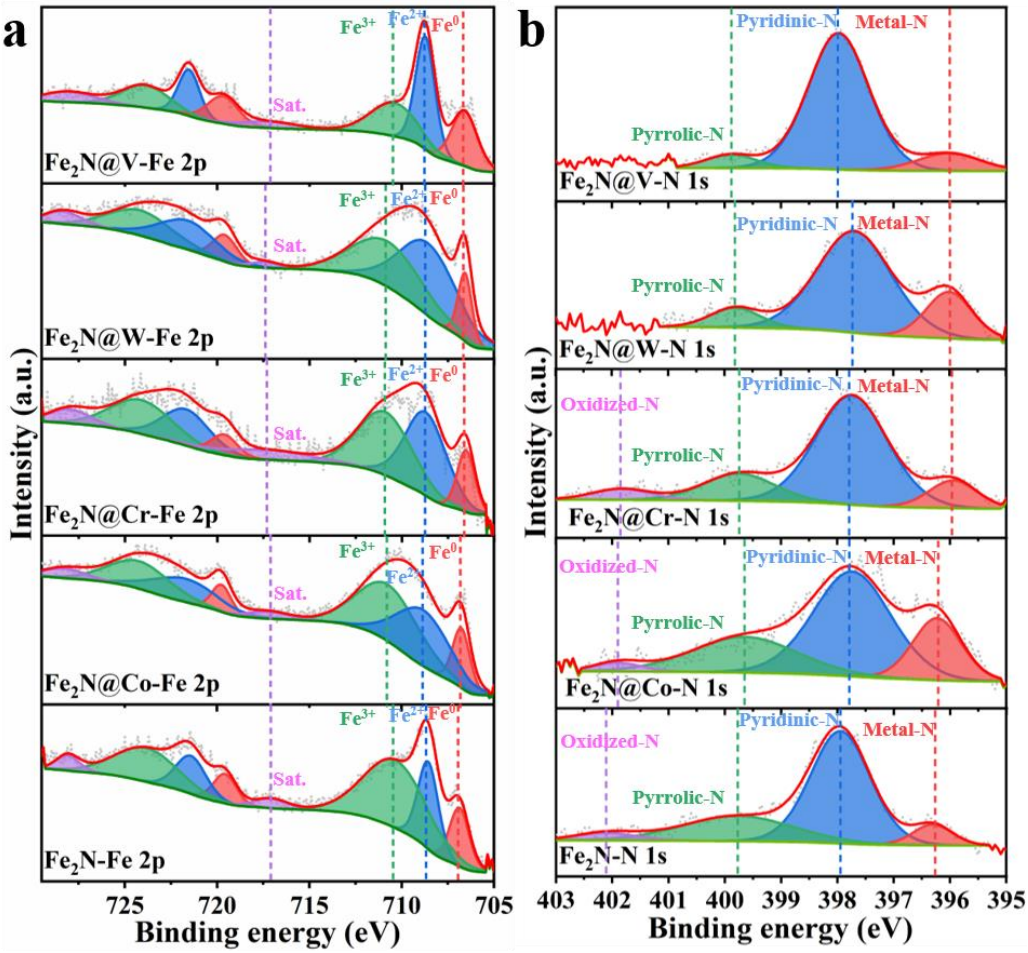

Figure 5.9 The high-resolution XPS spectra for (a) Fe 2p and (b) N 1s of the series of doped Fe_2N samples.

The high-resolution XPS spectra have also depicted the orbitals of doping elements in

Figure 5.10. The dominant peaks of the Co-doped sample centered at 778.9 eV, 780.9 eV, 782.9 eV and 787.1 eV are ascribed as $2p_{3/2}$ of metallic Co^0, Co^{2+} and Co^{3+} coordinated to O or N ions and satellite peak and the satellite peak.[145] The Cr doped sample has shown two main peaks at 575.9 eV and 576.8 eV correspond to Cr-N $2p_{3/2}$ and Cr-O $2p_{3/2}$.[248] The W doped sample has exhibited three divided peaks at 33.0 eV, 35.2 eV and 37.3 eV, which are assigned to different valence states of W-N $4f_{7/2}$ of different valence states as well as W-C $4f_{7/2}$ on the surface.[309] The sample with doping V has two peaks at 516.6 eV and 524.0 eV, which are corresponding to V-N $2p_{3/2}$ and V-N $2p_{1/2}$.[146] These results indicate that the doping element atoms usually existing in the crystal lattice on the surface by forming bonds with nitrogen ions.

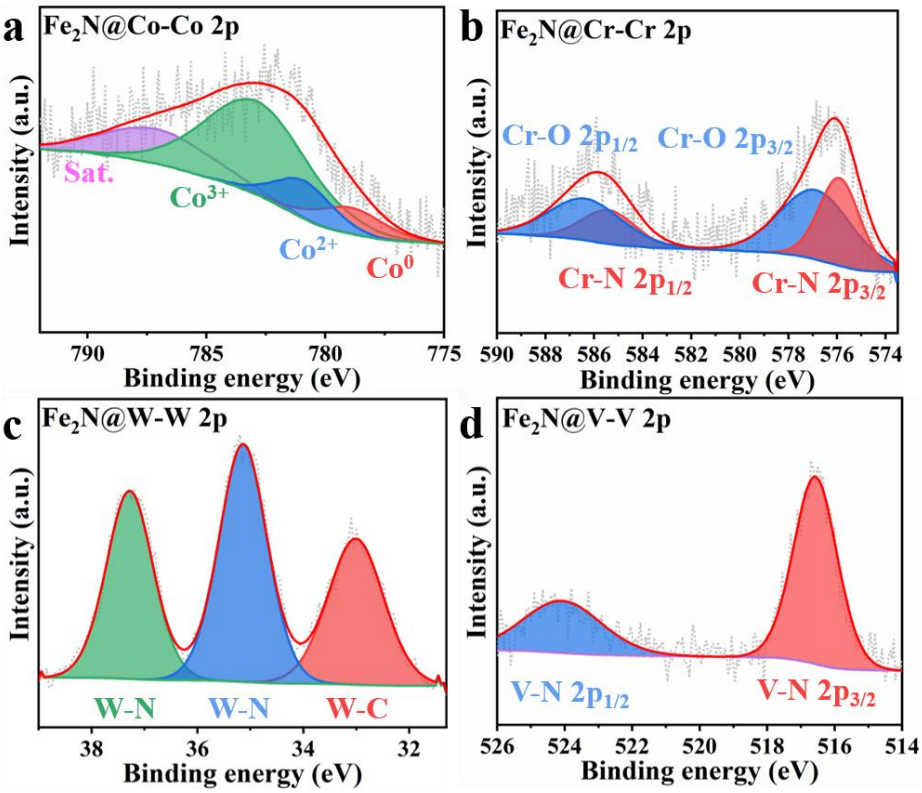

Figure 5.10 The high-resolution XPS spectra for (a) Co 2p, (b) Cr 2p, (c) W 4f and (d) V 2p of the series of doped Fe_2N samples.

The actual atomic concentrations of each element in doped Fe_2N samples have also been tested by XPS characterization. It is obvious that all the actual element doping ratios are much lower than the default ratio (5 at%) in the experimental condition. The element of the highest atomic doping ratio is Co, which contains 2.82 at% of that of its doped Fe_2N sample. The element with the lowest doping ratio is V, which only contains 0.12 at% of that of the doped sample. The doping ratio of W is also under 1 at%. Thus, these results have demonstrated the obscure color distributions of W and V images observed by TEM elemental mapping. The reason that leads to the difference of ratio under the same setting condition may be due to the metal salts used in precursor synthesis. The Co and Cr doping samples used compounds of nitrate, while W and V doping samples using tungstate salt and metavanadate salt. Thus, W and V elements are more difficult to dissociate and dope into the crystal lattice.

5.2.2 Piezoelectric catalytic H_2 evolution activity and electrochemical characterization

The piezoelectric catalytic activity of the series of as-prepared Fe_2N samples has been examined by measuring the H_2 evolution. As shown in **Figure 5.11a**, the H_2 evolution rates of different types of element doped Fe_2N (doping ratio of 5 at%) sample are all higher than that of the pure Fe_2N sample. The Co-doped Fe_2N has exhibited the highest activity of 122.8 μmol $g^{-1}h^{-1}$. The reason is that a notable difference of radius among various metal atoms would lead to the lattice expansion when they are doped, and the

piezoelectric performance has been improved.[310] Simultaneously, the crystal integrity of the doped catalyst would not be destroyed. In addition, the doped metal atoms are favorable to replace the subsurface atoms and downshift the d-band center of Fe_2N, which will be demonstrated by DFT calculation in the following section.[146]

Table 5.3 The actual atomic concentrations of each element in the doped Fe_2N samples synthesized by the default experimental condition of 5 at% doping.

Atomic Concentration %					
Fe_2N-Co5%	Fe 2p	O 1s	N 1s	C 1s	**Co 2p**
	6.86	26.5	8.08	55.74	**2.82**
Fe_2N-Cr5%	Fe 2p	O 1s	N 1s	C 1s	**Cr 2p**
	4.54	23.78	8.23	61.97	**1.48**
Fe_2N-W5%	Fe 2p	O 1s	N 1s	C 1s	**W 2p**
	4.91	24.19	5.89	64.16	**0.85**
Fe_2N-V5%	Fe 2p	O 1s	N 1s	C 1s	**V 2p**
	3.47	19	8.89	68.52	**0.12**

The activity subsequence of different doped samples from high to low level has been ordered as Co, Cr, W and V, which is in accordance with the doping ratio in **Table 5.3**. This means the doping ratio also plays an important role in affecting the piezoelectric catalytic performance. For deeply exploring the effect of doping ratio for the catalytic activity, the Co (2.5 at%) and V (15 at%) doped Fe_2N have been tested for comparison

(**Figure 5.11b**). Consequently, they have exhibited the performances of 247.9 and 244.4 μmol $g^{-1}h^{-1}$, which are much higher than that of the samples with the 5 at% doping ratios. This result means that the lower setting doping ratio of Co and the higher setting doping ratio of V can considerably improve the activity of the doped Fe_2N catalyst. This is because the actual doping ratios of Co (2.5%) doped and V (15%) doped samples are closer to the optimal doping ratio than that of 5% doped samples. When the doping ratio is lower than the optimal condition (the V doping sample), the polarization-induced surface charge will not be promoted sufficiently, so the separation and transfer of charge carriers are limited.[310] On the contrary, the excess dopant (the Co doping sample) may lead to the forming of defects, which could act as charge recombination centers in doped catalyst and lower the catalytic activity.[16,310]

Figure 5.11c has illustrated the effect of maintaining the cubic morphology of Co-doped Fe_2N. It can be found that the piezoelectric catalytic activity of the cubic sample is much higher than that of the nanoparticle sample, which was synthesized by long-term nitridation. This is due to the retaining porous structure derived from MOF precursor, which has a large specific surface area and more active sites during the reaction process. This result is in accordance with the previous chapter. The influence of the output power of the ultrasound source is also explored in **Figure 5.11d**. The catalytic performance shows an almost increasing linear trend along with the rise of the ultrasonic source output power, which demonstrates the necessity of ultrasound energy in this reaction. This also confirms the discussion of previous literature.[10]

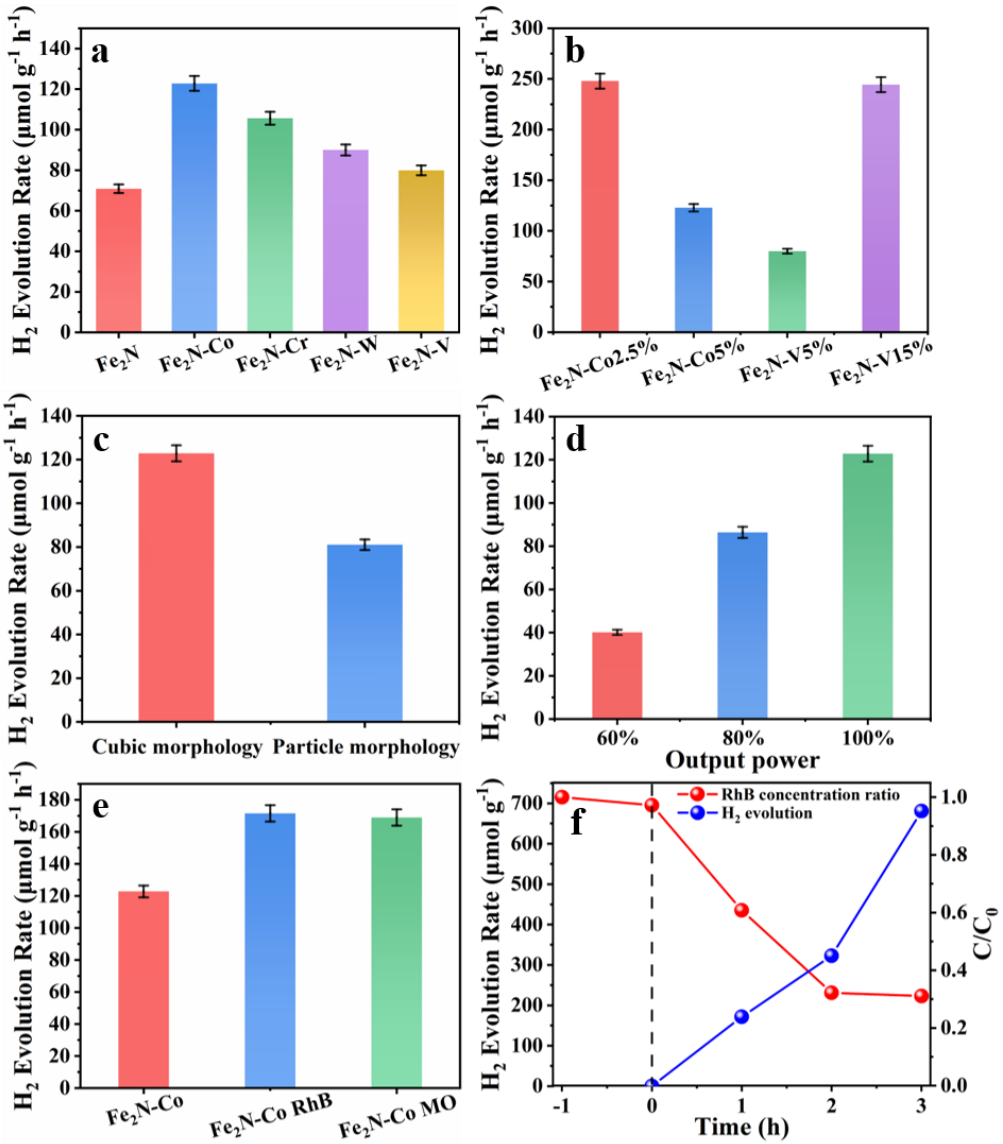

Figure 5.11 The piezoelectric H_2 generation of (a) pure Fe_2N and Co, Cr, W, V (5 at%) doped Fe_2N, (b) Co (2.5 at%) and V (15 at%) doped Fe_2N, (c) Co-doped Fe_2N of cube-like and nanoparticle morphology, (d) Co-doped Fe_2N under the conditions of the different output power of the ultrasonic source, (e) Co-doped Fe_2N with 5 ppm dye solution of RhB and MO, and (f) different continuing time (1, 2, 3 h) with 5 ppm RhB solution with the relative concentration ratios C/C_0 for the degradation of RhB before and after reaction with Co-doped Fe_2N.

Moreover, the doped Fe_2N also has the ability to degrade dye in the solution. The dyes including RhB and MO of 5 ppm concentration have been utilized for testing the degradation activity of these doped samples. Simultaneously, the H_2 evolution performance of samples in the solution containing dye has also been tested. According to the results in **Figure 5.11e**, the H_2 evolution rates of samples in these types of dye solution have been enhanced. The highest one is that the sample in the RhB solution which offers the rate of 171.5 μmol $g^{-1}h^{-1}$.

Then, this reaction system with RhB solution has been continued for 2 more hours. The H_2 production grows with a rapidly rising trend as the reaction is timing. The accumulated H_2 amount achieved is 681.1 μmol g^{-1} after 3 h of operation (**Figure 5.11f**). The UV-Vis absorption spectra before and after different times of dye degradation and H_2 evolution reactions have been tested. It is obvious that the UV-Vis absorbance of each dye solution shows lower peaks than that of the initial solution, and the peaks become much lower after the reaction of longer timing. **Figure 5.11f** has also shown the relative degradation ratios C/C_0, where C_0 is the initial concentration of dyes and the C is the decomposed dyes concentration at different reaction times. After the adsorption equilibrium, the concentration only decreases about 2.8%, which means the dye decomposing is mainly due to the degradation. After 3 hours of degradation, about 70% of the dye has been decomposed. This means the doped Fe_2N has a considerable activity of dye degradation. The results mentioned above demonstrate that the reactions

of H_2 production and dye degradation have supplementary effects on each other. The mechanism would be demonstrated below.

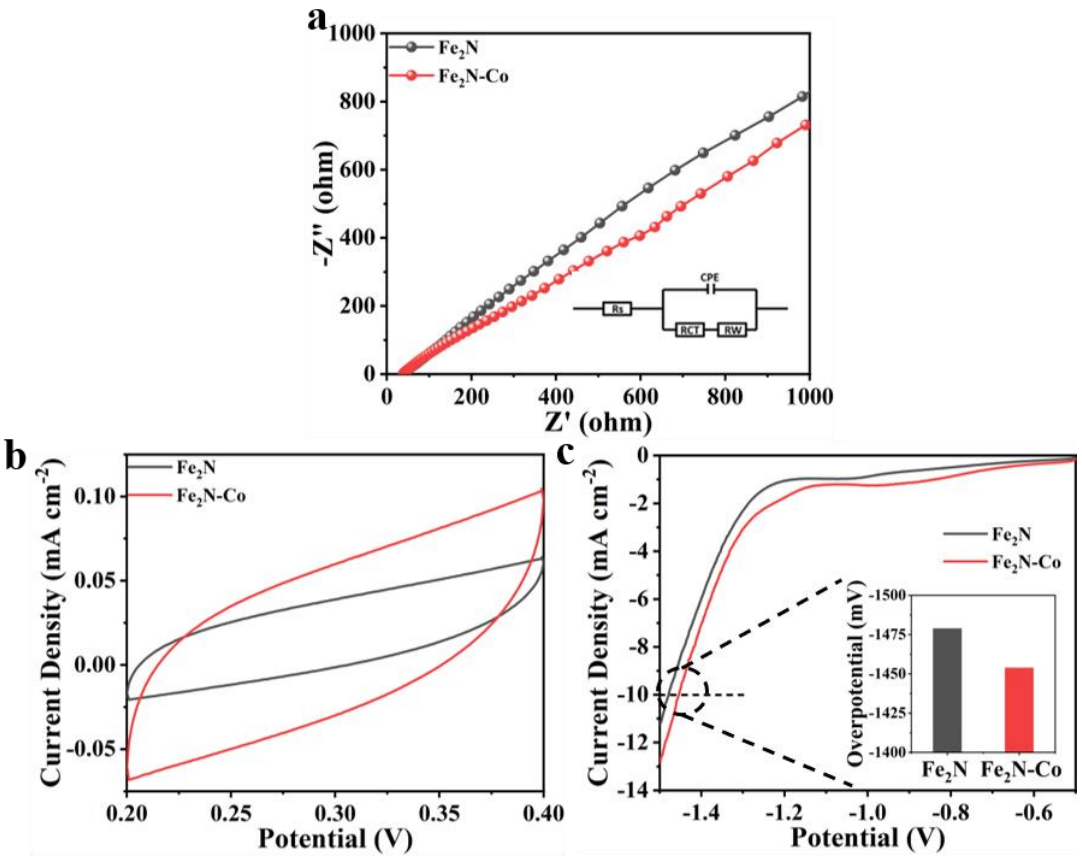

Figure 5.12 (a) The EIS Nyquist plots, (b) specific capacitance performances and (c) polarization curves of pure Fe_2N and Co-doped Fe_2N samples.

The electrochemical tests have been carried out to investigate the role of doped elements on the catalytic activity of Fe_2N. As **Figure 5.12a** has shown, the sample of Fe_2N@Co has a smaller arc than that of the Fe_2N sample, which means the R_{ct} is smaller. This indicates that the efficiency of charge transfer of Fe_2N@Co is better, which would facilitate the reaction process.[145] For the specific capacitance performance, **Figure**

5.12b has illustrated that the sample of Fe_2N-Co with a larger enclosed loop area has better electron storage ability than the pure sample.[145] In addition, the polarization curves in **Figure 5.12c** reveals a higher current density for the doped sample than the pure sample. The overpotential of Fe_2N-Co (-1454 mV) is lower than that (-1479 mV) of the pure sample at the current density of 10 mA cm^{-2}. This indicates that the Fe_2N-Co sample has an enhanced charge transfer kinetics by the doped structure.[311] These results have proved that these electrochemical properties of the doped sample are beneficial for the piezoelectric catalytic process.

5.2.3 Theoretical calculation and photocatalytic mechanism

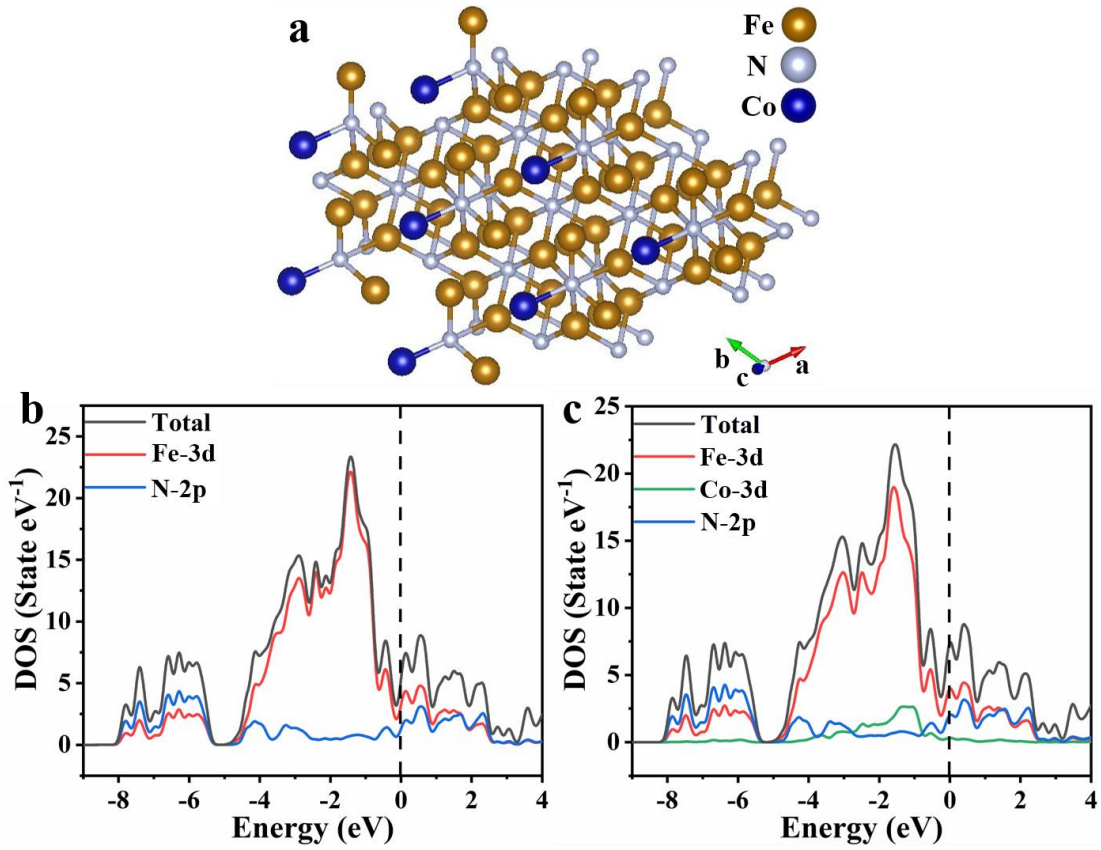

Figure 5.13 The atomic structure model of (a) Co-doped Fe_2N. Calculated electronic DOS of (b) pure Fe_2N and (c) Co-doped Fe_2N. The Fermi level is set to zero.

DFT calculations are carried out to further demonstrate the intrinsic effect of element dopants on the H_2 evolution rate of Fe_2N. **Figure 5.13a** has shown that the doped Co atoms have replaced some of the Fe atoms of Fe_2N-(001) surface. This indicates the metallic nature of all samples as a result of the existence of free electrons near the Fermi level.[145,260,312] In addition, there is an increased population of d states of Co near the Fermi level in the energy range between -3 to 0. The d-band center of Co-doped Fe_2N is -2.648 eV, which is downshifted compared to that (-2.596 eV) of the pure Fe_2N. It seems that the introduction of Co elements results in a change in the DOS near the Fermi level associated with the d states. According to the previous report, the contraction of the d-band and the downshifting of the d-band center would result in weakening of the interaction between the catalysts and absorbates. This is expected to contribute to the H_2 evolution performance.[146,302]

Based on the above results and the corresponding literature, the mechanism of piezoelectric catalytic hydrogen evolution in pure water or dye solution has been demonstrated below. Under the condition of ultrasonic vibration, the doped Fe_2N nanocubes are streamed and stressed by both vertical and lateral force. Thus, a piezoelectric potential is created on the surface of the cubes because of the piezoelectric effect. The electrons and holes are separated and transferred to the surface of the catalyst. Subsequently, the surficial doped metal elements can promote the transfer of an electron to the catalyst-solution interfaces and provide additional active sites for the redox

reactions. The procedure includes the reduction of H^+ by electrons for H_2 evolution, the reduction of O_2 by electrons for producing hydroxyl radicals (•OH) and oxygen radicals ($•O_2^-$), as well as the oxidation of H_2O by holes for producing •OH and H^+. Finally, the produced •OH and $•O_2^-$ are consumed by the dye molecules.[91,313,314]

In this process, the excited holes are efficiently consumed by the radical reaction, which not only leads to the degradation of dye but also limits the recombination between electrons and holes. Therefore, the H_2 evolution rate under the condition of dye solution is superior to that under the pure water condition. These reactions can be described as follows:

$$Piezocatalyst \xrightarrow{vibration} e^- + h^+$$

$$2H^+ + e^- \rightarrow H_2$$

$$O_2 + e^- \rightarrow \cdot O_2^-$$

$$\cdot O_2^- + e^- + 2H^+ \rightarrow H_2O_2$$

$$H_2O_2 \rightarrow 2 \cdot OH$$

$$H_2O + h^+ \rightarrow \cdot OH + H^+$$

$$Dye + \cdot OH / \cdot O_2^- \rightarrow Degradation$$

These proposed mechanisms for piezoelectric H_2 evolution while processing dye degradation is also suitable for other types of dyes.

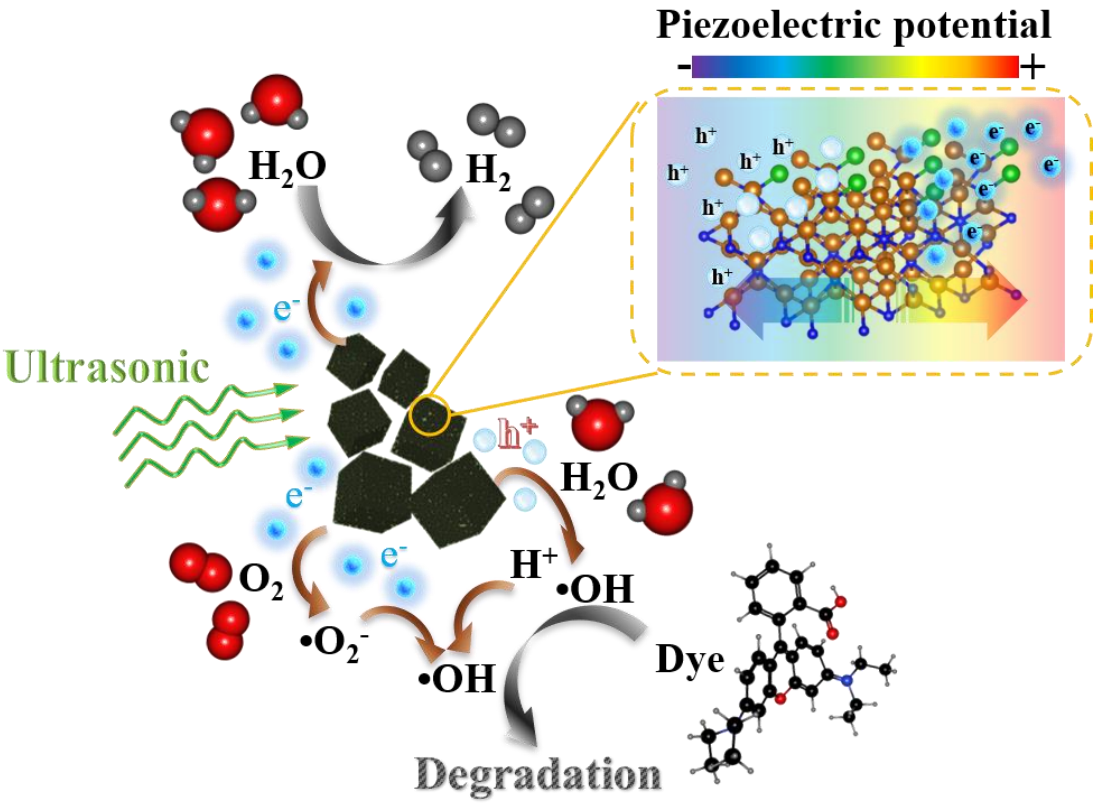

Figure 5.14 Proposed piezoelectric catalytic hydrogen production mechanism over the doped Fe_2N in a dye solution.

5.3 Conclusions

In conclusion, a series of MOF-derived Fe_2N with different doped elements (Co, Cr, W and V) have been synthesized successfully by the rapid-nitridation method and used for H_2 evolution by piezoelectric catalysis. The produced nanocubes with maintaining morphology from the MOF precursor have clearly been observed and characterized. The highest H_2 evolution rate is achieved by Co (5 at%) doped Fe_2N under the same ratio of doping (122.8 μmol $g^{-1}h^{-1}$), while every doped Fe_2N sample has a higher rate than that of the pure one. This highlights the advantages associated with the doping strategy.

Moreover, the Co and V doped sample with different doping ratios (2.5 and 15 at%, respectively) has gained much higher activity (247.9 and 244.4 μmol $g^{-1}h^{-1}$), which indicates that the doping ratio plays an important role in the piezoelectric catalytic process. In addition, the nanocubic sample has a better efficiency than that of the nanoparticle sample, which means the necessity of the rapid-nitridation method for keeping morphology. With the action of dye degradation, the process of piezoelectric H_2 production has been promoted. Finally, the DFT calculation has proved the d-band shift of Fe_2N and demonstrated the correctness of this strategy. These results provide a new strategy for the synthesis and tuning band gap of TMN with maintenance of morphology to offer the high-efficiency avenue for piezoelectric H_2 evolution.

Chapter 6

Conclusions and Perspective

6.1 Conclusions

This thesis aimed to systematically investigate new synthesis methodology and produce TMNs with ideal nanostructure and morphology. Then, these TMNs are applied in H_2 evolution catalytic reactions, including photocatalysis and piezoelectric catalysis. The results show that the mesoporous materials and MOF-derived TMNs are successfully synthesized. These samples have ordered mesoporous structure that is obtained through rapid-nitridation. In addition, the Fe_2N nanocubes can achieve a considerable H_2 production efficiency in the reactions of dye sensitization and degradation by photocatalysis and piezoelectric catalysis, respectively. Finally, the DFT calculation has elucidated for the improvement of catalytic performance. The details are listed below:

(1) A novel hard-template-based rapid-nitridation process has been explored. A series of ordered mesoporous TMN materials namely CoN, WN, CrN and Ni_3FeN are successfully synthesized within 30 min using a rather modest (in comparison with most ammono thermal processes) temperature range of 330-800°C. Utilization of (i) ordered porous precursors, (ii) pre-heating and (iii) pre-passing the ammonia for rapid-nitridation process is proved to be the key factors for efficiently shortening the nitridation and suppressing the closure or collapse of the mesoporous structures of TMNs materials. These results indicate that the template-based rapid-nitridation approach for the synthesis of mesoporous nitrides is indeed an effective method of generating catalysts in a rapid and readily scalable manner. Meanwhile, the universality of this method has been

proved, which means that various types of nitrides are suitable to be synthesized through this process. Hence this work paves way for a promising way to produce ordered mesoporous nitrides for a wide range of applications. This part of the work is mainly focusing on synthesis. Actually, the electrochemical properties of these mesoporous nitrides, such as OER activity, have been proved as highly efficient.

(2) Based on the synthesis method explored in **chapter 3**, as well as applying a more convenient template precursor, a kind of MOF derived porous Fe_2N has been synthesized using a two-step process, oxidation followed by the rapid-nitridation technique. MOF based on PB, which is made from a supramolecular assembly of iron components with N-containing organic ligands, has been employed. Usage of this MOF ensures that the nitride samples retain the shape of the precursor while showing only a nominal shrinkage during the chemical transformation (hence indicating a topotactic transformation). The preparation process is both quick and rather chimie douce (soft chemical). Fe_2N samples thus obtained have a high specific surface area, and offer abundant exposed active sites for photocatalytic activity. Fe_2N is sensitized using EY for boosting photocatalytic hydrogen evolution. Hydrogen production rates close to ~14.5 mmol $g^{-1}h^{-1}$ are observed, which is considered desirable. The superior conductivity of Fe_2N offers enhanced electron transfer performance between the catalyst and photosensitizer, so that the reduction reaction can be processed faster. Meanwhile, the separated reaction sites of dye degradation by the electron donor of the

sacrificial agent and the electron capture by the Fe_2N catalyst also limit the electron-hole recombination, hence yielding the observed high hydrogen production rates. Calculations show that free electrons in Fe_2N, responsible for its metallic-like properties, arise primarily because of Fe-3d. Overall, this work provides a new means of producing MOF derived TMN materials, which in conjunction with suitable dyes, offer high-efficiency and low-cost avenues for making photocatalysts for hydrogen production.

(3) Depend on the reaction route of **chapter 4**, a series of MOF-derived Fe_2N with different doped elements (Co, Cr, W and V) have been synthesized successfully by the rapid-nitridation method and used for H_2 evolution by piezoelectric catalysis. The produced nanocubes with maintaining morphology from the MOF precursor have clearly been observed and characterized. The highest H_2 evolution rate is achieved by Co (5 at%) doped Fe_2N under the same ratio of doping (122.8 μmol $g^{-1}h^{-1}$), while every doped Fe_2N sample has a higher rate than that of the pure one. This highlights the advantageous effects of the doping strategy. Moreover, the Co and V doped sample with different doping ratios (2.5 and 15 at%, respectively) has gained much higher activity (247.9 and 244.4 μmol $g^{-1}h^{-1}$), which indicates that the doping ratio plays an important role in the piezoelectric catalytic process. In addition, the nanocubic sample has a higher efficiency than that of the nanoparticle sample, which means the necessity of the rapid-nitridation method for keeping morphology. With the action of dye degradation, the process of piezoelectric H_2 production has been promoted. Finally, the DFT calculation

has proved the d-band shift of Fe_2N and demonstrated the correctness of this strategy. These results provide a new strategy for the synthesis and tuning band gap of TMN with keeping morphology to offer the high-efficiency avenue for piezoelectric H_2 evolution.

6.2 Perspective

In recent years, photocatalysis has been rapidly developed and various types of photocatalysts have been synthesized. Different kinds of strategies for improving the activity and decreasing the charge carrier recombination rate have been explored, which contains ions doping, element substitution and application of cocatalysts. These methodologies have also gained considerable effects. Except for the way of tuning components, morphology is another significant factor that influences the catalytic efficiency. To synthesize materials with ideal nanostructure needs simple and efficient methods.

At present, the hard- and soft-template methods, as well as the in-situ templating pathway and tuning MOF derivation have sufficient potential to synthesize materials with expected morphology. The third way for improving the catalytic performance is to explore another unique principle during the process. The piezoelectric catalyst is a new strategy to promote electron transfer by the effect of the in-built electric field as a result of squeezed or stretched. This kind of new technology could be utilized without the dependence on a specific energy source because mechanical energy such as vibration,

noise and fluid flow are surrounding the environment all the time. In addition, the considerable energy conversion efficiency (reported as 78% previously) of the piezoelectric reaction process has been regarded as an attractive advantage for exploration. The published literature clearly shows the advantages and practical application of piezoelectric catalysts. This shows the prospects of piezoelectric catalysis.

This thesis provides a new synthesis strategy for TMNs, which has the universality of application and simplicity of operation. This strategy can efficiently maintain the morphology of synthesized materials avoiding the collapse of the nanostructure. However, the control of conditions still needs to be improved due to the particular operation process. It is important to keep the detail operation unity for achieving the efficiency of this synthesized strategy. By the method of rapid-nitridation, a kind of MOF-derived Fe_2N has been synthesized using nanocubic morphology.

This type of TMN can gain a distinct H_2 evolution activity in dye sensitization reaction. However, the performance still has the possibility to be improved. For example, other types of MOF precursors can be chosen and more modifications on the surface of the materials are desirable. In deeper exploration, this kind of Fe_2N has been doped by a series of elements and used for piezoelectric H_2 evolution. The piezoelectric effect of TMN has been proved and the strategy of doping has been supported. However, the stability of this type of piezocatalyst needs to be improved further; the deeper principles during the piezoelectric process are also required to be explored. The solution to these

problems would considerably enhance the performance and the prospects of piezoelectric catalysts.

References

[1] J. Ran, J. Zhang, J. Yu, M. Jaroniec, et al. Earth-abundant cocatalysts for semiconductor-based photocatalytic water splitting. *Chem. Soc. Rev.* **2014,** 43, 7787–7812.

[2] W. Wang, X. Xu, W. Zhou, Z. Shao. Recent progress in metal-organic frameworks for applications in electrocatalytic and photocatalytic water splitting. *Adv. Sci.* **2017,** 4, 1600371.

[3] M.R. Shaner, H.A. Atwater, N.S. Lewis, E.W. McFarland. A comparative technoeconomic analysis of renewable hydrogen production using solar energy. *Energy Environ. Sci.* **2016,** 9, 2354.

[4] X. Li, J. Yu, J. Low, Y. Fang, et al. Engineering heterogeneous semiconductors for solar water splitting solar water splitting. *J. Mater. Chem. A Mater. Energy Sustain.* **2015,** 3, 2485–2534.

[5] S. Zhu, D. Wang. Photocatalysis: Basic principles, diverse forms of implementations and emerging scientific opportunities. *Adv. Energy Mater.* **2017,** 7, 1700841.

[6] J.C. Colmenares, R. Luque. Heterogeneous photocatalytic nanomaterials prospects and challenges in selective transformations of biomass-derived compounds. *Chem. Soc. Rev.* **2014,** 43, 765–778.

[7] J.C. Colmenares, R. Luque, J.M. Campelo, F. Colmenares, et al. Nanostructured photocatalysts and their applications in the photocatalytic transformation of lignocellulosic biomass: An overview. *Materials.* **2009,** 2, 2228–2258.

[8] Y. Qu, X. Duan. Progress, challenge and perspective of heterogeneous photocatalysts. *Chem. Soc. Rev.* **2013,** 42, 2568–2580.

[9] N. Han, P. Liu, J. Jiang, L. Ai, et al. Recent advances in nanostructured metal nitrides for water splitting. *J. Mater. Chem. A.* **2018,** 6, 19912–19933.

[10] Z. Liang, C.-F. Yan, S. Rtimi, J. Bandara. Piezoelectric materials for catalytic/photocatalytic removal of pollutants: Recent advances and outlook. *Appl. Catal. B Environ.* **2019,** 241, 256–269.

[11] J. Zhang, Y. Wu, M. Xing, S.A.K. Leghari, et al. Development of modified N doped TiO_2 photocatalyst with metals, nonmetals and metal oxides. *Energy Environ. Sci.* **2010,** 3, 715–726.

[12] K. Iwashina, A. Iwase, Y.H. Ng, R. Amal, et al. Z-schematic water splitting into H_2 and O_2 using metal sulfide as a hydrogen-evolving photocatalyst and reduced graphene oxide as a solid-state electron mediator. *J. Am. Chem. Soc.* **2015,** 137, 604–607.

[13] W. Wang, M.O. Tadé, Z. Shao. Nitrogen-doped simple and complex oxides for photocatalysis: A review. *Prog. Mater. Sci.* **2018,** 92, 33–63.

[14] X. Wang, K. Maeda, A. Thomas, K. Takanabe, et al. A metal-free polymeric photocatalyst for hydrogen production from water under visible light. *Nat. Mater.* **2009,** 8, 76–80.

[15] J. Qiu, X. Zhang, Y. Feng, X. Zhang, et al. Modified metal-organic frameworks as photocatalysts. *Appl. Catal. B Environ.* **2018,** 231, 317–342.

[16] S. Tu, Y. Guo, Y. Zhang, C. Hu, et al. Piezocatalysis and piezo-photocatalysis: Catalysts classification and modification strategy, reaction mechanism, and practical application. *Adv. Funct. Mater.* **2020,** 30, 2005158.

[17] M.M. Sullivan, C.J. Chen, A. Bhan. Catalytic deoxygenation on transition metal carbide catalysts. *Catal. Sci. Technol.* **2016,** 6, 602–616.

[18] M. Zhang, S. Zhao, Z. Zhao, S. Li, et al. Piezocatalytic effect induced hydrogen production from water over non-noble metal Ni deposited ultralong GaN nanowires. *ACS Appl. Mater. Interfaces*. **2021,** 13, 10916–10924.

[19] W. Feng, J. Yuan, L. Zhang, W. Hu, et al. Atomically thin ZnS nanosheets: Facile synthesis and superior piezocatalytic H_2 production from pure H_2O. *Appl. Catal. B Environ.* **2020,** 277, 119250.

[20] A. Kudo, Y. Miseki. Heterogeneous photocatalyst materials for water splitting. *Chem. Soc. Rev.* **2009,** 38, 253–278.

[21] A. Fujishima, K. Honda. Electrochemical photolysis of water at a semiconductor electrode. *Nature*. **1972,** 238, 37–38.

[22] D.M. Schultz, T.P. Yoon. Solar synthesis: Prospects in visible light photocatalysis. *Science*. **2014,** 343, 1239176.

[23] X. Chen, A. Selloni. Introduction: Titanium dioxide (TiO_2) nanomaterials. *Chem. Rev.* **2014,** 114, 9281–9282.

[24] G. Liu, H.G. Yang, J. Pan, Y.Q. Yang, et al. Titanium dioxide crystals with tailored facets. *Chem. Rev.* **2014,** 114, 9559–9612.

[25] R. Asahi, T. Morikawa, T. Ohwaki, K. Aoki, et al. Visible-light photocatalysis in nitrogen-doped titanium oxides. *Science*. **2001,** 293, 269–271.

[26] H. Zhang, X. Lv, Y. Li, Y. Wang, et al. P25-graphene composite as a high performance photocatalyst. *ACS Nano*. **2010,** 4, 380–386.

[27] S.C. Yan, Z.S. Li, Z.G. Zou. Photodegradation performance of g-C_3N_4 fabricated by directly heating melamine. *Langmuir*. **2009,** 25, 10397–10401.

[28] F. Dong, Z. Zhao, T. Xiong, Z. Ni, et al. In situ construction of g-C_3N_4/g-C_3N_4 metal-free heterojunction for enhanced visible-light photocatalysis. *ACS Appl. Mater. Interfaces*. **2013,** 5, 11392–11401.

[29] S. Cao, J. Low, J. Yu, M. Jaroniec. Polymeric photocatalysts based on graphitic carbon nitride. *Adv. Mater.* **2015,** 27, 2150–2176.

[30] X. Meng, W. Qi, W. Kuang, S. Adimi, et al. Chromium-titanium nitride as efficient co-catalyst for photocatalytic hydrogen production. *J. Mater. Chem. A.* **2020,** 8, 15774–15781.

[31] B. Weng, Y. Xu. What if the electrical conductivity of graphene is significantly deteriorated for the graphene-semiconductor composite-based photocatalysis? *Appl. Mater. Interfaces*. **2015,** 7, 27948–27958.

[32] Y. Liu, L. Fang, H. Lu, L. Liu, et al. Highly effcient and stable Ag/Ag_3PO_4 plasmonic photocatalyst in visible light. *Catal. Commun.* **2012,** 17, 200–204.

[33] H. Wang, Y. Bai, J. Yang, X. Lang, et al. A facile way to rejuvenate Ag_3PO_4 as a recyclable highly efficient photocatalyst. *Chem. A Eur. J.* **2012,** 18, 5524–5529.

[34] Y. Wang, R. Shi, J. Lin, Y. Zhu. Enhancement of photocurrent and photocatalytic activity of ZnO hybridized with graphite-like C_3N_4. *Energy*

Environ. Sci. **2011,** 4, 2922–2929.

[35] S. Kumar, T. Surendar, A. Baruah, V. Shanker. Synthesis of a novel and stable g-C_3N_4-Ag_3PO_4 hybrid nanocomposite photocatalyst and study of the photocatalytic activity under visible light irradiation. *J. Mater. Chem. A.* **2013,** 1, 5333–5340.

[36] Z. Zou, J. Ye, K. Sayama, H. Arakawa. Direct splitting of water under visible light irradiation with an oxide semiconductor photocatalyst. *Nature*. **2001,** 414, 625–627.

[37] W. Tu, Y. Zhou, Z. Zou. Photocatalytic conversion of CO_2 into renewable hydrocarbon fuels: State-of-the-Art accomplishment, challenges, and prospects. *Adv. Mater*. **2014,** 26, 4607–4626.

[38] P. Li, Y. Zhou, Z. Zhao, Q. Xu, et al. Hexahedron prism-anchored octahedronal CeO_2: Crystal facet-based homojunction promoting efficient solar fuel synthesis. *J. Am. Chem. Soc.* **2015,** 137, 9547–9550.

[39] C. Chen, W. Ma, J. Zhao. Semiconductor-mediated photodegradation of pollutants under visible-light irradiation. *Chem. Soc. Rev.* **2010,** 39, 4206–4219.

[40] L. Shen, L. Huang, S. Liang, R. Liang, et al. Electrostatically derived self-assembly of NH_2-mediated zirconium MOFs with graphene for photocatalytic reduction of Cr(vi). *RSC Adv.* **2014,** 4, 2546–2549.

[41] H. Chen, charith E. Nanayakkara, vicki H. Grassian. Titanium dioxide photocatalysis in atmospheric chemistry. *Chem. Rev.* **2012,** 112, 5919–5948.

[42] D. Zhu, Q. Zhou. Action and mechanism of semiconductor photocatalysis on degradation of organic pollutants in water treatment: A review. *Environ. Nanotechnology, Monit. Manag.* **2019,** 12, 100255.

[43] J.D. Bryan, D.R. Gamelin. Doped semiconductor nanocrystals: Synthesis, characterization, physical properties, and applications. *Prog. Inorg. Chem.* **2005,** 54, 47–126.

[44] H.J. Queisser, E.E. Haller. Defects in semiconductors: Some fatal, some vital. *Science*. **1998,** 281, 945–950.

[45] Y.C. Cao. Impurities enhance semiconductor nanocrystal performance. *Science*. **2011,** 332, 48–49.

[46] G. Liu, L. Wang, H.G. Yang, H.-M. Cheng, et al. Titania-based photocatalysts-crystal growth, doping and heterostructuring. *J. Mater. Chem.* **2010,** 20, 831–843.

[47] N. Serpone, A. V. Emeline. Semiconductor photocatalysis - past, present, and future outlook. *J. Phys. Chem. Lett.* **2012,** 3, 673–677.

[48] D. Mocatta, G. Cohen, J. Schattner, O. Millo, et al. Heavily doped semiconductor nanocrystal quantum dots. *Science*. **2011,** 332, 77–81.

[49] R.S. Ningthoujam, N.S. Gajbhiye. Synthesis, electron transport properties of transition metal nitrides and applications. *Prog. Mater. Sci.* **2015,** 70, 50–154.

[50] P. Zhang, J. Zhang, J. Gong. Tantalum-based semiconductors for solar water splitting. *Chem. Soc. Rev.* **2014,** 43, 4395–4422.

[51] I. Tsuji, H. Kato, A. Kudo. Visible-light-induced H_2 evolution from an aqueous solution containing sulfide and sulfite over a ZnS-$CuInS_2$-$AgInS_2$ solid-solution photocatalyst. *Angew. Chem. Int. Ed.* **2005,** 44, 3565–3568.

[52] Y. Sasaki, H. Kato, A. Kudo. $[Co(bpy)_3]^{(3+/2+)}$ and $[Co(phen)_3]^{(3+/2+)}$ electron mediators for overall water splitting under sunlight irradiation using Z-scheme photocatalyst system. *J. Am. Chem. Soc.* **2013,** 135, 5441–5449.

[53] F.N. Sayed, O.D. Jayakumar, R. Sasikala, R.M. Kadam, et al. Photochemical hydrogen generation using nitrogen-doped TiO_2-Pd nanoparticles: Facile synthesis and effect of Ti^{3+} incorporation. *J. Phys. Chem. C*. **2012,** 116, 12462–12467.

[54] J. Yu, L. Qi, M. Jaroniec. Hydrogen production by photocatalytic water splitting over Pt/TiO_2 nanosheets with exposed (001) facets. *J. Phys. Chem. C*. **2010,** 114, 13118–13125.

[55] H.-Y. Lin, H.-C. Yang, W.-L. Wang. Synthesis of mesoporous Nb_2O_5 photocatalysts with Pt, Au, Cu and NiO cocatalyst for water splitting. *Catal. Today*. **2011,** 174, 106–113.

[56] X. Fang, Q. Shang, Y. Wang, L. Jiao, et al. Single Pt atoms confined into a metal-organic framework for efficient photocatalysis. *Adv. Mater.* **2018,** 30, 1705112.

[57] P. Gao, J. Liu, S. Lee, T. Zhang, et al. High quality graphene oxide-CdS-Pt nanocomposites for efficient photocatalytic hydrogen evolution. *J. Mater. Chem.* **2012,** 22, 2292–2298.

[58] J. Sato, N. Saito, Y. Yamada, K. Maeda, et al. RuO_2-loaded β-Ge_3N_4 as a non-oxide photocatalyst for overall water splitting. *J. Am. Chem. Soc.* **2005,** 127, 4150–4151.

[59] K. Maeda, R. Abe, K. Domen. Role and function of ruthenium species as promoters with TaON-based photocatalysts for oxygen evolution in two-step water splitting under visible light. *J. Phys. Chem. C*. **2011,** 115, 3057–3064.

[60] W.J. Youngblood, S.-H.A. Lee, Y. Kobayashi, E.A. Hernandez-Pagan, et al. Photoassisted overall water splitting in a visible light-absorbing dye-sensitized photoelectrochemical cell. *J. Am. Chem. Soc.* **2009,** 131, 926–927.

[61] B. Ma, J. Yang, H. Han, J. Wang, et al. Enhancement of Photocatalytic Water oxidation activity on IrO_x−ZnO/$Zn_{2-x}GeO_{4-x-3y}N_{2y}$ catalyst with the solid solution phase junction. *J. Phys. Chem. C*. **2010,** 114, 12818–12822.

[62] K. Maeda, K. Teramura, D. Lu, T. Takata, et al. Photocatalyst releasing hydrogen from water. *Nature*. **2006,** 440, 295.

[63] K. Maeda, N. Sakamoto, T. Ikeda, H. Ohtsuka, et al. Preparation of core-shell-structured nanoparticles (with a noble-metal or metal oxide core and a chromia shell) and their application in water splitting by means of visible light. *Chem. A Eur. J.* **2010,** 16, 7750–7759.

[64] K. Maeda, K. Teramura, D. Lu, N. Saito, et al. Noble-metal/$Cr_{(2)}O_{(3)}$ core/shell nanoparticles as a cocatalyst for photocatalytic overall water splitting. *Angew. Chem. Int. Ed.* **2006,** 45, 7806–7809.

[65] L. Yu, B.Y. Xia, X. Wang, X.W. Lou. General formation of M-MoS_3 (M = Co, Ni) hollow structures with enhanced electrocatalytic activity for hydrogen evolution. *Adv. Mater.* **2016,** 28, 92–97.

[66] X. Xu, Y. Pan, W. Zhou, Y. Chen, et al. Toward enhanced oxygen evolution on perovskite oxides synthesized from different approaches: A case study of $Ba_{0.5}Sr_{0.5}Co_{0.8}Fe_{0.2}O_{3-\delta}$. *Electrochim. Acta*. **2016,** 219, 553–559.

[67] Z. Peng, D. Jia, A.M. Al-Enizi, A.A. Elzatahry, et al. From water oxidation to reduction: Homologous Ni-Co based nanowires as complementary water splitting electrocatalysts. *Adv. Energy Mater.* **2015,** 5, 1402031.

[68] D. Friebel, M.W. Louie, M. Bajdich, K.E. Sanwald, et al. Identification of highly active Fe sites in (Ni,Fe)OOH for electrocatalytic water splitting. *J. Am. Chem. Soc.* **2015,** 137, 1305–1313.

[69] X. Xu, C. Su, W. Zhou, Y. Zhu, et al. Co-doping strategy for developing perovskite oxides as highly efficient electrocatalysts for oxygen evolution reaction. *Adv. Sci.* **2016,** 3, 1500187.

[70] H. Wu, J. Geng, H. Ge, Z. Guo, et al. Egg-derived mesoporous carbon microspheres as bifunctional oxygen evolution and oxygen reduction electrocatalysts. *Adv. Energy Mater.* **2016,** 6, 1600794.

[71] Y. Liu, G. Yu, G. Li, Y. Sun, et al. Coupling Mo_2C with nitrogen-rich nanocarbon leads to efficient hydrogen-evolution electrocatalytic sites. *Angew. Chem. Int. Ed.* **2015,** 54, 10752–10757.

[72] S. Chen, T. Takata, K. Domen. Particulate photocatalysts for overall water splitting. *Nat. Rev. Mater.* **2017,** 2, 17050.

[73] M.G. Kibria, F.A. Chowdhury, S. Zhao, B. AlOtaibi, et al. Visible light-driven efficient overall water splitting using p-type metal-nitride nanowire arrays. *Nat. Commun.* **2015,** 6, 6797.

[74] Q. Wang, T. Hisatomi, Q. Jia, H. Tokudome, et al. Scalable water splitting on particulate photocatalyst sheets with a solar-to-hydrogen energy conversion efficiency exceeding 1. *Nat. Mater.* **2016,** 15, 611–615.

[75] Y. Hikita, K. Nishio, L.C. Seitz, P. Chakthranont, et al. Band edge engineering of oxide photoanodes for photoelectrochemical water splitting: Integration of subsurface dipoles with atomic-scale control. *Adv. Energy Mater.* **2016,** 6,

1502154.

[76] Y. Kuang, Q. Jia, G. Ma, T. Hisatomi, et al. Ultrastable low-bias water splitting photoanodes via photocorrosion inhibition and in situ catalyst regeneration. *Nat. Energy*. **2017,** 2, 16191.

[77] J. Li, N. Wu. Semiconductor-based photocatalysts and photoelectrochemical cells for solar fuel generation: A review. *Catal. Sci. Technol.* **2015,** 5, 1360–1384.

[78] T. Simon, M.T. Carlson, J.K. Stolarczyk, J. Feldmann. Electron transfer rate vs recombination losses in photocatalytic H_2 generation on Pt-decorated CdS nanorods. *ACS Energy Lett.* **2016,** 1, 1137–1142.

[79] T. Gershon, B. Shin, N. Bojarczuk, M. Hopstaken, et al. The role of sodium as a surfactant and suppressor of non-radiative recombination at internal surfaces in Cu_2ZnSnS_4. *Adv. Energy Mater.* **2015,** 5, 1400849.

[80] Z. Liang, R. Shen, Y.H. Ng, P. Zhang, et al. A review on 2D MoS_2 cocatalysts in photocatalytic H_2 production. *J. Mater. Sci. Technol.* **2020,** 56, 89–121.

[81] N. Xiao, S. Li, X. Li, L. Ge, et al. The roles and mechanism of cocatalysts in photocatalytic water splitting to produce hydrogen. *Chinese J. Catal.* **2020,** 41, 642–671.

[82] Z.L. Wang, J. Song. Piezoelectric nanogenerators based on zinc oxide nanowire arrays. *Science*. **2006,** 312, 242–246.

[83] L. Wang, S. Liu, Z. Wang, Y. Zhou, et al. Piezotronic effect enhanced photocatalysis in strained anisotropic ZnO/TiO_2 nanoplatelets via thermal stress. *ACS Nano*. **2016,** 10, 2636–2643.

[84] J. Wu, N. Qin, D. Bao. Effective enhancement of piezocatalytic activity of $BaTiO_3$ nanowires under ultrasonic vibration. *Nano Energy*. **2018,** 45, 44–51.

[85] H. You, Z. Wu, L. Zhang, Y. Ying, et al. Harvesting the vibration energy of $BiFeO_3$ nanosheets for hydrogen evolution. *Angew. Chem. Int. Ed.* **2019,** 58, 11779–11784.

[86] X. Xu, L. Xiao, Z. Wu, Y. Jia, et al. Harvesting vibration energy to piezo-

catalytically generate hydrogen through Bi_2WO_6 layered-perovskite. *Nano Energy*. **2020,** 78, 105351.

[87] T.-M. Chou, S.-W. Chan, Y.-J. Lin, P.-K. Yang, et al. A highly efficient Au-MoS_2 nanocatalyst for tunable piezocatalytic and photocatalytic water disinfection. *Nano Energy*. **2019,** 57, 14–21.

[88] M.-H. Wu, J.-T. Lee, Y.J. Chung, M. Srinivaas, et al. Ultrahigh efficient degradation activity of single- and few-layered $MoSe_2$ nanoflowers in dark by piezo-catalyst effect. *Nano Energy*. **2017,** 40, 369–375.

[89] Y.-C. Wang, J.M. Wu. Effect of controlled oxygen vacancy on H_2-production through the piezocatalysis and piezophototronics of ferroelectric R3C $ZnSnO_3$ nanowires. *Adv. Funct. Mater*. **2020,** 30, 1907619.

[90] D. Yu, Z. Liu, J. Zhang, S. Li, et al. Enhanced catalytic performance by multi-field coupling in $KNbO_3$ nanostructures: Piezo-photocatalytic and ferro-photoelectrochemical effects. *Nano Energy*. **2019,** 58, 695–705.

[91] C. Yu, M. Tan, Y. Li, C. Liu, et al. Ultrahigh piezocatalytic capability in eco-friendly $BaTiO_3$ nanosheets promoted by 2D morphology engineering. *J. Colloid Interface Sci.* **2021,** 596, 288–296.

[92] J.M. Wu, W.E. Chang, Y.T. Chang, C.-K. Chang. Piezo-catalytic effect on the enhancement of the ultra-high degradation activity in the dark by single- and few- layers MoS_2 nanoflowers. *Adv. Mater.* **2016,** 28, 3718–3725.

[93] X. Ning, A. Hao, Y. Cao, J. Hu, et al. Effective promoting piezocatalytic property of zinc oxide for degradation of organic pollutants and insight into piezocatalytic mechanism. *J. Colloid Interface Sci.* **2020,** 577, 290–299.

[94] Y. Su, L. Zhang, W. Wang, X. Li, et al. Enhanced H_2 evolution based on ultrasound-assisted piezo-catalysis of modified MoS_2. *J. Mater. Chem. A.* **2018,** 6, 11909–11915.

[95] F. Chen, H. Huang, L. Guo, Y. Zhang, et al. The role of polarization in photocatalysis. *Angew. Chem. Int. Ed.* **2019,** 58, 10061–10073.

[96] S. Li, Z. Zhao, J. Zhao, Z. Zhang, et al. Recent advances of ferro-, piezo-, and

pyroelectric nanomaterials for catalytic applications. *ACS Appl. Nano Mater.* **2020,** 3, 1063–1079.

[97] X. Wang, G.S. Rohrer, H. Li. Piezotronic modulations in electro- and photochemical catalysis. *MRS Bull.* **2018,** 43, 946–951.

[98] M.B. Starr, X. Wang. Coupling of piezoelectric effect with electrochemical processes. *Nano Energy*. **2015,** 14, 296–311.

[99] W.J. Chun, A. Ishikawa, H. Fujisawa, T. Takata, et al. Conduction and valence band positions of Ta_2O_5, TaON, and Ta_3N_5 by UPS and electrochemical methods. *J. Phys. Chem. B.* **2003,** 107, 1798–1803.

[100] K. Maeda, K. Domen. New non-oxide photocatalysts designed for overall water splitting under visible light. *J. Phys. Chem. C.* **2007,** 111, 7851–7861.

[101] M.G. Kibria, Z. Mi. Artificial photosynthesis using metal/nonmetal-nitride semiconductors: current status, prospects, and challenges. *J. Mater. Chem. A.* **2016,** 4, 2801–2820.

[102] D. Barman, S. Paul, S. Ghosh, S.K. De. Cu_3N nanocrystals decorated with Au nanoparticles for photocatalytic degradation of organic dyes. *ACS Appl. Nano Mater*. **2019,** 2, 5009–5019.

[103] A. Zakutayev, C.M. Caskey, A.N. Fioretti, D.S. Ginley, et al. Defect tolerant semiconductors for solar energy conversion. *J. Phys. Chem. Lett.* **2014,** 5, 1117–1125.

[104] Y. Wu, P. Lazic, G. Hautier, K. Persson, et al. First principles high throughput screening of oxynitrides for water-splitting photocatalysts. *Energy Environ. Sci.* **2013,** 6, 157–168.

[105] T. Suda, K. Kakishita. Band-gap energy and electron effective mass of polycrystalline Zn_3N_2. *J. Appl. Phys.* **2006,** 99, 076101.

[106] A.H. Jayatissa, T. Wen. Microstructure and optical properties of zinc nitride films deposited by magnetron sputtering method. *Surf. Coatings Technol.* **2012,** 211, 163–166.

[107] D.E. Partin, D.J. Williams, M. O'Keeffe. The crystal structures of Mg_3N_2 and

Zn_3N_2. *J. Solid State Chem.* **1997,** 132, 56–59.

[108] Y.L. Wang, T. Nie, Y.H. Li, X.L. Wang, et al. Black tungsten nitride as a metallic photocatalyst for overall water splitting operable at up to 765 nm. *Angew. Chem. Int. Ed.* **2017,** 56, 7430–7434.

[109] L. Liang, X. Li, J. Zhang, P. Ling, et al. Efficient infrared light induced CO_2 reduction with nearly 100% CO selectivity enabled by metallic CoN porous atomic layers. *Nano Energy*. **2020,** 69, 104421.

[110] W. Huang, Y. Gao, J. Wang, P. Ding, et al. Plasmonic enhanced reactive oxygen species activation on low-work-function tungsten nitride for direct near-infrared driven photocatalysis. *Small*. **2020,** 16, 2004557.

[111] Y. Zhang, S. He, W. Guo, Y. Hu, et al. Surface-plasmon-driven hot electron photochemistry. *Chem. Rev.* **2018,** 118, 2927–2954.

[112] N.T. Nguyen, T. Yan, L. Wang, J.Y.Y. Loh, et al. Plasmonic titanium nitride facilitates indium oxide CO_2 photocatalysis. *Small*. **2020,** 16, 2005754.

[113] J.E. Houston, G.E. Laramore, R.L. Park. Surface electronic properties of tungsten, tungsten carbide, and platinum. *Science*. **1974,** 185, 258–260.

[114] S. Dong, X. Chen, X. Zhang, G. Cui. Nanostructured transition metal nitrides for energy storage and fuel cells. *Coord. Chem. Rev.* **2013,** 257, 1946–1956.

[115] Y. Xiao, J.Y. Hwang, Y.K. Sun. Transition metal carbide-based materials: synthesis and applications in electrochemical energy storage. *J. Mater. Chem. A.* **2016,** 4, 10379–10393.

[116] W. Qi, Y. Zhou, S. Liu, H. Liu, et al. Oxidized impurity in transition metal nitride for improving the hydrogen evolution efficiency of transition metal nitride-based catalyst. *Appl. Mater. Today*. **2020,** 18, 100476.

[117] Z. Wang, Y. Inoue, T. Hisatomi, R. Ishikawa, et al. Overall water splitting by Ta_3N_5 nanorod single crystals grown on the edges of $KTaO_3$ particles. *Nat. Catal.* **2018,** 1, 756–763.

[118] Y. He, P. Ma, S. Zhu, M. Liu, et al. Photo-induced performance enhancement of tantalum nitride for solar water oxidation. *Joule*. **2017,** 1, 831–842.

[119] X. Hou, S. Jiang, Y.Y. Li, J. Xiao, et al. Ni-doped InN/GaZnON composite catalyst for overall water splitting under visible light irradiation. *Int. J. Hydrogen Energy*. **2015,** 40, 15448–15453.

[120] M. Ebaid, J.W. Min, C. Zhao, T.K. Ng, et al. Water splitting to hydrogen over epitaxially grown InGaN nanowires on a metallic titanium/silicon template: reduced interfacial transfer resistance and improved stability to hydrogen. *J. Mater. Chem. A.* **2018,** 6, 6922–6930.

[121] X. Zhou, E.M. Zolnhofer, N.T. Nguyen, N. Liu, et al. Stable Co-catalyst-free photocatalytic H_2 evolution from oxidized titanium nitride nanopowders. *Angew. Chem. Int. Ed.* **2015,** 54, 13385–13389.

[122] W. Qi, S. Liu, F. Li, H. Jiang, et al. Prussian blue derived Fe_2N for efficiently improving the photocatalytic hydrogen evolution activity of g-C_3N_4 nanosheets. *Catal. Sci. Technol.* **2019,** 9, 2571–2577.

[123] H. Chen, D. Jiang, Z. Sun, R.M. Irfan, et al. Cobalt nitride as an efficient cocatalyst on CdS nanorods for enhanced photocatalytic hydrogen production in water. *Catal. Sci. Technol.* **2017,** 7, 1515–1522.

[124] L. Chen, H. Huang, Y. Zheng, W. Sun, et al. Noble-metal-free Ni_3N/g-C_3N_4 photocatalysts with enhanced hydrogen production under visible light irradiation. *Dalt. Trans.* **2018,** 47, 12188–12196.

[125] Z. Sun, H. Chen, L. Zhang, D. Lu, et al. Enhanced photocatalytic H_2 production on cadmium sulfide photocatalysts using nickel nitride as a novel cocatalyst. *J. Mater. Chem. A.* **2016,** 4, 13289–13295.

[126] K. Xia, Z. Chen, J. Yi, H. Xu, et al. Highly efficient visible-light-driven schottky catalyst MoN/2D g-C_3N_4 for hydrogen production and organic pollutants degradation. *Ind. Eng. Chem. Res.* **2018,** 57, 8863–8870.

[127] B. Ma, J. Zhang, K. Lin, D. Li, et al. Improved photocatalytic hydrogen evolution of CdS using earth-abundant cocatalyst Mo_2N with rod shape and large capacitance. *ACS Sustain. Chem. Eng.* **2019,** 7, 13569–13575.

[128] L. Tian, S. Min, F. Wang, Z. Zhang. Metallic vanadium nitride as a noble-metal-

free cocatalyst efficiently catalyzes photocatalytic hydrogen production with CdS nanoparticles under visible light irradiation. *J. Phys. Chem. C*. **2019,** 123, 28640–28650.

[129] B. Weng, M.Y. Qi, C. Han, Z.R. Tang, et al. Photocorrosion inhibition of semiconductor-based photocatalysts: Basic principle, current development, and future perspective. *ACS Catal.* **2019,** 9, 4642–4687.

[130] M. Xiao, B. Luo, M. Lyu, S. Wang, et al. Single-crystalline nanomesh tantalum nitride photocatalyst with improved hydrogen-evolving performance. *Adv. Energy Mater.* **2018,** 8, 1701605.

[131] T. Hisatomi, M. Otani, K. Nakajima, K. Teramura, et al. Preparation of crystallized mesoporous Ta_3N_5 assisted by chemical vapor deposition of tetramethyl orthosilicate. *Chem. Mater.* **2010,** 22, 3854–3861.

[132] S.S.K. Ma, T. Hisatomi, K. Maeda, Y. Moriya, et al. Enhanced water oxidation on Ta_3N_5 photocatalysts by modification with alkaline metal salts. *J. Am. Chem. Soc*. **2012,** 134, 19993–19996.

[133] L. Yuliati, J.-H. Yang, X. Wang, K. Maeda, et al. Highly active tantalum(v) nitridenanoparticles prepared from a mesoporous carbon nitride template for photocatalytic hydrogen evolution under visible light irradiation. *J. Mater. Chem.* **2010,** 20, 4295–4298.

[134] T.D.C. Nguyen, T.P.L.C. Nguyen, H.T.T. Mai, V.-D. Dao, et al. Novel photocatalytic conversion of CO_2 by vanadium-doped tantalum nitride for valuable solar fuel production. *J. Catal.* **2017,** 352, 67–74.

[135] N. Yamada, K. Maruya, Y. Yamaguchi, X. Cao, et al. p- to n-type conversion and nonmetal-metal transition of lithium-inserted Cu_3N films. *Chem. Mater.* **2015,** 27, 8076–8083.

[136] C.M. Caskey, R.M. Richards, D.S. Ginley, A. Zakutayev. Thin film synthesis and properties of copper nitride, a metastable semiconductor. *Mater. Horizons*. **2014,** 1, 424–430.

[137] K. Maeda, K. Teramura, N. Saito, Y. Inoue, et al. Photocatalytic overall water

splitting on gallium nitride powder. *Bull. Chem. Soc. Jpn.* **2007,** 80, 1004–1010.

[138] S.P. Phivilay, C.A. Roberts, A.A. Puretzky, K. Domen, et al. Fundamental bulk/surface structure-photoactivity relationships of supported ($Rh_{2-y}Cr_yO_3$)/GaN photocatalysts. *J. Phys. Chem. Lett.* **2013,** 4, 3719–3724.

[139] T. Ohno, L. Bai, T. Hisatomi, K. Maeda, et al. Photocatalytic water splitting using modified GaN:ZnO solid solution under visible light: Long-time operation and regeneration of activity. *J. Am. Chem. Soc.* **2012,** 134, 8254–8259.

[140] J. Wu. When group-III nitrides go infrared: New properties and perspectives. *J. Appl. Phys.* **2009,** 106, 5.

[141] S. Arafin, X. Liu, Z. Mi. Review of recent progress of III-nitride nanowire lasers. *J. Nanophotonics*. **2013,** 7, 074599.

[142] M.G. Kibria, H.P.T. Nguyen, K. Cui, S. Zhao, et al. One-step overall water splitting under visible light using multiband InGaN/GaN nanowire heterostructures. *ACS Nano*. **2013,** 7, 7886–7893.

[143] Z. Jin, T. Wei, L. Li, F. Li, et al. Loading Co_3N nanoparticles as efficient cocatalysts over $Zn_{0.5}Cd_{0.5}S$ for enhanced H_2 evolution under visible light. *Dalt. Trans.* **2019,** 48, 2676–2682.

[144] J. Di, C. Chen, C. Zhu, P. Song, et al. Cobalt nitride as a novel cocatalyst to boost photocatalytic CO_2 reduction. *Nano Energy*. **2021,** 79, 105429.

[145] S. Liu, X. Meng, S. Adimi, H. Guo, et al. Efficient photocatalytic hydrogen evolution over carbon supported antiperovskite cobalt zinc nitride. *Chem. Eng. J.* **2021,** 408, 127307.

[146] Z. Chen, Y. Song, J. Cai, X. Zheng, et al. Tailoring the d-band centers enables Co_4N nanosheets to be highly active for hydrogen evolution catalysis. *Angew. Chem. Int. Ed.* **2018,** 57, 5076–5080.

[147] X. Meng, W. Kuang, W. Qi, Z. Cheng, et al. Ultra-low loading of Au clusters on nickel nitride efficiently boosts photocatalytic hydrogen production with titanium dioxide. *ChemCatChem*. **2020,** 12, 2752–2759.

[148] C. Wang, W. Qi, Y. Zhou, W. Kuang, et al. Ni-Mo ternary nitrides based one-

dimensional hierarchical structures for efficient hydrogen evolution. *Chem. Eng. J.* **2020,** 381, 122611.

[149] B. Ma, X. Wang, K. Lin, J. Li, et al. A novel ultraefficient non-noble metal composite cocatalyst Mo_2N/Mo_2C/graphene for enhanced photocatalytic H_2 evolution. *Int. J. Hydrogen Energy*. **2017,** 42, 18977–18984.

[150] B. Ma, D. Li, X. Wang, K. Lin. Molybdenum-based Co-catalysts in photocatalytic hydrogen production: Categories, structures, and roles. *ChemSusChem*. **2018,** 11, 3871–3881.

[151] J. Ran, H. Wang, H. Jin, C. Ling, et al. Metallic MoN ultrathin nanosheets boosting high performance photocatalytic H_2 production. *J. Mater. Chem. A.* **2018,** 6, 23278–23282.

[152] S. Gong, Z.J. Jiang, P. Shi, J. Fan, et al. Noble-metal-free heterostructure for efficient hydrogen evolution in visible region: Molybdenum nitride/ultrathin graphitic carbon nitride. *Appl. Catal. B Environ.* **2018,** 238, 318–327.

[153] B. Ma, Y. Liu, J. Li, K. Lin, et al. Mo_2N: An efficient non-noble metal cocatalyst on CdS for enhanced photocatalytic H_2 evolution under visible light irradiation. *Int. J. Hydrogen Energy*. **2016,** 41, 22009–22016.

[154] L. Chen, C. Liu, Z. Zhang. Novel [111] oriented γ-Mo_2N thin films deposited by magnetron sputtering as an anode for aqueous micro-supercapacitors. *Electrochim. Acta*. **2017,** 245, 237–248.

[155] Y. Qu, N. Sun, M. Humayun, A. Zada, et al. Improved visible-light activities of nanocrystalline CdS by coupling with ultrafine NbN with lattice matching for hydrogen evolution. *Sustain. Energy Fuels*. **2018,** 2, 549–552.

[156] Y. Guo, H. Zhu, Q. Wang. Piezoelectric effects in surface-engineered two-dimensional group III nitrides. *ACS Appl. Mater. Interfaces*. **2019,** 11, 1033–1039.

[157] W. Xia, A. Mahmood, R. Zou, Q. Xu. Metal-organic frameworks and their derived nanostructures for electrochemical energy storage and conversion. *Energy Environ. Sci.* **2015,** 8, 1837–1866.

[158] Y. Wang, D. Liu, Z. Liu, C. Xie, et al. Porous cobalt-iron nitride nanowires as excellent bifunctional electrocatalysts for overall water splitting. *Chem. Commun.* **2016,** 52, 12614–12617.

[159] L. Lux, K. Williams, S. Ma. Heat-treatment of metal-organic frameworks for green energy applications. *CrystEngComm*. **2015,** 17, 10–22.

[160] B. Zhu, R. Zou, Q. Xu. Metal-organic framework based catalysts for hydrogen evolution. *Adv. Energy Mater.* **2018,** 1801193, 1–33.

[161] H. bin Wu, B. yu Xia, L. Yu, X. Yu, et al. Porous molybdenum carbide nano-octahedrons synthesized via confined carburization in metal-organic frameworks for efficient hydrogen production. *Nat. Commun.* **2015,** 6, 6512.

[162] H. Furukawa, K.E. Cordova, M. O'Keeffe, O.M. Yaghi. The chemistry and applications of metal-organic frameworks. *Science*. **2013,** 341, 1230444.

[163] R.J. Kuppler, D.J. Timmons, Q.R. Fang, J.R. Li, et al. Potential applications of metal-organic frameworks. *Coord. Chem. Rev.* **2009,** 253, 3042–3066.

[164] S.L. James. Metal-organic frameworks. *Chem. Soc. Rev.* **2003,** 32, 276–288.

[165] A. Saad, H. Shen, Z. Cheng, R. Arbi, et al. Mesoporous ternary nitrides of earth-abundant metals as oxygen evolution electrocatalyst. *Nano-Micro Lett.* **2020,** 12, 79.

[166] A. Saad, Z. Cheng, X. Zhang, S. Liu, et al. Ordered mesoporous cobalt-nickel nitride prepared by nanocasting for oxygen evolution reaction electrocatalysis. *Adv. Mater. Interfaces*. **2019,** 6, 1900960.

[167] L. Pan, T. Muhammad, L. Ma, Z.-F. Huang, et al. MOF-derived C-doped ZnO prepared via a two-step calcination for efficient photocatalysis. *Appl. Catal. B Environ.* **2016,** 189, 181–191.

[168] J.-D. Xiao, H.-L. Jiang. Thermally stable metal-organic framework-templated synthesis of hierarchically porous metal sulfides: Enhanced photocatalytic hydrogen production. *Small*. **2017,** 13, 1700632.

[169] Y. Lv, W. Zhan, Y. He, Y. Wang, et al. MOF-templated synthesis of porous Co_3O_4 concave nanocubes with high specific surface area and their gas sensing

properties. *ACS Appl. Mater. Interfaces*. **2014,** 6, 4186–4195.

[170] J.L.C. Rowsell, O.M. Yaghi. Metal-organic frameworks: a new class of porous materials. *Microporous Mesoporous Mater.* **2004,** 73, 3–14.

[171] D.J. Tranchemontagne, J.L. Mendoza-Cortes, M. O'Keeffe, O.M. Yaghi. Secondary building units, nets and bonding in the chemistry of metal-organic frameworks. *Chem. Soc. Rev.* **2009,** 38, 1257–1283.

[172] T. Toyao, M. Fujiwaki, K. Miyahara, T.-H. Kim, et al. Design of zeolitic imidazolate framework derived nitrogen-doped nanoporous carbons containing metal species for carbon dioxide fixation reactions. *ChemSusChem*. **2015,** 8, 3905–3912.

[173] X. Kang, H. Liu, M. Hou, X. Sun, et al. Synthesis of supported ultrafine non-noble subnanometer-scale metal particles derived from metal-organic frameworks as highly efficient heterogeneous catalysts. *Angew. Chem. Int. Ed.* **2016,** 55, 1080–1084.

[174] Y. Xu, X. Lv, Y. Chen, W. Fu. Highly selective reduction of nitroarenes to anilines catalyzed using MOF-derived hollow Co_3S_4 in water under ambient conditions. *Catal. Commun.* **2017,** 101, 31–35.

[175] H. Liu, S. Zhang, Y. Liu, Z. Yang, et al. Well-dispersed and size-controlled supported metal oxide nanoparticles derived from MOF composites and further application in catalysis. *Small*. **2015,** 11, 3130–3134.

[176] W. Zhong, H. Liu, C. Bai, S. Liao, et al. Base-free oxidation of alcohols to esters at room temperature and atmospheric conditions using nanoscale Co-based catalysts. *ACS Catal.* **2015,** 5, 1850–1856.

[177] Y. Chen, R. Zhang, L. Jiao, H. Jiang. Metal-organic framework-derived porous materials for catalysis. *Coord. Chem. Rev.* **2018,** 362, 1–23.

[178] D.D. Vaughn, J. Araujo, P. Meduri, J.F. Callejas, et al. Solution synthesis of Cu_3PdN nanocrystals as ternary metal nitride electrocatalysts for the oxygen reduction reaction. *Chem. Mater.* **2014,** 26, 6226–6232.

[179] Y. Zhu, G. Chen, X. Xu, G. Yang, et al. Enhancing electrocatalytic activity for

hydrogen evolution by strongly coupled molybdenum nitride@nitrogen-doped carbon porous nano octahedrons. *ACS Catal.* **2017,** 7, 3540–3547.

[180] M.S. Balogun, W. Qiu, W. Wang, P. Fang, et al. Recent advances in metal nitrides as high-performance electrode materials for energy storage devices. *J. Mater. Chem. A.* **2015,** 3, 1364–1387.

[181] W. Li, C.Y. Cao, C.Q. Chen, Y. Zhao, et al. Fabrication of nanostructured metal nitrides with tailored composition and morphology. *Chem. Commun.* **2011,** 47, 3619–3621.

[182] S. Fu, C. Zhu, J. Song, M.H. Engelhard, et al. Highly ordered mesoporous bimetallic phosphides as efficient oxygen evolution electrocatalysts. *ACS Energy Lett.* **2016,** 1, 792–796.

[183] R.K.C.D. Lima, M.S. Batista, M. Wallau, E.A. Sanches, et al. High specific surface area LaFeCo perovskites-synthesis by nanocasting and catalytic behavior in the reduction of NO with CO. *Appl. Catal. B Environ.* **2009,** 90, 441–450.

[184] L. Jin, B. Liu, Y. Wu, S. Thanneeru, et al. Synthesis of mesoporous CoS_2 and $Ni_xCo_{1-x}S_2$ with superior supercapacitive performance using a facile solid-Phase sulfurization. *ACS Appl. Mater. Interfaces*. **2017,** 9, 36837–36848.

[185] Y. Shi, Y. Wan, R. Zhang, D. Zhao, et al. Synthesis of self-supported ordered mesoporous cobalt and chromium nitrides. *Adv. Funct. Mater.* **2008,** 18, 2436–2443.

[186] G. Jiang, H. Han, W. Zhuang, X. Xu, et al. Three-dimensional ordered mesoporous cobalt nitride for fast-kinetics and stable-cycling lithium storage. *J. Mater. Chem. A.* **2019,** 7, 17561–17569.

[187] J. Lai, B. Huang, Y. Chao, X. Chen, et al. Strongly coupled nickel-cobalt nitrides/carbon hybrid nanocages with Pt-like activity for hydrogen evolution catalysis. *Adv. Mater.* **2019,** 31, 1805541.

[188] H. Wang, J. Li, K. Li, Y. Lin, et al. Transition metal nitrides for electrochemical energy applications. *Chem. Soc. Rev.* **2021,** 50, 1354–1390.

[189] Z. Chen, Y. Ha, Y. Liu, H. Wang, et al. In situ formation of cobalt

nitrides/graphitic carbon composites as efficient bifunctional electrocatalysts for overall water splitting. *ACS Appl. Mater. Interfaces*. **2018,** 10, 7134–7144.

[190] Y. Yuan, J. Wang, S. Adimi, H. Shen, et al. Zirconium nitride catalysts surpass platinum for oxygen reduction. *Nat. Mater.* **2020,** 19, 282–286.

[191] V. Molinari, C. Giordano, M. Antonietti, D. Esposito. Titanium nitride-nickel nanocomposite as heterogeneous catalyst for the hydrogenolysis of aryl ethers. *J. Am. Chem. Soc.* **2014,** 136, 1758–1761.

[192] L. Ma, L.R.L. Ting, V. Molinari, C. Giordano, et al. Efficient hydrogen evolution reaction catalyzed by molybdenum carbide and molybdenum nitride nanocatalysts synthesized via the urea glass route. *J. Mater. Chem. A.* **2015,** 3, 8361–8368.

[193] C. Defilippi, D. V. Shinde, Z. Dang, L. Manna, et al. HfN nanoparticles: An unexplored catalyst for the electrocatalytic oxygen evolution reaction research. *Angew. Chem. Int. Ed.* **2019,** 58, 15464–15470.

[194] C.P. Jiménez-Gómez, C. Defilippi, J.A. Cecilia, R. Moreno-Tost, et al. The role of nitride species in the gas-phase furfural hydrogenation activity of supported nickel catalysts. *Mol. Catal.* **2020,** 487, 110889.

[195] J.S.J. Hargreaves. Heterogeneous catalysis with metal nitrides. *Coord. Chem. Rev.* **2013,** 257, 2015–2031.

[196] J.S. Kang, M.A. Park, J.Y. Kim, S.H. Park, et al. Reactively sputtered nickel nitride as electrocatalytic counter electrode for dye- and quantum dot-sensitized solar cells. *Sci. Rep.* **2015,** 5, 10450.

[197] M.E. Kreider, A. Gallo, S. Back, Y. Liu, et al. Precious metal-free nickel nitride catalyst for the oxygen reduction reaction. *ACS Appl. Mater. Interfaces*. **2019,** 11, 26863–26871.

[198] A.P. Murthy, D. Govindarajan, J. Theerthagiri, J. Madhavan, et al. Metal-doped molybdenum nitride films for enhanced hydrogen evolution in near-neutral strongly buffered aerobic media. *Electrochim. Acta*. **2018,** 283, 1525–1533.

[199] P.J. McGinn. Thin-film processing routes for combinatorial materials

investigations - A review. *ACS Comb. Sci.* **2019,** 21, 501–515.

[200] Y. Han, X. Yue, Y. Jin, X. Huang, et al. Hydrogen evolution reaction in acidic media on single-crystalline titanium nitride nanowires as an efficient non-noble metal electrocatalyst. *J. Mater. Chem. A.* **2016,** 4, 3673–3677.

[201] L. Huang, Z. Hu, H. Jin, J. Wu, et al. Salt-assisted synthesis of 2D materials. *Adv. Funct. Mater.* **2020,** 30, 1908486.

[202] P. Urbankowski, B. Anasori, T. Makaryan, D. Er, et al. Synthesis of two-dimensional titanium nitride Ti_4N_3 (MXene). *Nanoscale*. **2016,** 8, 11385–11391.

[203] H. Jin, Q. Gu, B. Chen, C. Tang, et al. Molten salt-directed catalytic synthesis of 2D layered transition-metal nitrides for efficient hydrogen evolution. *Chem.* **2020,** 6, 2382–2394.

[204] M. Shalom, V. Molinari, D. Esposito, G. Clavel, et al. Sponge-like nickel and nickel nitride structures for catalytic applications. *Adv. Mater.* **2014,** 26, 1272–1276.

[205] J. Xie, S. Li, X. Zhang, J. Zhang, et al. Atomically-thin molybdenum nitride nanosheets with exposed active surface sites for efficient hydrogen evolution. *Chem. Sci.* **2014,** 5, 4615–4620.

[206] H. Wu, W. Chen. Copper nitride nanocubes: size-controlled synthesis and application as cathode catalyst in alkaline fuel cells. *J. Am. Chem. Soc.* **2011,** 133, 15236–15239.

[207] Y. Zhang, B. Ouyang, J. Xu, G. Jia, et al. Rapid synthesis of cobalt nitride nanowires: Highly efficient and low-cost catalysts for oxygen evolution. *Angew. Chem. Int. Ed.* **2016,** 128, 8812–8816.

[208] W.W. Chen, K. Sasaki, C. Ma, A.I. Frenkel, et al. Hydrogen-evolution catalysts based on non-noble metal nickel-molybdenum nitride nanosheets. *Angew. Chem. Int. Ed.* **2012,** 51, 6131–6135.

[209] A.M. Alexander, J.S.J. Hargreaves, C. Mitchell. The reduction of various nitrides under hydrogen: Ni_3N, Cu_3N, Zn_3N_2 and Ta_3N_5. *Top. Catal.* **2012,** 55, 1046–1053.

[210] R. Michalsky, A.M. Avram, B.A. Peterson, P.H. Pfromm, et al. Chemical looping of metal nitride catalysts: low-pressure ammonia synthesis for energy storage. *Chem. Sci.* **2015,** 6, 3965–3974.

[211] C.G. Morales-Guio, L.-A. Stern, X. Hu. Nanostructured hydrotreating catalysts for electrochemical hydrogen evolution. *Chem. Soc. Rev.* **2014,** 43, 6555.

[212] W.F. Chen, J.T. Muckerman, E. Fujita. Recent developments in transition metal carbides and nitrides as hydrogen evolution electrocatalysts. *ChemComm*. **2013,** 49, 8896–8909.

[213] R. Fang, R. Luque, Y. Li. Efficient one-pot fructose to DFF conversion using sulfonated magnetically separable MOF-derived Fe_3O_4 (111) catalysts. *Green Chem.* **2017,** 19, 647–655.

[214] M. Lan, R. Guo, Y. Dou, J. Zhou, et al. Fabrication of porous Pt-doping heterojunctions by using bimetallic MOF template for photocatalytic hydrogen generation. *Nano Energy*. **2017,** 33, 238–246.

[215] D. Zhao, J. Feng, Q. Huo, N. Melosh, et al. Triblock copolymer syntheses of mesoporous silica with periodic 50 to 300 angstrom pores. *Science*. **1998,** 279, 548–552.

[216] X. Deng, K. Chen, H. Tüysüz. A protocol for the nanocasting method: Preparation of ordered mesoporous metal oxides. *Chem. Mater.* **2016,** 29, 40–52.

[217] B.E. Warren. X-ray diffraction, Courier Corporation, .

[218] M. Yang. Synthesis and physical properties study on mixed metal oxynitrides.

[219] J.I. Goldtein, D.E. Newbury, J.R. Michael, N.W. Ritchie, et al. Scanning electron microscopy and X-ray microanalysis, Springer, .

[220] Drives and positioning systems for electron microscopes. *Mono Spektra*. (n.d.) https://www.monospektra.com/positioning/applicatio.

[221] M.E. Hayat. Basic techniques for transmission electron microscopy, Elsevier, .

[222] N. Rijal. Electron microscope: Principle, types, and applications. *Microbe Online*. **2020,** https://microbeonline.com/electron-microscope-prin.

[223] H.-H. Perkampus. UV-VIS spectroscopy and its applications, Springer Science

\& Business Media, .

[224] O. Scherf-Clavel. Impurity profiling of challenging active pharmaceutical ingredients without chromophore.

[225] T.L. Barr. Modern ESCA The principles and practice of X-Ray photoelectron spectroscopy, CRC press, .

[226] J. Segui. Differentially pumped vacuum systems for spectroscopic imaging. *COMSOL*. **2014,** https://www.comsol.com/blogs/differentially-pumped.

[227] M. Naderi. Chapter fourteen-surface area: Brunauer-Emmett-Teller (BET), in: Prog. Filtr. Sep., : pp. 585–608.

[228] Y.S. Choudhary, L. Jothi, G. Nageswaran. Chapter 2 - Electrochemical characterization, in: Spectrosc. Methods Nanomater. Charact., : pp. 19–54.

[229] H. Chengguo, H. Yutong. Principles of linear sweep voltammetry and interpretations of voltammograms. *Univ. Chem.* **2021,** 36, 2005071.

[230] D. Damborska, P. Kasak, J. Tkac. Glycoprofiling of cancer biomarkers: Label-free electrochemical lectin-based biosensors. *Open Chem.* **2015,** 13, 636–655.

[231] P. Giannozzi, S. Baroni, N. Bonini, M. Calandra, et al. Quantum Espresso: a modular and open-source software project for quantum simulations of materials. *J. Phys. Condens. Matter*. **2009,** 21, 395502.

[232] J.D. Head, M.C. Zerner. A Broyden-Fletcher-Goldfarb-Shanno optimization procedure for molecular geometries. *Chem. Phys. Lett.* **1985,** 122, 264–270.

[233] G. Kresse, D. Joubert. From ultrasoft pseudopotentials to the projector augmented-wave method. *Phys. Rev. B.* **1999,** 59, 1758.

[234] H. Xin, A. Vojvodic, J. Voss, J.K. Nørskov, et al. Effects of d-band shape on the surface reactivity of transition-metal alloys. *Phys. Rev. B.* **2014,** 89, 115114.

[235] B. Hammer, J.K. Nørskov. Electronic factors determining the reactivity of metal surfaces. *Surf. Sci.* **1995,** 343, 211–220.

[236] C.A. Mackliet. Diffusion of iron, cobalt, and nickel. *Phys. Rev. B.* **1958,** 109, 1964–1970.

[237] H. Asteman, J. Svensson, L. Johansson. Evidence for chromium evaporation

influencing the oxidation of 304L: The effect of temperature and flow rate. *Oxid. Met.* **2002,** 57, 193–216.

[238] G. Ehrlich, F.G. Hudda. Atomic view of surface self-diffusion: tungsten on tungsten. *J. Chem. Phys.* **1966,** 44, 1039–1049.

[239] E. Rossinyol, J. Arbiol, F. Peiró, A. Cornet, et al. Nanostructured metal oxides synthesized by hard template method for gas sensing applications. *Sensors Actuators B Chem.* **2005,** 109, 57–63.

[240] H. Wang, W. Guo, Z. Jiang, R. Yang, et al. New insight into the enhanced activity of ordered mesoporous nickel oxide in formaldehyde catalytic oxidation reactions. *J. Catal.* **2018,** 361, 370–383.

[241] Q. Liu, J. Li, Z. Zhao, M. Gao, et al. Design, synthesis and catalytic performance of vanadium-incorporated mesoporous silica KIT-6 catalysts for the oxidative dehydrogenation of propane to propylene. *Catal. Sci. Technol.* **2016,** 6, 5927–5941.

[242] K. Selvakumar, S.M.S. Kumar, R. Thangamuthu, P. Rajput, et al. 2D and 3D silica-template-derived MnO_2 electrocatalysts towards enhanced oxygen evolution and oxygen reduction activity. *ChemElectroChem*. **2018,** 5, 3980–3990.

[243] B.T. Yonemoto, G.S. Hutchings, F. Jiao. A general synthetic approach for ordered mesoporous metal sulfides. *J. Am. Chem. Soc.* **2014,** 136, 8895–8898.

[244] P. Mei, Y. Yamauchi, M. Pramanik, A. Fatehmulla, et al. Hard-templated preparation of mesoporous cobalt phosphide as an oxygen evolution electrocatalyst. *Electrochem. Commun.* **2019,** 104, 106476.

[245] A. Saad, H. Shen, Z. Cheng, Q. Ju, et al. Three-dimensional mesoporous phosphide-spinel oxide heterojunctions with dual function as catalysts for overall water splitting. *ACS Appl. Energy Mater.* **2020,** 3, 1684–1693.

[246] Y. Wang, B. Zhang, W. Pan, H. Ma, et al. 3D porous nickel-cobalt nitrides supported on nickel foam as efficient electrocatalysts for overall water splitting. *ChemSusChem*. **2017,** 10, 4170–4177.

[247] Z. Xue, J. Kang, D. Guo, C. Zhu, et al. Electrochimica Acta self-supported cobalt nitride porous nanowire arrays as bifunctional electrocatalyst for overall water splitting. *Electrochim. Acta*. **2018,** 273, 229–238.

[248] B. Liu, L. Huo, R. Si, J. Liu, et al. A general method for constructing two-dimensional layered mesoporous mono- and binary-transition-metal nitride/graphene as an ultra-efficient support to enhance its catalytic activity and durability for electrocatalytic application. *ACS Appl. Mater. Interfaces*. **2016,** 8, 18770–18787.

[249] H. Yan, C. Tian, L. Sun, B. Wang, et al. Small-sized and high-dispersed WN from $[SiO_4(W_3O_9)_4]^{4-}$ clusters loading on GO-derived graphene as promising carriers for methanol electro-oxidation. *Energy Environ. Sci.* **2014,** 7, 1939–1949.

[250] D. Gao, J. Zhang, T. Wang, W. Xiao, et al. Metallic Ni_3N nanosheets with exposed active surface sites for efficient hydrogen evolution. *J. Mater. Chem. A.* **2016,** 4, 17363–17369.

[251] B. Cao, G.M. Veith, J.C. Neuefeind, R.R. Adzic, et al. Mixed close-packed cobalt molybdenum nitrides as non-noble metal electrocatalysts for the hydrogen evolution reaction. *J. Am. Chem. Soc.* **2013,** 135, 19186–19192.

[252] A. Lippitz, T. Hu. XPS investigations of chromium nitride thin films. *Surf. Coat. Technol.* **2005,** 200, 250–253.

[253] Y. Wang, C. Xie, D. Liu, X. Huang, et al. Nanoparticle-stacked porous nickel-iron nitride nanosheet: A highly efficient bifunctional electrocatalyst for overall water splitting. *ACS Appl. Mater. Interfaces*. **2016,** 8, 18652–18657.

[254] X. Chen, P. Gao, H. Liu, J. Xu, et al. In situ growth of iron-nickel nitrides on carbon nanotubes with enhanced stability and activity for oxygen evolution reaction. *Electrochim. Acta*. **2018,** 267, 8–14.

[255] Z. Liu, H. Tan, J. Xin, J. Duan, et al. Metallic intermediate phase inducing morphological transformation in thermal nitridation: Ni_3FeN-nased three-dimensional hierarchical electrocatalyst for water splitting. *ACS Appl. Mater.*

Interfaces. **2018,** 10, 3699–3706.

[256] C. Dong, X. Wang, X. Liu, X. Yuan, et al. In situ grown Nb_4N_5 nanocrystal on nitrogen-doped graphene as a novel anode for lithium ion battery. *RSC Adv*. **2016,** 6, 81290–81295.

[257] X. Li, Z. Ao, J. Liu, H. Sun, et al. Topotactic transformation of metal−organic frameworks to graphene-encapsulated transition-metal nitrides as efficient fenton-like catalysts. *ACS Nano*. **2016,** 10, 11532–11540.

[258] M. Chhowalla, H.E. Unalan. Thin films of hard cubic Zr_3N_4 stabilized by stress. *Nat. Mater*. **2005,** 4, 317–322.

[259] Y. Yuan, Y. Zhou, H. Shen, S.A. Rasaki, et al. Holey sheets of interconnected carbon-coated nickel nitride nanoparticles as highly active and durable oxygen evolution electrocatalysts. *Appl. Energy Mater*. **2018,** 1, 6774–6780.

[260] Y. Gu, S. Chen, J. Ren, Y.A. Jia, et al. Electronic structure tuning in Ni_3FeN/r-GO aerogel toward bifunctional electrocatalyst for overall water splitting. *ACS Nano*. **2018,** 12, 245–253.

[261] Y. Yuan, L. Yang, B. He, E. Pervaiz, et al. Cobalt-zinc nitride on nitrogen doped carbon black nanohybrids as a non-noble metal electrocatalyst for oxygen reduction reaction. *Nanoscale*. **2017,** 9, 6259–6263.

[262] A.M. Alexander, J.S.J. Hargreaves. Alternative catalytic materials: carbides, nitrides, phosphides and amorphous boron alloys. *Chem. Soc. Rev*. **2010,** 39, 4388–4401.

[263] X. Yu, Z. Zhao, D. Sun, N. Ren, et al. TiO_2/TiN core/shell nanobelts for efficient solar hydrogen generation. *Chem. Commun.* **2018,** 54, 6056–6059.

[264] Y. Hou, T. Huang, Z. Wen, S. Mao, et al. Metal-organic framework-derived nitrogen-doped core-shell-structured porous Fe/Fe_3C@C nanoboxes supported on graphene sheets for efficient oxygen. *Adv. Energy Mater*. **2014,** 4, 1400337.

[265] J. Wang, C.F. Tan, T. Zhu, G.W. Ho. Topotactic consolidation of monocrystalline CoZn hydroxides for advanced oxygen evolution electrodes. *Angew. Chem. Int. Ed.* **2016,** 128, 10482–10486.

[266] C.W. Abney, K.M.L. Taylor-Pashow, S.R. Russell, Y. Chen, et al. Topotactic transformations of metal-organic frameworks to highly porous and stable inorganic sorbents for efficient radionuclide sequestration. *Chem. Mater.* **2014,** 26, 5231–5243.

[267] S.J. Yang, S. Nam, T. Kim, J.H. Im, et al. Preparation and exceptional lithium anodic performance of porous carbon-coated ZnO quantum dots derived from a metal-organic framework. *J. Am. Chem. Soc.* **2013,** 135, 7394–7397.

[268] L. Zhang, H.B. Wu, X.W. (David) Lou. Metal-organic-frameworks-derived general formation of hollow structures with high complexity. *J. Am. Chem. Soc.* **2013,** 135, 10664–10672.

[269] L. Zhang, H.B. Wu, S. Madhavi, H.H. Hng, et al. Formation of Fe_2O_3 microboxes with hierarchical shell structures from metal-organic frameworks and their lithium storage properties. *J. Am. Chem. Soc.* **2012,** 134, 17388–17391.

[270] M. Xia, X. Zhang, T. Liu, H. Yu, et al. Commercially available Prussian blue get energetic in aqueous K-ion batteries. *Chem. Eng. J.* **2020,** 394, 124923.

[271] X.W. He, L.D. Tian, M.T. Qiao, J.Z. Zhang, et al. A novel highly crystalline $Fe_4(Fe(CN)_6)_3$ concave cube anode material for Li-ion batteries with high capacity and long life. *J. Mater. Chem. A.* **2019,** 7, 11478–11486.

[272] T. Yamashita, P. Hayes. Analysis of XPS spectra of Fe^{2+} and Fe^{3+} ions in oxide materials. *Appl. Surf. Sci.* **2008,** 254, 2441–2449.

[273] J.A.R. Guivar, E.A. Sanches, F. Bruns, E. Sadrollahi, et al. Vacancy ordered γ-Fe_2O_3 nanoparticles functionalized with nanohydroxyapatite: XRD, FTIR, TEM, XPS and Mössbauer studies. *Appl. Surf. Sci.* **2016,** 389, 721–734.

[274] J.F. Moulder, W.F. Stickle, P.E. Sobol, K.D. Bomben. Handbook of X-ray photoelectron spectroscopy, physical electronics.

[275] P. Mills, J.L. Sullivan. A study of the core level electrons in iron and its three oxides by means of X-ray photoelectron spectroscopy. *J. Phys. D. Appl. Phys.* **1983,** 16, 723–732.

[276] D. Liang, H. Zhang, X. Ma, S. Liu, et al. MOFs-derived core-shell Co_3Fe_7@Fe_2N

nanopaticles supported on rGO as high-performance bifunctional electrocatalyst for oxygen reduction and oxygen evolution reactions. *Mater. Energy*. **2020,** 17, 100433.

[277] S. Sultan, J.N. Tiwari, J.H. Jang, A.M. Harzandi, et al. Highly efficient oxygen reduction reaction activity of graphitic tube encapsulating nitrided CoxFey alloy. *Adv. Energy Mater.* **2018,** 8, 1801002.

[278] Z. Chen, Y. Li, L. Lei, S. Bao, et al. Investigation of Fe_2N@carbon encapsulated in N-doped graphene-like carbon as a catalyst in sustainable zinc-air batteries. *Catal. Sci. Technol.* **2017,** 7, 5670–5676.

[279] Y. Lou, J. Liu, M. Liu, F. Wang. Hexagonal Fe_2N coupled with N-doped carbon: Crystal-plane-dependent electrocatalytic activity for oxygen reduction. *ACS Catal.* **2020,** 10, 2443–2451.

[280] D. Liu, Z. Jin, Y. Bi. Charge transmission channel construction between a MOF and rGO by means of Co-Mo-S modification. *Catal. Sci. Technol.* **2017,** 7, 4478–4488.

[281] J. Moser, M. Grätzel. Photosensitized electron injection in colloidal semiconductors. *J. Am. Chem. Soc.* **1984,** 106, 6557–6564.

[282] X. Hao, Z. Jin, G. Lu. Enhanced surface electron transfer with the aid of methyl viologen on the Co_3O_4-g-C_3N_4 photocatalyst. *Chem. Lett.* **2016,** 45, 116–118.

[283] X. Meng, Y. Dong, Q. Hu, Y. Ding. Co nanoparticles decorated with nitrogen doped carbon nanotubes for boosting photocatalytic water splitting. *ACS Sustain. Chem. Eng.* **2019,** 7, 1753–1759.

[284] S.H. Li, N. Zhang, X. Xie, R. Luque, et al. Stress-transfer-induced in situ formation of ultrathin nickel phosphide nanosheets for efficient hydrogen evolution. *Angew. Chem. Int. Ed.* **2018,** 57, 13082–13085.

[285] M. Zheng, Y. Ding, L. Yu, X. Du, et al. In situ grown pristine cobalt sulfide as bifunctional photocatalyst for hydrogen and oxygen evolution. *Adv. Funct. Mater.* **2017,** 27, 1605846.

[286] H. Wang, Z. Jin. Rational design W-doped Co-ZIF-9 based Co_3S_4 composite

photocatalyst for efficient visible-light-driven photocatalytic H_2 evolution. *Sustain. Energy Fuels*. **2019,** 3, 173–183.

[287] M.Q. Yang, J. Dan, S.J. Pennycook, X. Lu, et al. Ultrathin nickel boron oxide nanosheets assembled vertically on graphene: a new hybrid 2D material for enhanced photo/electro-catalysis. *Mater. Horizons*. **2017,** 4, 885–894.

[288] W. Zhen, J. Ma, G. Lu. Small-sized Ni(1 1 1) particles in metal-organic frameworks with low over-potential for visible photocatalytic hydrogen generation. *Appl. Catal. B Environ.* **2016,** 190, 12–25.

[289] Z. Yan, X. Yu, Y. Zhang, H. Jia, et al. Enhanced visible light-driven hydrogen production from water by a noble-metal-free system containing organic dye-sensitized titanium dioxide loaded with nickel hydroxide as the cocatalyst. *Appl. Catal. B Environ.* **2014,** 160–161, 173–178.

[290] Y. Wang, J. Hong, W. Zhang, R. Xu. Carbon nitride nanosheets for photocatalytic hydrogen evolution: remarkably enhanced activity by dye sensitization. *Catal. Sci. Technol.* **2013,** 3, 1703–1711.

[291] L. Yang, J. Huang, L. Shi, L. Cao, et al. Efficient hydrogen evolution over Sb doped SnO_2 photocatalyst sensitized by Eosin Y under visible light irradiation. *Nano Energy*. **2017,** 36, 331–340.

[292] B. Weng, Q. Quan, Y. Xu. Decorating geometry- and size-controlled sub-20nm Pd nanocubes onto 2D TiO_2 nanosheets for simultaneous H_2 evolution and 1,1-diethoxyethane production. *J. Mater. Chem. A*. **2016,** 4, 18366–18377.

[293] C. Han, Z. Chen, N. Zhang, J.C. Colmenares, et al. Hierarchically CdS decorated 1D ZnO nanorods-2D graphene hybrids: Low temperature synthesis and enhanced photocatalytic performance. *Adv. Funct. Mater.* **2015,** 25, 221–229.

[294] M.Q. Yang, Y.J. Xu, B. Weng, Y.J. Xu. Synthesis of In_2S_3-CNT nanocomposites for selective reduction under visible light. *J. Mater. Chem. A*. **2014,** 2, 1710–1720.

[295] X. Pan, Y. Zhao, S. Liu, C.L. Korzeniewski, et al. Comparing graphene-TiO_2 nanowire and graphene-TiO_2 nanoparticle composite photocatalysts. *ACS Appl.*

Mater. Interfaces. **2012,** 4, 3944–3950.

[296] N. Zhang, Y. Xu. Aggregation- and leaching-resistant, reusable, and multifunctional Pd@CeO_2 as a robust nanocatalyst achieved by a hollow core-shell strategy. *Chem. Mater.* **2013,** 25, 1979–1988.

[297] M. Yang, C. Han, Y. Xu. Insight into the Effect of Highly dispersed MoS_2 versus layer-structured MoS_2 on the photocorrosion and photoactivity of CdS in graphene-CdS-MoS_2 composites. *J. Phys. Chem. C*. **2015,** 119, 27234–27246.

[298] Z. Chen, J. Wang, C. Li. Mechanical deformation modes and anisotropy of IVB transition metal nitrides. *J. Alloys Compd.* **2013,** 575, 137–144.

[299] H. Yang, S. Luo, X. Li, S. Li, et al. Controllable orientation-dependent crystal growth of high-index faceted dendritic $NiC_{0.2}$ nanosheets as high-performance bifunctional electrocatalysts for overall. *J. Mater. Chem. A*. **2016,** 4, 18499–18508.

[300] A. Rajeswari, S. Vismaiya, A. Pius. Preparation, characterization of nano ZnO-blended cellulose acetate-polyurethane membrane for photocatalytic degradation of dyes from water. *Chem. Eng. J.* **2017,** 313, 928–937.

[301] J. Nai, J. Zhang, X.W. (David) Lou. Construction of single-crystalline Prussian blue analog hollow nanostructures with tailorable topologies. *Chem*. **2018,** 4, 1967–1982.

[302] N. Yao, P. Li, Z. Zhou, Y. Zhao, et al. Synergistically tuning water and hydrogen binding abilities over Co_4N by Cr doping for exceptional alkaline hydrogen evolution electrocatalysis. *Adv. Energy Mater.* **2019,** 9, 1902449.

[303] A. Richel, N.P. Johnson. Observation of Bragg reflection in photonic crystals synthesized from air spheres in a titania matrix. *Appl. Phys. Lett.* **2000,** 76, 1816–1818.

[304] J. Nai, X.W. (David) Lou. Hollow structures based on Prussian blue and its analogs for electrochemical energy storage and conversion. *Adv. Mater.* **2019,** 31, 1706825.

[305] H. Jiang, L. Huang, Y. Wei, B. Wang, et al. Bio-derived hierarchical multicore-

shell Fe_2N-nanoparticle-impregnated N-doped carbon nanofiber bundles: A host material for lithium-/potassium-ion storage. *Nano-Micro Lett.* **2019,** 11, 56.

[306] N. Zhang, S. Xie, W. Wang, D. Xie, et al. Ultra-small Fe_2N/N-CNTs as efficient bifunctional catalysts for rechargeable Zn-Air batteries. *J. Electrochem. Soc.* **2020,** 167, 020505.

[307] C.-K. Cheng, C.-H. Lin, H.-C. Wu, C.-C.M. Ma, et al. The two-dimensional nanocomposite of molybdenum disulfide and nitrogen-doped graphene oxide for efficient counter electrode of dye-densitized dolar cells. *Nanoscale Res. Lett.* **2016,** 11, 117.

[308] H. Wang, X. Qiu, W. Wang, L. Jiang, et al. Iron sulfide nanoparticles embedded into a nitrogen and sulfur Co-doped carbon sphere as a highly active oxygen reduction electrocatalyst. *Front. Chem.* **2019,** 7, 855.

[309] H. Yan, M. Meng, L. Wang, A. Wu, et al. Small-sized tungsten nitride anchoring into a 3D CNT-rGO framework as a superior bifunctional catalyst for the methanol oxidation and oxygen reduction reactions. *Nano Res.* **2016,** 9, 329–343.

[310] J. Yuan, X. Huang, L. Zhang, F. Gao, et al. Tuning piezoelectric field for optimizing the coupling effect of piezo-photocatalysis. *Appl. Catal. B Environ.* **2020,** 278, 119291.

[311] F. Meng, J. Li, S.K. Cushing, M. Zhi, et al. Solar hydrogen generation by nanoscale p-n junction of p-type molybdenum disulfide/n-type nitrogen-doped reduced graphene oxide. *J. Am. Chem. Soc.* **2013,** 135, 10286–10289.

[312] X. Zhang, Y. Zhao, X. Jia, Y. Zhao, et al. Silica-protected ultrathin Ni_3FeN nanocatalyst for the efficient hydrolytic dehydrogenation of NH_3BH_3. *Adv. Energy Mater.* **2018,** 8, 1702780.

[313] E. Lin, Z. Kang, J. Wu, R. Huang, et al. $BaTiO_3$ nanocubes/cuboids with selectively deposited Ag nanoparticles: Efficient piezocatalytic degradation and mechanism. *Appl. Catal. B Environ.* **2021,** 285, 119823.

[314] J.M. Wu, Y.-G. Sun, W.-E. Chang, J.-T. Lee. Piezoelectricity induced water splitting and formation of hydroxyl radical from active edge sites of MoS_2

nanoflowers. *Nano Energy*. **2018,** 46, 372–382.

Biography

1. Z. Cheng, W. Qi, C. H. Pang, T. Thomas, T. Wu, S. Liu*, M. Yang*, Recent advances in transition metal nitride-based materials for photocatalytic applications. *Advanced Functional Materials*, **2021**, 2100553.

2. Z. Cheng, A. Saad, H. Guo, C. Wang, S. Liu, T. Thomas, M. Yang. Ordered mesoporous transition metal nitrides prepared through hard template nanocasting and rapid nitridation process. *Journal of Alloys and Compounds* **2020**, 838, 155375.

3. Z. Cheng, A. Saad, S. Adimi, H. Guo, S. Liu, T. Thomas, M. Yang. Metal organic framework-derived porous Fe_2N nanocubes by rapid-nitridation for efficient photocatalytic hydrogen evolution. *Materials Advances* **2020**, 1, 1161–1167.

4. A. Saad, Z. Cheng, H. Shen, T. Thomas, M. Yang. Recent advances in nanocasting cobalt-based mesoporous materials for energy storage and conversion. *Electrocatalysis* **2021**, 11, 465–484.

5. A. Saad, Z. Cheng, X. Zhang, S. Liu, H. Shen, T. Thomas, J. Wang, M. Yang. Ordered mesoporous cobalt-nickel nitride prepared by nanocasting for oxygen evolution reaction electrocatalysis. *Advanced Materials Interfaces* **2019**, 6, 1900960.

6. A. Saad, Z. Cheng, H. Shen, H. Guo, P. Attfield, T. Thomas, M. Yang. Surface engineering of mesoporous triphasic cobalt-copper phosphides as active electrocatalysts for overall water splitting. *Sustainable Energy & Fuels* **2021**, 5, 1366-1373.

7. A. Saad, H. Shen, Z. Cheng, R. Arbi, B. Guo, L. S. Hui, K. Liang, S. Liu, J. P. Attfield, A. Turak. Mesoporous ternary nitrides of earth-abundant metals as oxygen evolution electrocatalyst. *Nano-Micro Letters* **2020**, 12, 1–13.

8. A. Saad, H. Shen, Z. Cheng, Q. Ju, H. Guo, M. Munir, A. Turak, J. Wang, M. Yang. Three-dimensional mesoporous phosphide-spinel oxide heterojunctions with dual function as catalysts for overall water splitting. *ACS Applied Energy Materials* **2020**, 3, 1684–93.

9. X. Meng, W. Kuang, W. Qi, Z. Cheng, T. Thomas, S. Liu, C. Yang, M. Yang. Ultra-

low loading of Au clusters on nickel nitride efficiently boosts photocatalytic hydrogen production with titanium dioxide. *Chemcatchem* **2020**, 12, 2752–59.

10. W. Qi, S. Liu, F. Li, H. Jiang, Z. Cheng, S. Zhao, M. Yang. Prussian blue derived Fe_2N for efficiently improving the photocatalytic hydrogen evolution activity of g-C_3N_4 nanosheets. *Catalysis Science Technology* **2019**, 9, 2571–77.